

**Design of Surface Micro-machined Inertial MEMS
Sensor with Meta-heuristic Topology Optimization**

by

Hossein Rostami Najafabadi

A thesis submitted in partial
fulfillment of the requirements for the degree of

**PhD *en cotutelle* in
Mechanical Engineering (Ontario Tech University)
Mechatronics (University of São Paulo)**

Department of Automotive, Mechanical, and Manufacturing Engineering
Faculty of Engineering and Applied Science
University of Ontario Institute of Technology (Ontario Tech University)
Oshawa, Ontario, Canada

Department of Mechatronics and Mechanical Systems Engineering
Escola Politécnica da Universidade de São Paulo
University of São Paulo, São Paulo, Brazil

March 2023

© Hossein Rostami Najafabadi, 2023

THESIS EXAMINATION INFORMATION

Submitted by: **Hossein Rostami Najafabadi**

**PhD *en cotutelle* in Mechanical Engineering (Ontario Tech University) and
Mechatronics (University of São Paulo)**

Thesis title: Design of Surface Micro-machined Inertial MEMS Sensor with Meta-heuristic Topology Optimization

An oral defense of this thesis took place on January 27, 2023 in front of the following examining committee:

Examining Committee:

Chair of Examining Committee	Dr. Ghaus Rizvi, Ontario Tech University
Research Supervisor	Dr. Thiago de Castro Martins, University of São Paulo
Research Supervisor	Dr. Ahmad Barari, Ontario Tech University
Examining Committee Member	Dr. Meaghan Charest-Finn, Ontario Tech University
Examining Committee Member	Dr. Marcos de Sales Guerra Tsuzuki, University of São Paulo
University Examiner	Dr. Anatoli Chkrebtti, Professor of physics at Faculty of Science, Ontario Tech University
External Examiner	Dr. Mario Ricardo Gongora-Rubio, Senior researcher at Instituto de Pesquisas Tecnológicas de São Paulo (IPT)

The above committee determined that the thesis is acceptable in form and content and that a satisfactory knowledge of the field covered by the thesis was demonstrated by the candidate during an oral examination. A signed copy of the Certificate of Approval is available from the School of Graduate and Postdoctoral Studies.

Abstract

Micro-Electro-Mechanical Systems (MEMS) are getting popular for a variety of applications due to their small size, low cost, and good performance. MEMS devices are designed by combining simple shapes based on the experience of previous cases. Using mathematical design methods such as Topology Optimization (TO) helps to find the best possible design for a specific application. In a landslide monitoring application, high sensitive MEMS accelerometers are required to accurately predict the occurrence of landslides. But available TO methods are unable to find a design with maximum sensitivity, variable loading condition, and subjected to several constrains. Constraints are because of manufacturing limits in MEMS fabrication and performance limits from the physical problem. The aim of this thesis is to develop a meta-heuristic TO method using Simulated Annealing (SA) to solve non-convex and multi constraint TO problems without gradient information. This TO utilizes crystallization factors to improve the convergence and reduces computational costs in TO. The proposed method is validated with benchmark problems in the literature and it is successfully used for the TO MEMS accelerometers. Analysis of optimization parameters in this design gives some useful information about the convergence and uniqueness of the optimum solution. The optimized designs are then compared to available designs for several performance parameters. Additionally, some filtering and post-processing methods are developed to apply manufacturing limits in the lithography process.

Keywords: Topology Optimization, Simulated Annealing, Crystallization Factor, Post-processing, Manufacturing constraints, MEMS Accelerometer.

Resumo

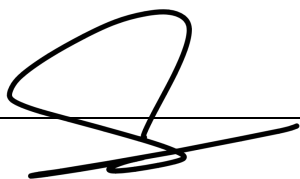
Os sistemas microeletromecânicos (MEMS) estão se tornando populares para uma variedade de aplicações devido ao seu pequeno tamanho, baixo custo e bom desempenho. Os dispositivos MEMS são projetados combinando formas simples com base na experiência de casos anteriores. O uso de métodos de projeto matemático, como a Otimização de Topologia (TO), ajuda a encontrar o melhor projeto possível para um aplicativo específico. Em uma aplicação de monitoramento de deslizamentos de terra, acelerômetros MEMS de alta sensibilidade são necessários para prever com precisão a ocorrência de deslizamentos de terra. Mas os métodos TO disponíveis são incapazes de encontrar um projeto com sensibilidade máxima, condição de carregamento variável e sujeito a várias restrições. As restrições são devidas aos limites de fabricação na fabricação de MEMS e aos limites de desempenho do problema físico. O objetivo desta tese é desenvolver um método TO meta-heurístico usando Simulated Annealing (SA) para resolver problemas TO não convexos e multi-restrições sem informação de gradiente. Este TO utiliza fatores de cristalização para melhorar a convergência e reduzir os custos computacionais no TO. O método proposto é validado com problemas de referência na literatura e é usado com sucesso para os acelerômetros TO MEMS. A análise dos parâmetros de otimização neste projeto fornece algumas informações úteis sobre convergência e exclusividade da solução ótima. Os designs otimizados são então comparados aos designs disponíveis para vários parâmetros de desempenho. Além disso, alguns métodos de filtragem e pós-processamento são desenvolvidos para aplicar os limites de fabricação no processo de litografia.

Palavras-chave: Otimização Topológico, Recozimento Simulado, Fator de Cristalização, Pós-processamento, Acelerômetro MEMS.

AUTHOR'S DECLARATION

I hereby declare that this thesis consists of original work of which I have authored. This is a true copy of the thesis, including any required final revisions, as accepted by my examiners.

I authorize the University of Ontario Institute of Technology (Ontario Tech University) and the University of São Paulo to lend this thesis to other institutions or individuals for the purpose of scholarly research. I further authorize University of Ontario Institute of Technology (Ontario Tech University) and the University of São Paulo to reproduce this thesis by photocopying or by other means, in total or in part, at the request of other institutions or individuals for the purpose of scholarly research. I understand that my thesis will be made electronically available to the public.

A handwritten signature in black ink, consisting of a large loop and a trailing line, positioned above a horizontal line.

Hossein Rostami Najafabadi

STATEMENT OF CONTRIBUTIONS

I hereby certify that I am the sole author of this thesis. I have used standard referencing practices to acknowledge ideas, research techniques, or other materials that belong to others. The following is the list of publications in scientific events:

Hossein R. Najafabadi, Tiago G. Goto, Mizael S. Falheiro, Thiago C. Martins, Ahmad Barari, Marcos S. G. Tsuzuki; ‘‘Smart Topology Optimization Using Adaptive Neighborhood Simulated Annealing’’. *Journal of Applied Science*

Tiago G. Goto, Hossein R. Najafabadi, Mizael F. Falheiro, Rafael T. Moura, Larissa Driemeier, Ahmad Barari, Marcos S. G. Tsuzuki, Thiago C. Martins; ‘‘A new non-gradient-based topology optimization algorithm with black–white density and manufacturability constraints’’. *Journal of Structures*

Tiago G. Goto, Hossein R. Najafabadi, Guilherme C. Duran, Edson K. Ueda, André K. Sato, Thiago C. Martins, Rogério Y. Takimoto, Hossein Gohari, Ahmad Barari, Marcos S. G. Tsuzuki; ‘‘Versatility of Simulated Annealing with Crystallization Heuristic: Its Application to a Great Assortment of Problems’’. *Engineering Problems - Uncertainties, Constraints and Optimization Techniques, IntechOpen*

Hossein R. Najafabadi, Tiago G. Goto, Thiago C. Martins, Ahmad Barari, Marcos de Sales Guerra Tsuzuki; ‘‘Topology Optimization of Capacitive MEMS Accelerometers for Seismic Applications’’. *20th International Conference on Geometry and Graphics*

Hossein R. Najafabadi, Bruno M. Verona, Tiago G. Goto, Thiago C. Martins, Ahmad Barari, Marcos S. G. Tsuzuki; ‘‘Topology Optimization and Microfabrication Constraints’’. *14th IEEE International Conference on Industry Applications (INDUSCON)*

Tiago Goto, Hossein R. Najafabadi, Mizael Falheiro, Thiago C. Martins, Ahmad Barari, Marcos S.G. Tsuzuki; ‘‘Topological Optimization and Simulated Annealing’’. *17th IFAC Symposium on Information Control Problems in Manufacturing INCOM 2021*

Hossein R. Najafabadi, Tiago Goto, Mizael Falheiro, Thiago C. Martins, Ahmad Barari, Marcos S.G. Tsuzuki; ‘‘Post-Processing of non gradient-based Topology Optimization with Simulated Annealing’’. *17th IFAC Symposium on Information Control Problems in Manufacturing INCOM 2021*

Hossein R. Najafabadi, Tiago G. Goto, Thiago C. Martins, Ahmad Barari, Marcos S.G. Tsuzuki; ‘‘Multi-objective Topology Optimization Using Simulated Annealing Method’’. *19th International Conference on Geometry and Graphics*

To my family, friends, and whoever brings peace to the world.

Acknowledgements

I would like to thank everyone who helped me accomplish this work. First of all, I would like to thank Professor Thiago de Castro Martins and Professor Ahmad Barari for their supervision during this project and providing research material in Computational Geometry Laboratory and AD2MLabs. I am thankful to Research Support Foundation of the State of São Paulo for the financial support of this project by process number of 2019/03453-2 Fundação de Amparo à Pesquisa do Estado de São Paulo(FAPESP) and to IPT (Instituto de Pesquisas Tecnológicas) for giving us access to their equipment at LMI (Laboratório de Micromanufatura). We would like to acknowledge CMC Micro-systems for the provision of products and services that facilitated this research, including CAD tools and design methodology, fabrication services, and engineering services.

It is a pleasure to thank my friends in Iran, Brazil, Canada, and all around the world for the wonderful time we shared.

Finally, I would like to express my deep and sincere gratitude to my family for their continuous and unparalleled love, help, and support. I am grateful to my sister for her support and also to her children who are always in my heart. I will be forever indebted to my parents for giving me the opportunities and experiences that have made me who I am. They selflessly encouraged me to explore new directions in life and seek my own destiny. This journey would not have been possible if not for them, and I dedicate this milestone to them.

Contents

Abstract	iii
Resumo	iv
Author's Declaration	v
Statement of Contributions	vi
Acknowledgements	viii
Contents	ix
List of Tables	xi
List of Figures	xii
List of Abbreviations and Acronyms	xvi
1 INTRODUCTION	1
1.1 Landslide	2
1.1.1 Falls	2
1.1.2 Slide	3
1.1.3 Spreads	3
1.1.4 Flows	3
1.2 Landslide monitoring systems	5
1.3 Structural health monitoring with accelerometers	7
1.4 Required specifications of an accelerometer for landslide monitoring and structural health monitoring	9
2 THEORY AND BACKGROUND	13
2.1 Accelerometer and possible configurations	13
2.1.1 Suspension systems and optimized designs in the literature	19
2.2 Topology Optimization	23
2.2.1 Optimization Algorithms	23
2.2.2 Constrained optimization	27
2.2.3 Simulated Annealing (SA) optimization algorithm	30
2.2.4 Gradient and non-gradient based Topology Optimization	34
2.3 Variable loading TO	38

2.4	Manufacturability in topology optimization	39
2.5	Microfabrication	40
2.5.1	Bulk Micromachining	41
2.5.2	Surface Micromachining	41
2.6	Limitation in surface micromachining	43
2.7	Morphological operators	45
2.7.1	Dilation	46
2.7.2	Erosion	47
2.7.3	Opening	47
2.7.4	Closing	48
3	METHODOLOGY AND RESULTS	49
3.1	Topology Optimization with SA and crystallization factors . . .	49
3.2	Post-Processing	66
3.3	Binary Topology Optimization	74
3.4	Concept design of the accelerometer	78
3.5	Objective and constraints of Topology Optimization	80
3.6	Verification of Performance	97
3.7	Design for Microfabrication	106
4	CONCLUSION AND FUTURE WORKS	109
	BIBLIOGRAPHY	111

List of Tables

Table 1 – The required specifications of inertial accelerometer sensor for landslide and structural health monitoring.	11
Table 2 – Parameters of SA for the design of the cantilever beam.	54
Table 3 – Compliance (C) of optimized cantilever beam from the GTO in the literature and the proposed method herein.	58
Table 4 – Compliance (C) of optimized half-MBB beam from the GTO in the literature and the proposed method herein.	61
Table 5 – Heat transfer compliance (C) for a 3D plate with a heat sink on middle top from GTO in literature and proposed method.	64
Table 6 – Compliance (C) of optimized cantilever beam from the GTO in the literature and NGTO with SA after post-processing (PP).	70
Table 7 – Compliance of optimized half-MBB beam from the GTO in the literature and NGTO with SA after post-processing (PP) in different volume fractions.	72
Table 8 – Dimensions of the design domain and parameters of SA for TO of out-of-plane MEMS accelerometer.	79
Table 9 – Design specifications of the optimized structures.	97
Table 10 – Mechanical properties of Silicon as the structural material.	97
Table 11 – Comparison of specifications and performance in proposed designs and similar designs in the literature.	105

List of Figures

Figure 2.1 – Parallel plate configuration of the capacitive accelerometer.	15
Figure 2.2 – Transverse comb configuration of the capacitive accelerometer.	17
Figure 2.3 – Lateral comb configuration of the capacitive accelerometer	18
Figure 2.4 – Schematic of beam configurations used as suspension structure	19
Figure 2.5 – Flow chart of unconstrained optimization with SA algorithm	33
Figure 2.6 – Effect of a small dust particle on the patterns made with photolithogra- phy.	44
Figure 2.7 – Over etching and change of dimensions by keeping the sample in etchant for a longer time.	44
Figure 2.8 – Change of corners and edges in etching and measured radius.	45
Figure 3.9 – Schematic of the cantilever beam with point load (F) at the free end. .	53
Figure 3.10–Minimized compliance from the proposed method versus the number of iterations for the cantilever beam problem.	55
Figure 3.11–Number of accepted and rejected solutions versus temperature in TO with SA for the cantilever beam problem.	56
Figure 3.12–Crystallization factor versus temperature for four locations of the can- tilever beam in proposed TO method with SA.	57
Figure 3.13–Optimized topology of the cantilever beam for minimizing compliance with GTO from the literature (left) and the proposed method (right) for different volume fractions.	59
Figure 3.14–Schematic of the MBB beam with a point load (F) at the middle. . . .	60
Figure 3.15–Schematic of the half-MBB beam with a point load (F) and new bound- ary conditions.	60
Figure 3.16–Compliance from TO by the proposed method versus different numbers of iterations in the half-MBB problem.	61
Figure 3.17–Optimized topology of the half-MBB beam from the GTO in the litera- ture (left) and from the proposed method (right) with different volume fractions.	62
Figure 3.18–Schematic of the heat conduction problem with a heat sink on the middle top.	63
Figure 3.19–Heat compliance from TO by the proposed method versus the number of iterations for heat transfer problem.	64
Figure 3.20–Optimized topology of the heat transfer problem from [113] (left) and the proposed method (right) with different volume fractions.	65
Figure 3.21–Optimized topology of a 3D cantilever beam with 1000 iterations in each temperature and the proposed TO with SA and 0.5 volume fraction.	66

Figure 3.22—surface micromachining process with a mask from TO without post-processing.	67
Figure 3.23—Post-processed results of GTO and TO with SA in a cantilever beam problem with different volume fractions.	69
Figure 3.24—Optimized topology of the half-MBB beam with GTO of reference and NGTO with SA after post-processing in different volume fractions. . .	71
Figure 3.25—Effect of post-processing by density filters on products of surface micromachining.	72
Figure 3.26—Simulated etching for the optimized topologies of the cantilever beam with only density filters post-processing (left) and by adding morphological operators (right).	73
Figure 3.27—A targeting element and neighbors in a 2D discretized domain.	75
Figure 3.28—Effect of adding connectivity criteria to the binary TO with SA.	75
Figure 3.29—Convergence of compliance and connectivity versus temperature in binary TO of cantilever beam with SA.	76
Figure 3.30—Number of accepted and rejected solutions versus temperature for the objective of compliance and connectivity in binary TO with SA.	76
Figure 3.31—Neighboring elements defined for the generation of connected solutions.	77
Figure 3.32—Results of binary TO with SA by checking connection in new solutions.	78
Figure 3.33—The boundary condition, design domain, and initial proof mass.	79
Figure 3.34—flow chart of the topology optimization in the sensor problem.	80
Figure 3.35—Optimized topology of the sensor for minimizing the first natural frequency and constraints on the ratio of frequencies, connectivity, and maximum displacement in a trial run.	82
Figure 3.36—Number of accepted and rejected solutions in minimizing first natural frequency and constraints on the ratio of frequencies, connectivity, and maximum displacement in a trial run.	82
Figure 3.37—Convergence of objective function versus temperature in minimizing first natural frequency and constraints on the ratio of frequencies, connectivity, and maximum displacement in a trial run.	83
Figure 3.38—Change of sensitivity in minimizing first natural frequency and constraints on the ratio of frequencies, connectivity, and maximum displacement in a trial run.	84
Figure 3.39—Results of TO for maximizing sensitivity and constraints on the ratio of frequencies, connectivity, and maximum displacement in a trial run.	84
Figure 3.40—Accepted and rejected solutions for maximizing sensitivity and constraints on the ratio of frequencies, connectivity, and maximum displacement in a trial run.	85

Figure 3.41–Sensitivity versus temperature for maximizing sensitivity and constraints on the ratio of frequencies, connectivity, and maximum displacement in a trial run.	86
Figure 3.42–First natural frequency for maximizing sensitivity and constraints on the ratio of frequencies, connectivity, and maximum displacement in a trial run.	87
Figure 3.43–Results of TO for maximizing sensitivity and constraints on the ratio of frequencies, connectivity, and maximum displacement in the second trial run.	87
Figure 3.44–Number of accepted and rejected solutions versus temperature for maximizing sensitivity and constraints on the ratio of frequencies, connectivity, and maximum displacement in the second trial run.	88
Figure 3.45–Sensitivity versus temperature for maximizing sensitivity and constraints on the ratio of frequencies, connectivity, and maximum displacement in the second trial run.	88
Figure 3.46–First natural frequency for maximizing sensitivity and constraints on the ratio of frequencies, connectivity, and maximum displacement in the second trial run.	89
Figure 3.47–Results of maximizing sensitivity with the constraint on connectivity and maximum out-of-plane displacement.	89
Figure 3.48–Results of minimizing ratio of first natural frequency to the average of six first natural frequencies and constraint on a minimum of first natural frequency.	90
Figure 3.49–Optimized topology for maximizing sensitivity and constraint on connectivity, maximum displacement, and the ratio of second to first natural frequencies (D1).	91
Figure 3.50–Post-processed design for maximizing sensitivity and constraints on the maximum out-of-plane displacement, connectivity, and ratio of natural frequencies (D1).	91
Figure 3.51–Number of accepted and rejected solutions in each temperature for TO with SA in design (D1).	92
Figure 3.52–Convergence of sensitivity in TO with SA in design (D1).	92
Figure 3.53–Results of TO for minimizing the first natural frequency and constraints on connectivity, maximum displacement, and the ratio of second to first natural frequencies.	93
Figure 3.54–Post-processed results of TO with SA for minimized first natural frequency and constraints on connectivity, maximum out-of-plane displacement, and the ratio of natural frequencies (D2).	93
Figure 3.55–Number of accepted and rejected solutions for design (D2).	94

Figure 3.56–Convergence of minimizing the first natural frequency in Design (D2). . .	94
Figure 3.57–Optimized topology for maximizing the ratio of the second to the first natural frequency with constraints on maximum displacement and connectivity (D3)	95
Figure 3.58–Post-processed topology of design (D3).	95
Figure 3.59–Number of accepted and rejected solutions in each temperature for D3.	96
Figure 3.60–Convergence of the objective function (ratio of second to first natural frequency) to the optimum solution for design (D3).	96
Figure 3.61–Mesh for FEA of design (D1).	98
Figure 3.62–Total displacement in design (D1) from FE simulation with a scale of 1000.	98
Figure 3.63–Von Mises stress in design (D1) by applying $1g$ of inertial acceleration.	99
Figure 3.64–Mode shapes and natural frequencies from FEA in design (D1).	100
Figure 3.65–Mesh for FEA of design (D2).	101
Figure 3.66–Total displacement in design (D2) from FE simulation with a scale of 1000.	101
Figure 3.67–Von Mises stress in design (D2) by applying $1g$ of inertial acceleration.	102
Figure 3.68–Mode shapes and natural frequencies from FEA in design (D2).	102
Figure 3.69–Mesh for FEA of design (D3).	103
Figure 3.70–Total displacement in design (D3) from FE simulation with a scale of 1000.	103
Figure 3.71–Von Mises stress in design (D3) by applying $1g$ of inertial acceleration.	104
Figure 3.72–Mode shapes and natural frequencies from FEA in design (D3).	104
Figure 3.73–Simulated fabrication process with PolyMUMPs.	108

List of abbreviations and acronyms

AC	Alternative Current
CC	Connectivity Constraint
CMC	Canadian Microelectronics Corporation
CMOS	Complementary Metal–Oxide–Semiconductor
CVD	Chemical Vapor Deposition
DC	Direct current
DRIE	Deep Reactive Ion Etching
EMI	Electro-Magnetic Interference
FEA	Finite Element Analysis
GA	Genetic Algorithm
GTO	Gradient-based Topology Optimization
KKT	Karush–Kuhn–Tucker
LPCVD	Low-Pressure Chemical Vapor Deposition
MBB	Messerschmitt–Bolkow–Blohm
MEMS	Micro-Electro-Mechanical Systems
MMA	Method of Moving Asymptotes
NGTO	Non-Gradient-based Topology Optimization
OC	Optimality Criteria
PolyMUMPs	Polysilicon Multi-User Micromachining Process
PR	Piezoresistive
PP	Post Processing
PSG	Phosphosilicate Glass
PVD	Physical Vapor Deposition
RAMP	Rational Approximation of Material Properties

RF	Radio Frequency
SA	Simulated Annealing
SE	Structuring Element
SIMP	Simplified Isotropic Material with Penalization
SOI	Silicon On Insulator
TO	Topology Optimization
VF	Volume Fraction

1 Introduction

Inertial sensors have been used for the measurement of acceleration in a wide range of applications. The measured acceleration can be used directly, such as crush detection in car airbags, or it can be integrated to find velocity and displacement, such as navigation systems. New manufacturing techniques and design technologies made it possible for accelerometers to be used in small movement detection applications. A developing application of inertial sensors is to measure the small displacements and velocities to predict landslides and the collapse of civil structures. In the detection of small movements for such applications, the inertial sensor should be able to measure very small accelerations with high resolution. Among the available inertial sensors, Micro-Electro-Mechanical Systems (MEMS) are capable of being used commercially in this application with a small size and reasonable price. Examples of using MEMS inertial sensors for landslide monitoring and structural health monitoring reviewed later in this chapter. Due to the limitations of mass and fabrication methods, MEMS accelerometers still need to be improved in sensitivity and resolution for very small acceleration detection. Topology optimization as a mathematical method has been used in the design of mechanical structure of MEMS sensors with specified design objectives and constraints. Reviewing the topology optimization algorithms and similar cases showed that available methods are not applicable to this optimization problem. The main goal of this study is to develop an efficient topology optimization technique for improving the sensitivity of MEMS accelerometers with several constraints in manufacturing and lateral sensitivity. The optimization parameters are analyzed for investigation of convergence in the topology optimization process.

In this chapter, the landslide phenomenon and available monitoring systems are introduced first. Then, the application of inertial accelerometers in landslide monitoring is reviewed in the literature. Structural health monitoring systems with a similar application are also investigated. After reviewing some similar applications, the required specifications of the inertial sensor are listed. The next section reviews different configurations of inertial sensors with their advantages and disadvantages. Based on this review, the proper design concept is selected. Then topology optimization is introduced with its possible effect on the improvement of accelerometer performance. The proper topology optimization method for this work with more details is presented in the next chapter. A developed algorithm to improve this method is also presented. Finally, a summary of the microfabrication methods and their limitations which should be considered in the design for manufacturability is presented. These limitations were applied to the final design using filters and image processing techniques.

1.1 Landslide

Landslide is a general word for any sudden movement or slip of ground. Each year occurrence of landslides endangers people's lives and assets. Landslides are making almost 17% of all fatalities from natural hazards all around the world [1]. Lots of landslides occur in Brazil triggered by torrential rain and make disasters in urban areas [2]. This is the motivation for a project to develop technologies for landslide monitoring at Institute for Technological Research(IPT, Instituto de Pesquisas Tecnológicas), Sao Paulo, Brazil. To study landslides and find possible methods to monitor them, it is necessary to determine the type and specifications of a landslide. Definitions of landslides are different from the point of view of geologists, engineers, and other professionals. This diversity in definitions shows the complexity of the landslide phenomenon and its behaviors [3]. A landslide is defined as the down-slope movement of soil, rock, and organic materials affected by gravity. Classifications of landslides are usually considering specific mechanics of slope failure and the properties and characteristics of failure types. The type of landslide determines the potential speed of movement, the volume of moving materials, the distance of movement, as well as the possible effects of the landslide on the surrounding area [3]. In this section, different types of landslides are described and a brief description of occurrence places, velocity of travel, triggering mechanism, effects, and predictability of each type are discussed.

1.1.1 Falls

When soil or rock detaches from a steep slope along a surface on which little or no shear displacement has occurred, the fall occurs. Then, the material descends mainly by falling, bouncing, or rolling. There are two main types of falls; rockfall and topple. In rockfall, rock or earth moves downward rapidly. It starts by undercutting slopes through natural processes (such as freeze/thaw cycle, stream, earthquake, etc.) or human activities (such as excavation during road building). Falls can damage property beneath the fall line of large rocks. Boulders can bounce or roll for great distances, damage structures, or kill people. The damage from falls on roads and railroads is particularly serious and mostly prevented by avoiding the area or building barriers. Mapping of hazardous rockfall areas has been completed in most of the susceptible areas to be considered in future road constructions. In topple, a mass of soil or rock rotates around a point or an axis below the center of gravity of the displaced mass. It occurs in steep places and their speed depends on the distance that the mass travels. Monitoring topple-prone areas by using tiltmeters is useful in topple. Tiltmeters are used to record changes in slope inclination near cracks and areas of the highest vertical movements. These changes can be monitored for the prediction of upcoming falls and can protect people with safety alarms [4]. A network of highly sensitive and accurate sensors can be used to measure tilts in susceptible areas.

1.1.2 Slide

A slide is a down-slope movement of a soil or rock mass that occurs on ruptured surfaces or in relatively thin zones of intense shear strain. There are two main types of slides, rotational and translational. In a rotational slide, the slide movement is rotational about an axis that is parallel to the contour of the slope. The head of the displaced material may move almost vertically downward, and the upper surface of the displaced material may tilt backward toward the scarp. This type of slide is usually slow and triggered by saturation of slides that happens during heavy rain or a rise in the level of a stream. Historical slides are the most possible places where this type of slide occurs and they should be monitored to detect any movement and prevent possible damages (especially saving people's lives) [3]. In a translational landslide, the mass moves along a relatively planar surface with little rotational movement or backward tilting. This is the most common type of landslide that occurs in all environments and conditions. Translational slides commonly fail along geologic discontinuities such as faults, joints, bedding surfaces, or the contact between rock and soil. They move initially slow or with moderate speed and increase speed during the movement. They usually begin after heavy rainfall or other phenomena that put too much water in the ground such as human-related disturbances. The initially slow landslide could destroy property and endanger people when increasing its speed. The prediction of the translational slide is similar to the rotational slide that uses monitoring systems in susceptible areas [3]. The data of movements collected by motion sensors can be processed to predict dangerous slides and save lives and properties. Slides also can make changes in the environment and in some cases, an early prediction gives enough time to control it.

1.1.3 Spreads

Spread is the lateral movement of cohesive soil or rock to the softer underlying material. Spreads may result from liquefaction or flow (and extrusion) of the softer underlying material. Types of spreads include block spreads, liquefaction spreads, and lateral spreads. In a spread, a slow or rapid landslide occurs where there is liquefiable soil and frequent earthquake. Avoiding to build structures and roads near susceptible areas is the most efficient way to reduce damages of a spread. In addition, they can be avoided by strengthening the structures in the design [3]. Severe spreads endanger many lives and can be predicted by measurement of soil water content and movements of slides.

1.1.4 Flows

A flow is a continuous movement of soil with short-lived shear surfaces. The velocity of moving mass is mostly similar to the viscous movement of liquids. Often, there is a gradation of change from slides to flows, depending on the water content, mobility, and evolution of the movement. There are different flows regarding their size and mechanism

of operation. Debris flow is a form of rapid mass movement in which loose soil, rock, and sometimes organic matter combines with water to form a slurry that flows down-slope. They occur all around the world, especially in steep gullies and canyons. Debris flows are rapid and depend on consistency and slope angle. Intense surface-water flow causes debris that could move buildings or fill them with sediment. It usually occurs frequently in the same area in heavy rain and with a steep slope. To prevent potential damage, construction should be avoided in such places and monitoring systems can be used to detect increasing movements or soil water content. Lahars or volcanic debris are another type of flows that originates on the slopes of volcanoes. They are triggered by water and move at high speed. In order to reduce the potential damages, it's essential to consider areas that have a history of lahars and use an active monitoring system to warn before it happens [5]. Debris avalanches are essentially large, extremely rapid and often open-slope flows formed when an unstable slope collapses and the resulting fragmented debris is rapidly transported away from the slope [3]. Their speed of movement is relatively high and they can destroy cities and endanger people's lives. Construction should be avoided in valleys on volcanoes or steep mountain slopes to prevent damage. Also, a real-time monitoring system can alarm people to evacuate the place before the occurrence [4]. Earthflows move mass as a plastic or viscous flow with internal deformation. Susceptible marine clay is very vulnerable and may lose all shear strength with a change in its natural moisture content and suddenly liquefies, potentially destroying large areas and flowing for several kilometers. Earthflows can range from very slow (creep) to rapid and catastrophic. Earth flow starts with the saturation of soil during a long period of rainfall or any other natural/human-made phenomenon that adds too much water to the soil. They damage constructions and endanger people's lives. Even though the best way to reduce damages is to avoid the construction of buildings in susceptible areas, for places that are already settled it's applicable to measure the shear strength of clay and monitor the area for evacuation before earthflow and save people's lives. In a slow earth flow, they can damage pipelines and displace constructions that cause damage over a long time. In this case, the earth flow should be detected by monitoring systems like inclinometers installed in boreholes and affected constructions must be inspected for potential damages [5], [6]. As discussed in this section, for many types of landslides, it is possible to reduce damages and save lives by monitoring susceptible areas and early warning systems. The parameters such as water content, movements, and slope have major effects on the landslides and should be measured in a landslide monitoring system. The next section reviews available methods to measure these parameters in previous works and specifies the properties of the sensors for reliable measurements.

1.2 Landslide monitoring systems

Damages of landslides can be reduced by avoiding settlements and transits near susceptible areas as the primary solution. But there are urban areas already constructed in such locations. Also, there are some locations where passing beside a susceptible area is inevitable for geographical or political reasons. And, most importantly, climate change due to global warming changed safe urban areas to areas susceptible to severe floods and landslides. In such areas, the occurrence of a landslide is possible every moment and can be enhanced by external parameters such as heavy rainfalls. In such situations, landslide monitoring can predict a landslide by measuring movements, the water content of the soil, and any other relevant parameter that can trigger a landslide. Prediction of a landslide can help people to evacuate the location to reduce damages and save lives. In this section, a summary of landslide monitoring systems and available prediction systems are reviewed and they are compared according to their advantages and disadvantages.

The most important parameter in predicting landslides is the movement of slides over time. Measurement of movements with enough resolution and at a reasonable price is the first step in landslide monitoring. Different methodologies have been used in the literature to measure landslide movements. Clark et al. [7] adopted tiltmeters to measure the displacement of the ground surface in the south and east coast of England. They studied ground movement threshold that shows the trigger of a landslide. Angeli et al. [8] used two multiple-base wire-extensometer units to measure landslide movements as small as a centimeter in the Tessina region, Alpago valley of NE (Italy). They also installed an automatic topographic system to measure surface movements. A camera recorded target infrared light at 6 hours intervals (and 1-3 hours during emergency periods) and sent results to a database to be analyzed. Their system was able to continuously monitor landslide and predict some critical situations. Despite proved applicability of their system, maintaining steel wires in the extensometer is costly. In addition, the complementary topographic system does not work properly in intense rainfall or foggy weather. Angeli et al. [9] drilled a number of horizontal and vertical boreholes and installed long fiber-glass extensometer bars to measure the movements of the Sirolo landslide, Italy. This type of extensometer is usually used in the monitoring of structures by civil engineers and this team used it successfully for landslide movement measurement in order of hundreds of a millimeter. They showed this method is useful for rock-slide applications. They also used rain gauges and pressure sensors to determine the effect of rainfall and groundwater levels on landslides. Needing precision installation makes capital costs for this monitoring system high. Additionally, this system needs periodical maintenance which adds to the monitoring costs. Corominas et al. [10] used a borehole wire extensometer for monitoring the Vallcebre translational slide, Eastern Pyrenees (Spain) and the Alverá mudslide, Dolomites (Italy). They developed some equations to calculate the movements of translational slides from measurements of extensometers within the borehole. Even though this method can

measure the horizontal and vertical displacements of the slides, they cannot be used for large displacements. In addition, initial and maintenance costs for borehole extensometers are relatively high. In another case of landslide monitoring, Zan et al. [11] used a system with a laser diastimeter, geophone, and rain gauge to provide enough information for landslide monitoring. They measured ground displacement and seismic-induced vibrations by means of a laser diastimeter and geophone. Their system starts alarming when the variations exceed the established threshold. This method showed a good performance as a landslide early warning system, but the laser diastimeter is limited to the light transmission of air in the measuring location. Since most landslides occur in rainy areas, a laser system cannot work in many locations [12]. Zhou et al. [13] used a GPS-based landslide monitoring system to monitor the landslide in Sichuan, China. They built 15 permanent GPS monuments in the area to measure the displacement of the landslide with an accuracy level of 2 mm. Using GPS in their research showed fair performance with low costs, but this method is limited to the surface of the slides. On the other hand, Petley et al. [14] showed that landslide movements start from the toe and then retrogress upslope. They got these results by analyzing data collected from piezometers, inclinometers, extensometers, and electronic distance measurement (EDM) from the Tessina landslide. In another approach, Garich et al. [15] developed a system for landslide monitoring by connecting several MEMS accelerometers to a wireless system. They combined each sensor with a low-power data transmitter for real-time monitoring. Their work showed good compatibility of MEMS sensors for remote geotechnical applications, especially landslide monitoring. Arnhardt et al. [16] reviewed different types of early warning systems. By comparing of pros and cons of each method, they concluded that accelerometers are the best choice for displacement measurement in transportation infrastructures and similar applications such as landslide monitoring. Yin et al. [17] used a combination of GPS and an inclinometer to monitor a landslide in the Tree Georges Reservoir area, China. They measured the water level, the water pressure, and the ground displacement (GPS for surface measurement and inclinometer for deep measurement). They showed that by analyzing these data, the prediction of a landslide is more accurate. Georgieva et al. [18] developed an autonomous landslide monitoring system using wireless sensors. They used ground acceleration and orientation of sensor nodes as input data to automatically predict a landslide. In landslide prediction, they used the method presented by Fukuzono [19] to use changes in velocity as a parameter to predict landslides. They showed that the accuracy of this method is highly dependent on the accelerometer's resolution. Photogrammetry is another method that has been used by researchers for landslide monitoring. Travelletti et al. [20] analyzed ground-based optical images of the Super-Sauze landslide, south French Alps. They showed acceptable performance of this method but realized that meteorological, illumination, and ground surface conditions limit the application of this method. In a similar work, Peppia et al. [21] used photogrammetry to monitor a landslide movement in

Hollin Hill, UK. They showed that this method comes with a few centimeters of accuracy in displacement measurements. Another problem of this method was discovered to be seasonal vegetation that cannot be completely filtered out. To improve the early warning systems, recent methods are focusing on the analysis of several parameters and their relation to predict a landslide. Srinivas and Raghava Rao [22] developed a Zigbee hardware module to communicate between different sensors. The detected disturbance in accelerometer sensors, water level sensors, or temperature sensors will start the analysis of all data to predict the possibility of landslides. Chae et al. [1] reviewed information on susceptible areas and failure mechanisms. They concluded that physically based models have a higher predictive capability and displacement measurement is the essential parameter in physical models. If the displacements can be recorded at a higher resolution, they can be used in available models. A model proposed by Kirschbaum and Stanley [23] combines satellite-based precipitation estimates with susceptibility map. This method monitors near real-time and is accessible for public use, but it did not predict majority of landslides because it just uses rainfall information of the area. It would be more applicable by adding variables like seismic activity [23]. Some other researchers also used similar methods (rainfall thresholds as failure criteria) to predict landslides [24]. Krkac et al. [25] developed a model to predict landslide movements in Kostanjek, Croatia. They applied a random forest method to the data obtained from landslide movement, groundwater level, and precipitation. This model can predict a landslide if the measurements are accurate, especially velocity and displacement. Besides the accuracy of landslide prediction, recent researchers are developing monitoring systems with lower costs to be used easily in any susceptible area. Since Brazil is a country with lots of urban areas with the possibility of landslides, researchers are testing different methods to predict landslides with the possibility of usage in large scales. Otero [26] et al. made experiments to predict landslides with the analysis of low-cost accelerometers. They made different experiments with different angles and added water to the soil to measure accelerations. They showed that acceleration can be used to find velocity and displacement of movements and can be used as a signal in early warning systems. They also showed that the acceleration data are close to each other and the resolution of the measurements has an important effect on the prediction's accuracy. According to their experiments and models, higher accuracy of accelerometers would be enough to detect pre-failure signals with high reliability of performance. The data can be analyzed by Recent development in data analytics to generate high-quality information from the large dataset [27, 28].

1.3 Structural health monitoring with accelerometers

Displacement information collected by the accelerometers showed good performance to be used for structural health monitoring. Megastructures such as dams and bridges undergo

movements from creep or vibrations. These movements are normal in most cases and are considered in the design of structures. But there are cases that a movement can be a sign of failure. By measuring and monitoring displacements in real-time at various locations of a structure, failure can be predicted [29]. The failure of a large structure can cause severe damage to people and the environment. Dam failure can cause floods and destroy infrastructures downstream. A recent example of dam failure is the Brumadinho dam collapse in Minas Gerais, Brazil. This disaster caused the death of 270 people and damaged the downstream environment by releasing around 12 million cubic meters of tailing [30]. In a similar case of the collapse of the Mariana tailing dam, the tailing slurry moved approximately 620 km downriver and damaged a large area of rivers and forests [31]. Such disasters can be predicted by an early warning system to evacuate the area and save lives in the first stage, and secondly, reduce damages if possible. Similarly, in the case of bridge failure, an early warning is helpful in preventing possible damage. Using displacement data shows the deformation of bridges and could be used in mathematical models to predict their collapse [32]. Measured data should be interpreted for the prediction of potential hazards. So, the required data and its accuracy is important in structural health monitoring [33]. Dam safety management systems use 3-dimensional surface deformation data to monitor dams' condition [34]. History of dam failures shows that earthen dam failure generally happens due to overtopping, internal erosion, and piping [35]. Even though these mechanisms are different, the failure of dams could be predicted using the displacement history of surfaces. With the development of sensing technologies, the management and safety of geotechnical infrastructures (levees and earthen dams) are improved. MEMS accelerometer sensors play an important role in the case of structural health monitoring [36]. The feasibility of embedding MEMS devices into concrete material for conditioning and health monitoring of civil infrastructures is investigated by Saafi and Romine [37]. They showed that MEMS sensors have sufficient chemical and moisture resistance to be used in such applications. Additionally, damage to the structure does not affect its performance, and it can continue the measurements for failure detection. Abdoun et al. [38] used MEMS sensors for simultaneous measurement of 3D soil acceleration and 3D ground deformation up to a depth of 100 meters with an accuracy of $\pm 1.5mm$ per 30m. Their system is capable of measuring 3D ground deformation at 30cm intervals and acceleration at 2.4m intervals to a depth of 100m. The only measurement of relative displacement is possible using these sensors, and so, the reference end of the array should be accessible in a stable layer to get accurate data. Their system is cost-effective for continuous monitoring. Additionally, the sinusoidal response of MEMS accelerometers causes the slope of the sine curve to be less degraded than that of traditional accelerometers (just 1.5% for 10 degrees and 29% for 45 degrees of deviation) when they deviate from the vertical or horizontal installation. This is very advantageous when the system will be left in place permanently and the casing becomes extremely distorted. More recent research

on structural health monitoring is mostly using MEMS sensors as an accurate, low-cost, low-power consumption, and easy-to-connect solution [39]. Nuzzo et al. [40] used a 3-axis accelerometer with a wireless connection as a low-power and cost-effective device for structural health monitoring. Villacorta et al. [41] used ADXL355 MEMS accelerometer with $\pm 2g$ range for modal analysis of structural health monitoring. They showed the acceptable performance of the MEMS accelerometer system with almost one-tenth of the capital cost of the conventional piezoelectric accelerometer system. Parisi et al. [42] showed up to 80% reduction of power consumption by using MEMS accelerometers instead of piezoelectric ones in structural health monitoring systems. Komarizadehasl et al. [43] used a combination of five gyroscopes and five accelerometers to measure inclination. They showed that the system with MEMS accelerometers can be accurate enough for damage detection of bridges at a considerably lower cost than a commercial inclinometer (HI-INC). Pleuger et al. [44] used a MEMS accelerometer with a range of $\pm 4g$ to measure accelerations of a bridge over a long period of time. Then they used filters to reduce noise and integrated acceleration data to obtain velocity and displacement. They showed that using a Kalman filter can improve the accuracy of measurements in the dynamic loading condition. In summary, MEMS accelerometers are becoming the most popular device for structural health monitoring systems. In addition to the methods developed for filtering and data analysis, the improvement of the mechanical sensor increases the accuracy and applicability of MEMS accelerometers in the future generation of structural health monitoring systems.

1.4 Required specifications of an accelerometer for landslide monitoring and structural health monitoring

In the previous sections, some literature on landslide monitoring systems and structural health monitoring was reviewed. They showed that using MEMS accelerometers are becoming a popular solution for real-time monitoring in early warning systems. In this section, the characteristics of the required accelerometer for such applications are determined from the previous systems. Available off-the-shelf MEMS accelerometers are not designed specifically for this application, but based on the data type and previous similar works, it is possible to determine important required specifications. Arnhardt et al. [45] developed a network of sensors for real-time monitoring of landslides. They used MEMS silicon capacitive sensors to measure acceleration. The 3-axis acceleration sensor used in their work had a sensitivity of $1333 \frac{\text{counts}}{g}$, acceleration range of $\pm 2g$, and bandwidth of $45Hz$. The tested accuracy for the acceleration measurements was $\pm 0,008g$. Their work showed that accelerometers and especially MEMS ones could be used for landslide monitoring with enough accuracy. The sensitivity expressed in the unit of least significant bit per g in a digital output is equal to about $36 \frac{mv}{g}$. Bennett and Abdoun [46]

installed a long device inside the soil for measuring 3-D soil permanent deformation and accelerations. Using a MEMS accelerometer made the installation of this device easier due to the fact that the accuracy of measurement does not change significantly when the device deformed from a horizontal or vertical angle. They installed the sensor array on a shaking table and exited the setup by $0.08 - 1.4g$ acceleration and $0.5 - 2.5Hz$ frequency. They also tested this device with an earthquake simulator and in-site experiments. The obtained data from the field test showed an accuracy of $\pm 1.5mm$ per $30m$. The MEMS sensor used in their work was in the range of $\pm 2g$, $20Hz$ of $3dB$ bandwidth, and $0.01deg$ of tilt resolution. Tran et al. [47] selected a 3-axis capacitive type of MEMS accelerometer for landslide monitoring because of its high sensitivity, low power consumption, and low temperature dependence. They used a sensor with $\pm 3g$ measurement range and sensitivity of $SX = 0.336 \frac{V}{g}$, $SY = 0.337 \frac{V}{g}$, and $SZ = 0.329 \frac{V}{g}$. Their sensor network tested for the detection of unknown vibration signals, tilt measurement, and displacement measurement. Displacement is calculated by double integration of acceleration, so accumulated errors are considerable in this application. They suggested a smart method that reduces the sample rate in normal conditions to reduce noise and power consumption. Li et al. [48] used a 3-axis accelerometer with $\pm 2g$ measurement range and $900 \frac{LSB}{g}$ sensitivity for geotechnical monitoring of ground subsidence. This is equivalent to about $25 \frac{mv}{g}$. They used the Kalman filter to reduce the noise of sensor nodes for improving the accuracy of displacement measurements. Alippi et al. [49] developed a MEMS accelerometer with $\pm 2g$ acceleration range, $0.66 \frac{V}{g}$ rated sensitivity, $50\mu g/\sqrt{Hz}$ rated noise density, and $1.5KHz$ resonance frequency for monitoring of microseismic activity of structures (and similarly slopes activities). Kotta et al. [50] used accelerometers for monitoring a specific landslide. They did some experiments that showed $0.2 - 0.4g$ acceleration is for the beginning of soil movement. For a significant change of ground motion, the value of acceleration is above $0.5g$. Above $1g$ of acceleration of ground motion indicates a very strong activity of landslide. Because the capacitance-based MEMS accelerometers are not as sensitive as piezoelectric or piezoresistive to temperature, and also the working temperature does not change rapidly in landslide detection applications, temperature compensation is not necessary in this case. The signals that are reported in the literature are up to $35Hz$ and measured with the upper limit of $50Hz$. The peak values of the signal reported around $5Hz$ [51]. The upper limit of $45Hz$ is also used for measurements in another case and proved the sufficiency of this upper band [45]. To sum up, a measurement range of $\pm 2g$ and $50Hz$ of bandwidth is required for landslide and structural health monitoring. Since measurement of velocity and displacement is desired for this application, a DC-response is required. A sensitivity of more than $0.600 \frac{V}{g}$ is acceptable for this application. The transverse sensitivity is $5 - 10\%$ for commercial models and less than this value is more desirable. Table 1 shows a summary of minimum requirements for the MEMS sensor used in the previous landslide monitoring systems.

Table 1 – The required specifications of inertial accelerometer sensor for landslide and structural health monitoring.

Required specification	Value	Unit
Measurement range	± 2	g
Bandwidth	0-50	Hz
Sensitivity	> 0.6	v/g
Transverse sensitivity	$< 5-10$	$\%$

The specifications mentioned in Table 1 are from the previous successful use of MEMS accelerometers in landslide and structural health monitoring systems in the literature. But higher sensitivity, lower noise, and lower transverse sensitivity are more desirable for increasing the resolution of measurements and increasing the chance of prediction of a landslide or collapse in a structure. The research project performed by the geologists at IPT showed a need for higher sensitivity and lower cross-axis sensitivity in accelerometers to get a reliable measurement of movements and changes in slopes. Improvement of these specifications could be done by changing the mechanical structure of the sensor or electronics. Each approach has its limitations and can improve some specifications. In this study, the mechanical unit in a MEMS sensor has been improved by topology optimization design techniques. The main target is to increase sensitivity in the measurement direction and reduce cross-axis sensitivity. Convergence to a feasible solution adds manufacturing and displacement constraints to the optimization problem. The next chapter introduces available concept designs for MEMS accelerometers. Then the out-of-plane design is selected based on the required specifications of the sensor in landslide monitoring. In the next section, available optimization methods are introduced. Then gradient-based and non-gradient-based topology optimization algorithms are explained with their application in topology optimization problems. Variable loading and manufacturability are two important parameters in this design that explained in the next section. Then the microfabrication process and specifically surface micromachining is introduced as the manufacturing method of the MEMS sensor. Manufacturability constraints from the lithography process are explained and some trial experiments have been performed at the laboratory to show the manufacturing limits numerically and graphically. Morphological operators are considered as an image processing method to consider the behavior of etching in lithography. In chapter 3, a new algorithm is proposed for meta-heuristic topology optimization to find optimum solutions for a structural design. The methodology was validated by benchmark problems from the literature. Then, a post-processing method was developed by using density filters and morphological operators to apply manufacturing constraints. This post-processing method tested several designs obtained from topology optimization and simulated for a completed lithography process. A binary algorithm is also proposed

to generate manufacturable designs directly where post-processing changes the design considerably. In the next section of chapter 3, the design parameters selected for the MEMS accelerometer and the objective of optimization are determined by analyzing the objective of design and its convergence in some generative designs. Then, a combination of different objective functions and constraints was used to design three MEMS accelerometers. The convergence of the topology optimization problem was analyzed to determine the type of optimum solution and the possibility of having alternative designs. Finally, the performance of each design was simulated and compared with the available designs in the literature. In the end, the conclusion of this research is presented following some suggestions for future works.

2 Theory and Background

This chapter provides the theory and mathematical formulations used in this research. A brief description of accelerometers, topology optimization, manufacturability, and micro-fabrication is presented with recent research in each subject. The first section introduces the concept design of an accelerometer and common mechanisms in the measurement of acceleration. It also shows the common suspension structures used in the design of an accelerometer. A literature review on the design and topology optimization of MEMS accelerometers shows up-to-date designs with pros and cons. In the next section, the topology optimization method is selected as an automatic method in design. Various optimization algorithms were reviewed from the literature. A non-gradient topology optimization method based on simulated annealing was selected as an efficient algorithm in a multi-constraint and non-convex optimization problem. Then, the variable loading situation was reviewed as it is an important case in this design. At the end of this chapter, the microfabrication process is introduced for manufacturing MEMS accelerometers and the limitations are investigated from lithography experiments.

2.1 Accelerometer and possible configurations

An accelerometer is a device that measures the rate of change in velocity over time or acceleration of a structure relative to an inertial reference frame. The mechanism of operation in an accelerometer is suspending a proof mass with springs to the reference frame. Applying an acceleration to the structure results in a force in the same direction proportional to the mass and acceleration according to d'Alembert's principle shown in Eq. (2.1).

$$\vec{F}_{net} = m\vec{a} \quad (2.1)$$

where F_{net} is the net force, m is the mass, and a is the applied acceleration vector. The inertial force from Eq. 2.1 causes motion in the suspended mass. The dynamic model of the system can be demonstrated by a second-order mass-spring-damper system. The mass (m) is the proof mass, spring (K_m) comes from the stiffness of the suspension structure, and damper (c) is the damping effect of the friction interaction with the surrounding medium and hysteresis effects inside the crystal lattice structure. The equation of motion for this second-order dynamic system can be written using Newton's law of motion as Eq. (2.2).

$$m \frac{d^2x(t)}{dt^2} + c \frac{dx(t)}{dt} + K_m x(t) = ma(t) \quad (2.2)$$

where $x(t)$ is the displacement over time in the direction of motion relative to the inertial reference frame. The displacement of the proof mass can be measured to find the applied

acceleration. Various concept designs are available to measure the displacement, and each method can be efficient based on the type of acceleration signal. Basically, accelerometers are divided into two main categories of AC-response and DC-response. AC-response accelerometers have an ac-coupled response which is suitable for the measurement of dynamic motions with a wide range of frequencies. The full-scale range of these accelerometers can be adjusted by electronic parts. AC-response accelerometers mostly use piezoelectric materials as sensing elements. Piezoelectric materials are Lead Zirconate Titanate ceramics (PZT) in a wide range of application and Quartz or Tourmaline for harsh temperature environments. The output of piezoelectric sensors are charges that can be transmitted by a low-noise shielded cable or can be converted to a low impedance voltage using onboard integral electronics. The output of an AC-coupled device cannot track a signal completely because of the intrinsic limits of the RC time constant. Thus, the output of ac-coupled accelerometers comes with an undershoot (offset) error. This small error would be accumulated where the measured acceleration is integrated to calculate velocity or displacement. The DC-response (DC-coupled) accelerometers, on the other hand, can measure both static and dynamic acceleration because of having a performance range of down to 0Hz . Among the available technologies for dc-coupled acceleration measurement, piezoresistive and capacitive are the most common ones. Piezoresistive (PR) elements sense an acceleration signal by measurement of resistance change in a strain gauge. Piezoresistive accelerometers are able to measure accelerations from 0Hz up to 7KHz with a good signal-to-noise performance. The dynamic range of piezoresistive accelerometers is only limited by the quality of DC bridge amplifier. They are mostly used in acceleration measurements such as automotive safety tests. Since piezoresistive accelerometers are dc-coupled, they can be used in the calculation of velocity and displacements without integration errors. The piezoresistive accelerometers are sensitive to temperature variations due to the mechanism of performance. They usually need additional internal or external parts for temperature compensation which makes their design more complex. In addition, piezoresistive accelerometers have a very low sensitivity that makes them not suitable for accurate measurement of low gravity accelerations. Capacitive based accelerometer is another type of DC-response sensor that measures a displacement by changing capacitance between two electrodes. Capacitive accelerometers are widely used in commercial applications such as mobile devices for low-frequency and steady-state acceleration measurements. They can be fabricated by MEMS technology in high volume and low cost. Capacitive accelerometers have been used efficiently for the measurement of small accelerations. For such applications, the accelerometer should be designed with high sensitivity and low noise to improve the accuracy of measurement. Among the available accelerometer types, the capacitive mechanism has been selected in this work because of its high sensitivity, low power consumption, low-temperature dependence, good dc-response, and fair noise performance [47, 52]. In addition, the fabrication method of the capacitive-based sensors is more simple

than piezoelectric and piezoresistive ones [53]. However, capacitive accelerometers may be susceptible to electromagnetic interference (EMI), in addition to requiring a more elaborate electronic device for capacitance readings, increasing circuitry, and packaging complexity [54]. But this is not a concern in the application of landslide monitoring. Capacitive accelerometers could also support a closed-loop operation with feedback force to keep the proof mass in the initial position [55]. In this approach, the required feedback force to nullify the proof mass displacement is used to estimate the acceleration, increasing the bandwidth, linearity, and dynamic range, but also increasing circuit and design complexity. For these features, capacitive accelerometers are preferred for low-g applications, including landslide monitoring. The first step in the design of a capacitive MEMS accelerometer is the conceptual design. The design concept determines the initial characteristics of the design and should be selected wisely according to the desired low motion measurement application. For the measurement of displacement in all directions and calculation of slopes, accelerations should be measured in three perpendicular axes. A single proof mass can be used to measure the acceleration in three perpendicular directions. It will present a more compact device with no risk of alignment error. But it has high cross-axis sensitivity which is undesirable for the low acceleration measurements and very small changes in slope. It also limits the measurement configuration to the in-plane movements in two directions. The mechanical and electrical connections are also complicated and the layout design is not simple. Even in cases where one proof mass has been used for measuring acceleration in the x and y direction and another one for the z direction, the same problems still exist. By using a separate proof mass for each direction, the design would be more simple and with less cross-axis sensitivity [56]. Additionally, the selection of capacitive measurement configuration is more flexible when using a proof mass for measurement in only one direction. Generally, there are three different configurations for the capacitive MEMS sensors; parallel plate, transverse comb, and lateral comb [57]. A parallel plate (out-of-plane) configuration is a plate proof mass suspended by beams parallel to a fixed electrode. The parallel plates are perpendicular to the direction of the acceleration measurement. By applying acceleration, the proof mass (suspended plate) moves in the direction of acceleration according to Eq.(2.2). This movement changes the distance between two parallel plates as shown in Fig. 2.1.

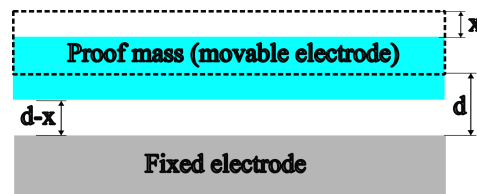


Figure 2.1 – Parallel plate configuration of the capacitive accelerometer.

In the absence of external acceleration, for parallel plates with an overlapping area of A and the initial distance of d the capacitance between two electrodes can be calculated

using Eq. (2.3) by neglecting small fringing effects at the edges of plates.

$$C_1 = k\epsilon_0 \frac{A}{d} \quad (2.3)$$

where k is the relative permittivity which is approximately 1 for air and $\epsilon_0 = 8.854 \times 10^{-12} \frac{F}{m}$ is permittivity of free space. Applying the external acceleration changes the location of electrode by x according to Eq.(2.2). The new capacitance can be calculated similarly by Eq. (2.4).

$$C_2 = k\epsilon_0 \frac{A}{d \pm x} \quad (2.4)$$

The negative sign shows when the direction of acceleration moves the suspended plate toward the fixed plate and the positive sign is for movement in the opposite direction. The change in capacitance from Eq. (2.3) to Eq. (2.4) can be measured using an electric circuit. Then the output signal can be calibrated to calculate the displacement of the proof mass and external acceleration. This parallel plate configuration provides high capacitance between two electrodes due to the large electrode area which can be measured with higher accuracy and it provides higher sensitivity. For the large displacements of the proof mass, the change of capacitance is non-linear according to Eq. (2.4). That makes parallel plate accelerometers limited to a low range of accelerations for approximately linear response. For measurement of higher ranges of acceleration, a feedback electrostatic force can be provided by a closed-loop control system. The electrostatic force applies a force in the opposite direction of the acceleration to keep the proof mass in the initial position. Since this feedback system makes electronics more complex, it is not a common solution. In most commercial applications, other configurations can be used for a high range of acceleration with an open loop system and linear response. In the application of landslide monitoring, the range of accelerations is about $\pm 1g$ and non-linearity is relatively small. Also, pull-in phenomena (pull electrodes toward each other because of electrostatic force) are considerable in parallel plate configuration due to the high overlapping area [58]. This pull-in voltage puts a limitation on the applicable electrical potential between electrodes for capacitance measurement. Pull-in voltage for a capacitive accelerometer is defined as the voltage in which the electrostatic force between plates is more than the spring force of the suspension system and the electrodes stick together. The pull-in voltage can be calculated by Eq. (2.5) for a parallel plate capacitive accelerometer using mechanical spring constant of K_m , the surface area of A , an air gap of d , and permittivity of $\epsilon = k\epsilon_0$ [59].

$$V_{pull-in} = \sqrt{\frac{8d^3 K_m}{27\epsilon A}} \quad (2.5)$$

From Eq. (2.5), the pull-in voltage can be increased by increasing the distance between plates or the stiffness of the mechanical suspension system or reducing the overlapping area of plates. If so, the sensitivity of the accelerometer would be decreased. Thus, a

balanced combination of such conflicting parameters should be designed to provide the required performance.

A transverse comb configuration is another method to measure displacements with a capacitance concept. The transverse configuration uses the same mechanism of changing distance between parallel plates, but for in-plane movements. Since the thickness of the structure is small due to manufacturing limits, a small overlapping area is available for the capacitor. To compensate for low capacitance in each pair of electrodes, comb shape plates with a set of large fingers are used in a transverse comb as shown in Fig. 2.2.

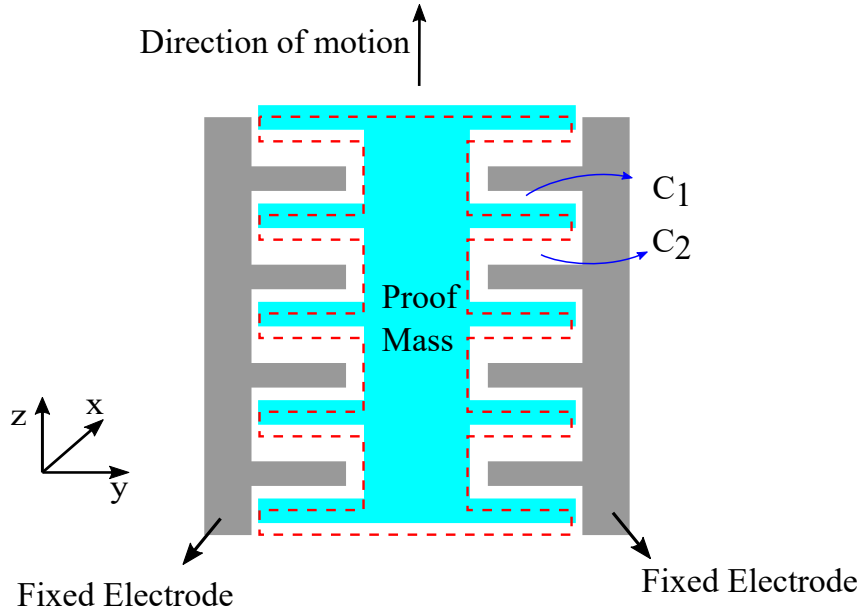


Figure 2.2 – Transverse comb configuration of the capacitive accelerometer.

Application of an in-plane external acceleration perpendicular to the fingers moves the suspended fingers in relation to the fixed fingers and changes the gap between them. The capacitance between each pair of fingers can be calculated from Eq. (2.3) and Eq. (2.4) for without and with external acceleration situations, respectively. The total capacitance is the summation of the capacitance between each pair of fingers. The main advantage of transverse comb configuration is having more controllable pull-in voltage [60]. Because of the differential topology, the force-displacement relationship is linear. The sensitivity of the transverse comb accelerometers also can be improved by the separation of electrodes to make two sets of parallel accelerometers with increasing and decreasing acceleration, respectively [61]. Since the capacitance changes according to Eq. (2.4), the non-linearity exists in the change of capacitance similar to the parallel plate configuration and limits the range of performance for linear measurements. In addition, the transverse comb configuration has small overlap areas that increase the fringing field effect at the border and adds more non-linearity to the measurement of changing capacitance. This fringing field effect can be reduced by using high aspect ratio fingers (thicker structure), but it is limited by the fabrication methods, especially in the case of MEMS sensors

[54]. So, the transverse comb configuration is not a proper case for landslide monitoring applications. Another common configuration for capacitive accelerometers is the lateral comb configuration. As shown in Fig. 2.3, lateral comb configuration uses a structure similar to the transverse comb to measure in-plane movements.

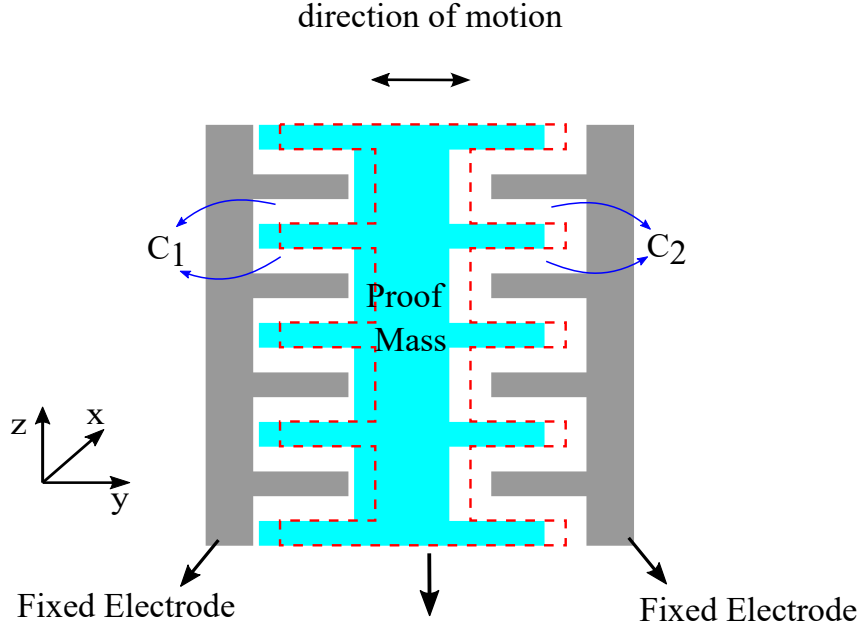


Figure 2.3 – Lateral comb configuration of the capacitive accelerometer

The only difference between the lateral and transverse comb configuration is that in the lateral comb, the fingers are parallel to the direction of measurement, and movement of proof mass changes the overlapping area of the capacitors. So the capacitance of each pair of fingers after the movement can be calculated from Eq. (2.6).

$$C_2 = k\epsilon_0 \frac{A_2}{d} = k\epsilon_0 t \frac{l_2 \pm l_1}{d} \quad (2.6)$$

where t is the thickness of the finger and l_i is the overlapping length of fingers. The main advantage of lateral comb configuration is the linear response in any range of acceleration. Additionally, the pull-in effect is not in the sensitive direction and higher voltage can be used in the measurements without sticking electrodes. But the fringing field is considerable in this configuration and adds some non-linearity to the measurements. Also, the change of electrostatic force in each position adds motion instability issues. So, the movements are limited. This configuration provides low sensitivity to small acceleration and is usually used in high acceleration sensors or as an actuator.

All of the capacitive accelerometer sensors use one of the mentioned configurations or a mixture of them depending on the application. By comparison of the advantages and disadvantages of these three configurations, it can be concluded that the parallel plate configuration represents a good performance for the measurement of weak acceleration signals with acceptable accuracy. The parallel plate configuration also gives more flexibility

to change the topology for improvement of the performance. So, the parallel plate configuration has been selected in this project to be designed by topology optimization for low motion detection in landslide monitoring and similar applications.

2.1.1 Suspension systems and optimized designs in the literature

The geometry and size of the suspension structure (spring) have a high effect on the performance of an accelerometer. A common approach in the design of MEMS sensors is to select a suspension beam and change dimensions to reach the desired performance [62]. This approach results in a satisfactory design in most cases but not necessarily the most efficient one. There are several suspension models that are used commonly in the previous designs [62]. A straight beam, crab-leg beam, folded beam, and serpentine are the most common suspension elements used in the literature [60]. Fig. 2.4 shows a simple schematic of each suspension beam design configuration.

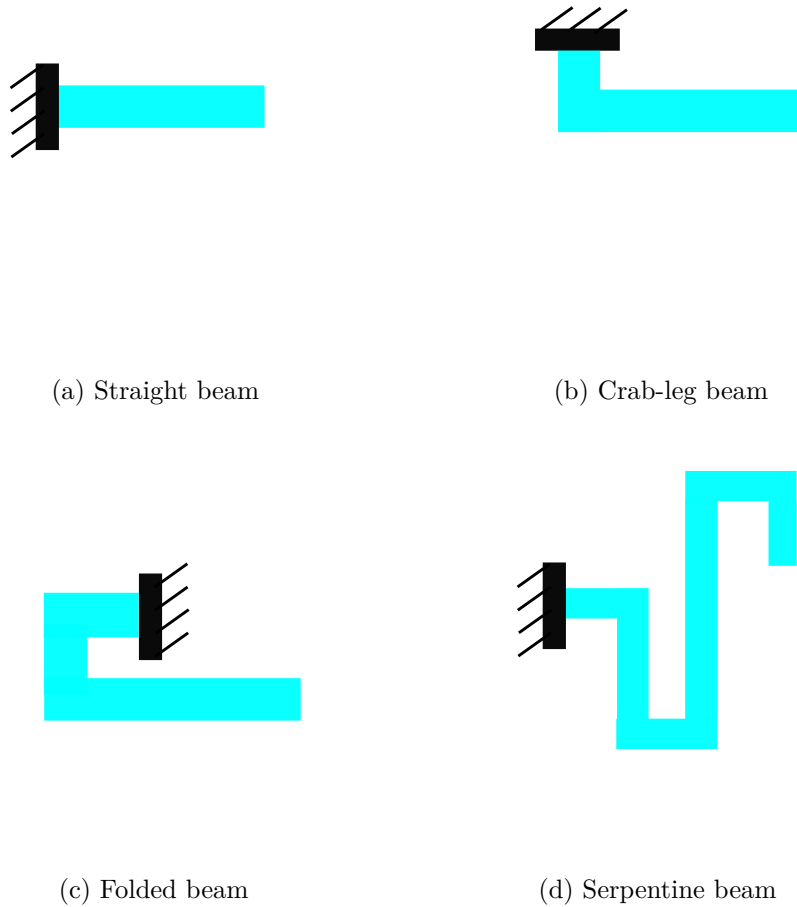


Figure 2.4 – Schematic of beam configurations used as suspension structure

Each configuration in fig. 2.4 represents some behaviors that can be useful for a different application. The straight beam is beneficial where linear bending of the beam is

required. For example, in piezoelectric and piezoresistive measurement methods bending of the straight beam can be measured easily. But in the other configurations, the beam undergoes rotation and the beam does not bend linearly. Crab-leg and folded beam configurations provide larger displacements and have lower peak stress on the beam [60]. The crab-leg and folded beam configurations are mostly used in the design of sensors with capacitive measurements because in such designs movement of the proof mass would be measured directly and independent of the bending of the suspension beams. The serpentine configuration benefits from providing large displacement in a compact area. In this design, the peak stress is also lower but the lateral displacement can be high [63]. In a real design situation, a combination of these configurations can be used to obtain a specific desired motion of the proof mass. The symmetric arrangement of suspension beams around the proof mass provides an equal distribution of stress and reduces lateral movements. It also can increase the sensitivity difference between the dominant direction of movements from the lateral one. There are some researches in the literature focusing on the design of suspension systems to maximize one or a set of desired performances. Most of the optimization research has been done on the design of suspension systems started from an initial design with predefined numbers and shapes of suspension beams. Then, an optimization algorithm finds the best combination of dimensions to maximize a performance such as sensitivity, bandwidth, etc [64, 52, 65, 66]. Besides their improvement in performance, these size optimization approaches are limited to the initial design and do not necessarily reach the best possible design. Pak et al. [67] used a multi-objective evolutionary algorithm to optimize the size of suspension beam in a fixed geometry. Their work used a simple model of an accelerometer with constant force and optimized dimensions for minimum noise and surface area. The Pareto front for their optimization shows the minimum noise for each surface area. Gomathi et al. [68] designed a capacitive accelerometer with a fixed proof mass at the center and suspended by two folded beams. They increased sensitivity by changing the dimension of beams and proof mass. Their design showed a set of dimensions with maximum sensitivity. But this design is limited to the initial shape. Hu et al. [69] used different sizes and shapes of suspension beams to increase the sensitivity of a bulk micro-machined sensor. This design used crab-leg beams as the initial design and only sizes are changed to increase the sensitivity. Lu et al. [64] optimized dimensions of a bulk micro-machined accelerometer with crab-leg and serpentine suspension structure. They showed that an ultrasensitive out-of-plane MOEMS (micro-optical electro-mechanical system) sensor can be achieved by finding efficient sizes of the proof mass and suspension structure. This method is only applicable to a predefined shape and is limited to the initial design. Zou and Seshia [70] designed a seismic-grade accelerometer to be built with bulk micromachining. They used a leverage mechanism for the suspension structure to reach desired properties for the seismic application. The size optimization is able to find the optimized design while it is strictly limited to the initial

configuration. This strategy can improve available designs for better performance but is not suitable for generative design and finding the best possible design.

A more flexible approach to finding the optimum geometry and size of the suspension structure in a MEMS accelerometer is topology optimization (TO). This method is a mathematical algorithm to determine the distribution of material (size and position) to reach maximum performance. There are a variety of algorithms in TO used in the literature and discussed in the next section. In a few cases, TO was applied successfully in the design of MEMS sensors with different targets. Fujiyoshi et al. [71] used TO in the design of an accelerometer to reduce bias drift. In their work, a stress isolation suspension structure was added to the design to reduce the bias drift in temperature changes. Their accelerometer is already designed for mechanical behavior and performance and the TO is used for the reduction of bias drift. Philippine et al. [72] used TO in the design of stressed capacitive RF MEMS switches. They utilized TO to minimize stress stiffening and curling. They considered a constant force from the constant actuation area and TO was used to find the minimum compliance, curling, and stress stiffening. Since the design area for the suspension structure is separated from the actuation area, changes in the topology of beams do not affect the force. So the derivatives of the objective function can be used efficiently to converge to the optimum solution. Additionally, the TO problem in their work is a kind of maximizing stiffness and is restricted by the volume fraction. So the optimization problem converges by reaching to maximum stiffness structure in a specific volume, similar to the convex TO problems in the literature [73]. Their approach is limited to convex optimization problems and cannot be used to maximize sensitivity which is proportional to minimizing the stiffness with other constraints. Teves and Silva [74] used TO in the design of a bulk micro-machined accelerometer. They considered maximizing/ minimizing strain energy, maximizing the mean value of the first six natural frequencies, and maximizing the volume fraction in different TO problems. Their design objective was mostly to increase the stiffness of the structure to increase the bandwidth. The proof mass and sensing area were considered constant in their design without getting affected by the mass or area of the suspension structure. With this assumption, they used derivatives of objective functions as sensitivity in a gradient-based TO algorithm. In the case of minimizing strain energy and maximizing mean natural frequency, the volume fraction constraint determines the optimized point since adding mass to the design domain improves these objective functions. But if the objective function is to maximize strain energy (minimize stiffness), the volume fraction constraint is an inactive constraint. The strain energy increases by decreasing the mass in the design domain (density of suspension structure). They used a minimum value for the mean natural frequency as an active constraint to get converge in the optimization process. The optimum design reported by this group is highly dependent on the initial design according to the applied TO method. Since elements with intermediate density were considered in the solution

with intermediate mechanical properties, their optimum solution converges to low density in simple suspension beams. Furthermore, the effect of changing mass (variable loading) and the area of sensing electrodes are not considered in their model. Wang et al. [75] designed a MEMS accelerometer using a semi-automated genetic algorithm (GA). They considered free-form geometries and used GA to improve the sensitivity and bandwidth of the accelerometer. Usage of free-form geometries resulted in 141% of improving sensitivity and 100% of improving bandwidth compared to conventional orthogonal designs. The assumption of their work was constant sensing area for both capacitance and inertial force. So the design just includes minimization of beam stiffness while the sensitivity is also dependent on the inertial proof mass and surface area of the electrodes. In addition, the optimization is limited to free-form geometries of the beam considered for the suspension system. But other combinations of suspension systems with any shape can be used to improve performance. To sum up, most of the available methods in the literature used shape optimization to find the best combination of sizes for a predefined design. In the cases where TO is used to design a MEMS accelerometer, there are some assumptions to simplify the optimization problem and converge to a feasible design. The assumption of constant proof mass puts a constant inertial force on the movable electrode and consequently, useful sensitivity information to be used in gradient-based TO algorithms. A constant proof mass also ignores the effect of changing the surface area of the capacitor. In the accelerometers made with bulk-micromachining, the proof mass is big enough in relation to the mass of tiny suspension structures. So, the assumption of constant force is reasonable in those designs. But in the accelerometers to be fabricated by surface micromachining, the thickness of proof mass and suspension structure are equal and changes in any region have a considerable effect on the performance. In addition, the surface area of the suspension structure can be used as electrodes and added as a design parameter in the calculation of capacitance. And most importantly, available TO problems deal with simple objective functions such as minimization of compliance and maximization of natural frequencies, while volume fraction is a constraint. But in this case, the objective is to increase sensitivity which is proportional to maximizing compliance in a limited range of motion. The volume fraction is not a design constraint in this case. The constraints come from the limitations in performance and feasibility for manufacturing. The main contribution of this study is developing a TO algorithm for considering variable loading in proof mass, the effect of changing surface area to the capacitance, and applying manufacturing constraints. The objective of maximizing sensitivity, and mentioned conditions make the TO problem non-convex and not possible to be solved by gradient-based methods. So, a non-gradient-based TO algorithm was developed and applied to this problem. Since for this objective function any singular solution improves the objective, manufacturing constraints are applied during the optimization process to just deal with the solutions which are manufacturable. The next section introduces TO and optimization techniques and then demonstrates their

applicability to different problems with limitations.

2.2 Topology Optimization

Topology Optimization (TO) is a general word for any algorithm that maximizes the performance of a system by determining the distribution of the material in a design domain. The design domain is the physical domain that has the possibility of adding or removing material to it. Unlike size or shape optimization, TO can converge to any shape and size inside the domain. A TO problem has at least one objective which is the target of optimization. An objective function can be any performance parameter of the system depending on its application. In the TO problems where the objective function changes continuously with the design variables, gradient-based optimization algorithms can lead the solution to the optimum solution in a few steps. Otherwise, non-gradient-based (gradient-free) algorithms can be used to estimate the optimum solution. Besides the objective of TO, there are constraints from physical limitations or some performance criteria. The optimization algorithm is responsible for gradually changing the topology of the design inside the domain to converge to the optimized solution. The selection of a proper TO algorithm and the optimizer is essential to reach the optimum design. The proper optimizer and TO method depend on the objectives and constraints. This section reviews the mathematical optimization methods first. Then, the gradient-based and non-gradient-based TO methods are discussed. The TO with intermediate density or binary elements is investigated and compared. Finally, TO problems with uncertainties are discussed and the variable loading TO problem is reviewed as a TO problem with uncertainty and methods to deal with it.

2.2.1 Optimization Algorithms

An optimization algorithm is a mathematical method to select the best available solution in a function. For an optimization problem, x_0 is minimum if for any x in the n -dimensional domain and f as the objective function, Eq. (2.7) is satisfied.

$$\forall x \in \mathbb{R}^n \rightarrow f(x_0) \leq f(x) \quad (2.7)$$

For the maximum solution, the same condition should be satisfied from Eq. (2.7) with the opposite direction of the inequality. It should be noted that x belongs to the domain of the function and in the case of constraints, the available solution must satisfy the imposed constraint. An optimization problem can have one or more optimum solutions. An optimum point is a global optimum if it is a valid solution that satisfies the conditions of Eq. (2.7) in the whole domain. In some cases, there are some valid solutions that satisfy the condition of Eq. (2.7) just for a neighborhood of x^* with a distance of δ but

not for the whole domain. Such points are called local optimums and can be presented in mathematical form as Eq. (2.8) for a local minimum and similarly for a local maximum.

$$\forall x \in \|x - x^*\| \leq \delta \mapsto f(x^*) \leq f(x) \quad (2.8)$$

Finding the optimum solution for an optimization problem is a procedure that uses different types of algorithms depending on the function and constraints. Optimization algorithms can be divided into two groups of deterministic or stochastic. Deterministic algorithms use specific rules to move an available solution to a new one. They have been used for many optimization problems, especially where the objective function is differentiable. Stochastic algorithms, on the other hand, use probabilistic rules to generate new solutions and converge to an optimum solution with an error. Where the objective function of the optimization problem is differentiable, derivatives can be calculated at any point in the domain. The derivative of a function shows the rate of change in the function by changing corresponding variables. For a function with only one variable, the derivative is the slope of the line when plotting the objective versus the input variable. In functions with more than one variable (multi-variable), the objective can change by changing any single variable while keeping the rest of the variables constant. For a multi-variable function, a partial derivative is the derivative of the function with respect to one variable assuming the rest of them are constant. A vector of all partial derivatives with respect to each variable is called a gradient and can be used for different purposes in studying a function. Assuming a differentiable multi-variable objective function is a scalar-valued function showed by $f : \mathbb{R}^n \mapsto \mathbb{R}$, the gradient vector at an arbitrary point of p in n -dimensional space can be calculated by Eq. (2.9).

$$\nabla f(p) = \begin{bmatrix} \frac{\partial f}{\partial x_1}(p) \\ \vdots \\ \frac{\partial f}{\partial x_n}(p) \end{bmatrix} \quad (2.9)$$

where $\frac{\partial f}{\partial x_i}$ is partial derivative with respect to x_i -th variable and nabla symbol (∇) is the vector differential operator. In a more general form if the objective function is a vector-valued function as $f : \mathbb{R}^n \mapsto \mathbb{R}^m$, derivatives can be shown by Jacobian matrix in Eq. (2.10).

$$J = \begin{bmatrix} \frac{\partial f}{\partial x_1} & \cdots & \frac{\partial f}{\partial x_n} \end{bmatrix} = \begin{bmatrix} \nabla^T f_1 \\ \vdots \\ \nabla^T f_m \end{bmatrix} = \begin{bmatrix} \frac{\partial f_1}{\partial x_1} & \cdots & \frac{\partial f_1}{\partial x_n} \\ \vdots & \ddots & \vdots \\ \frac{\partial f_m}{\partial x_1} & \cdots & \frac{\partial f_m}{\partial x_n} \end{bmatrix} \quad (2.10)$$

Continuity is an essential condition for a function to be differentiable but not enough. Additionally, even if a function is differentiable, it does not guarantee that the derivations (gradient in multi-variable) are useful to reach the optimum point. But usually, the gradient of objection function makes the optimization easier and lots of optimization algorithms are developed for optimization using a gradient, called gradient-based optimization and

mentioned in this study with the same name. In some cases, second-order derivatives of a function can give extra information for the investigation of critical points and also for large-scale optimization methods such as Newton-type methods [76]. For a multi-variable scalar-valued function, second-order partial derivatives (if all exist) are presented with a square matrix called the Hessian matrix. Assuming $f : \mathbb{R}^n \mapsto \mathbb{R}$, the Hessian matrix is a $n \times n$ matrix as Eq. (2.11).

$$H(f(x)) = H_f = \begin{bmatrix} \frac{\partial^2 f}{\partial x_1^2} & \frac{\partial^2 f}{\partial x_1 \partial x_2} & \cdots & \frac{\partial^2 f}{\partial x_1 \partial x_n} \\ \vdots & \vdots & \ddots & \vdots \\ \frac{\partial^2 f}{\partial x_n \partial x_1} & \frac{\partial^2 f}{\partial x_n \partial x_2} & \cdots & \frac{\partial^2 f}{\partial x_n^2} \end{bmatrix} \quad (2.11)$$

Comparison of Eq. (2.11) and Eq. (2.10) shows that the Hessian matrix is Jacobian of the gradient vector and can be obtained from Eq. (2.12).

$$H(f(x)) = J(\nabla f(x)) \quad (2.12)$$

According to Schwarz's theorem, if the second partial derivatives are all continuous, the Hessian matrix is symmetric. For a vector field function as $f : \mathbb{R}^n \mapsto \mathbb{R}^m$, the second partial derivatives are a third-order tensor or an array of m Hessian matrix as shown in Eq. (2.13).

$$H(f) = H(f_1(x), f_2(x), \dots, f_m(x)) = (H(f_1), H(f_2), \dots, H(f_m)) \quad (2.13)$$

The Hessian matrix of a function can be used for the second partial derivative test to determine the situation of a critical point. A critical point in the domain of a function is a point where the gradient vector is zero. If the Hessian is positive definite (negative-definite) at a critical point, then the point is an isolated local minimum (maximum). If the Hessian matrix has positive and negative eigenvalues at a critical point, then that is a saddle point. If the Hessian matrix is positive-semi-definite and negative-semi-definite at a critical point but not definite, the test is inconclusive (the critical point can be a local extremum or saddle point). Hessian matrix can be used to determine the convexity of a function. A scalar-valued function $f : \mathbb{R}^n \mapsto \mathbb{R}$ with available first and second derivatives is convex if and only if its Hessian matrix is positive-semi-definite in the whole domain. In optimization, if the objective function is convex, every local minimum is a global minimum (the same for maximum). For a strictly convex objective function, the problem has at most one optimal point. A convex optimization problem can be solved quickly and reliably for any size of variables and number of constraints. A variety of optimization methods have been developed for convex problems such as interior-point methods and can reach a solution with a specified accuracy [77]. Recognition of convexity is an important but not easy task in the optimization of a function, especially when dealing with a multi-variable problem. For any convex or non-convex problem, an optimization algorithm is required to find the optimum point. Algorithms that use gradient information of the objective

function to find the optimum are more popular due to efficient convergence. Bracketing algorithms, local descent algorithms, first-order algorithms, and second-order algorithms are some groups of gradient-based optimization methods. Bracketing algorithms such as Fibonacci search, Golden section search, and Bisection method are suitable for single variable optimization problems. They can find the optimum point in a known range efficiently, but they are limited to one variable as input for the optimization problem. Local descent algorithms are gradient-based optimization algorithms such as line search that choose a direction to move and perform a bracketing search in that direction. A local descent algorithm is applicable to multi-variable scalar-valued problems with a single global optimum. This method has high computational costs to reach the optimum solution. First-order or gradient descent is another gradient-based optimization algorithm that determines the direction of reaching the optimum solution using gradients of the objective function. These algorithms control the search on the line of movement with a step size instead of a full search to reduce computational costs. Adjustment of step size is necessary to make sure it is large enough to escape local optima and small enough to converge with enough accuracy. Second-order algorithms use the gradient and Hessian of a function to move toward the optimum solution. Newton and Secant's methods are two well-recognized second-order algorithms for single-variable problems. In multi-variable objective functions, Quasi-Newton methods can be used as a second-order algorithm. Quasi-Newton methods such as Davidson-Fletcher-Powell and Broyden-Fletcher-Goldfarb-Shanno are developed for a variety of optimization problems. Usually, gradient-based optimization algorithms converge to the optimum solution with reasonable computational cost and good accuracy. Intelligent manufacturing process planning is used in the literature to improve the accuracy and quality of the final products [78, 79]. The main problem with using gradient-based methods is having a differentiable objective function, which only works for well-formed mathematically defined functions. In a huge number of real optimization problems, the function and mathematical model are not defined and consequently, computation of gradients is impossible. Various models have been developed to simulate multi-physics problems in engineering with different models [80, 81]. In some cases, the mathematical model of the objective function is complex and the computational costs are not reasonable to calculate gradients. For example, the dynamic model for the movement of a submarine is complex and is dependent on fluid-structure interactions. For the control of such systems, neural networks are usually utilized to model the dynamic behaviors of the system. For optimization of movements and path planning of this system, the gradient cannot be calculated or it needs very complex modeling and simulations [82]. So, the gradient-based optimization algorithms are not applicable to the submarine modeled with a neural network. Even if an objective function is differentiable and the gradients can be calculated easily, they are not necessarily useful for optimization. For multi-modal (with multiple global optima), noisy (stochastic evaluation), and discontinuous objective

functions, gradients in the whole domain or in some regions are not a good guide for optimization. In such optimization problems, non-gradient-based algorithms are applicable without a need for first or second-order derivatives. Non-gradient-based algorithms such as Direct algorithms, Stochastic algorithms, and population algorithms do not need much information about the behavior of an objective function and work like a black box. Direct optimization algorithms (pattern search) are deterministic procedures to converge to a unique global optimum. Direct algorithms compare the relative difference of scores assigned to the domain to approximate gradient information. Then uses the directly estimated gradients to define the moving direction to the optimum solution. Cyclic coordinate search, Powell's method, Hooke-Jeeves method, and Nelder-Mead simplex searches are some popular direct search algorithms. Since direct search algorithms need a direction of movement to reach the optimum solution, they work efficiently with convex and uni-modal optimization problems. For non-convex or multi-modal problems, direct search algorithms do not guarantee to converge to the optimum solution. The direct search algorithms find an optimum solution for a non-convex problem that can be a local optimum depending on the initial solution. Stochastic optimization algorithms are another type of non-gradient-based optimization method that randomly searches the domain to find the optimum point. Due to random search, stochastic algorithms generate and evaluate a huge number of solutions and can escape the local optimum and converge to the global optimum. Simulated Annealing, Evolution strategy, and Cross-Entropy method are some examples of Stochastic optimization algorithms [83]. These algorithms are suitable for almost any type of optimization problem regardless of convexity or local optimums. The main issue that limits the application of this method is high computational costs due to the evaluation of many samples in the domain [84]. Population Algorithms are non-gradient-based optimization methods that work with stochastic strategy but maintain a population of candidate solutions to generate the next solutions and converge to the optimum. Population algorithms such as Genetic Algorithm, Differential Evolution, and Particle Swarm can give more robustness for converging to the optimum solution. These algorithms have better performance when starting from a population close to the optimum solution. Depending on the type of objective function and constraints, one or some of the mentioned algorithms can efficiently converge to the optimum solution. According to the physic of the optimization problem and having more flexibility to the topology optimization, stochastic algorithms with simulated annealing are used successfully as the optimizer in this research. This method has been used in many research works successfully as an efficient evolutionary method [83].

2.2.2 Constrained optimization

Constraint optimization is a process of finding the optimum for a function by considering some limits. The limits come from the physical or numerical conditions of the optimization

problem and can be hard or soft constraints. Hard constraints are the condition that must be satisfied and violating them makes the solution unacceptable. Soft constraints, on the other hand, are not essential but should be penalized in the solution. Hard constraints can be applied to an optimization problem as equality constraints or inequality constraints. For a general optimization problem with an objective function of $f(x)$ and $x \in \mathbb{R}^n$, l equality constraints that should be satisfied can be shown as Eq. (2.14).

$$g_i(x) = 0 \quad \text{for } i = 1, \dots, l \quad (2.14)$$

Similarly, an inequality constraint imposes a limit of inequality to the optimization problem. Inequality constraints for an optimization problem can be shown as Eq. (2.15).

$$h_j(x) \leq 0 \quad \text{for } j = 1, \dots, k \quad (2.15)$$

There are several methods to solve a constrained optimization problem. A constraint problem can be converted to an unconstrained optimization problem using penalization. The solution for the new unconstrained optimization problem with the penalization of constraints is the same or close to the original problem with constraints. In this method, the Maratos effect is the main disadvantage. Due to the Maratos effect, search steps to find the solution in the new unconstrained optimization can violate hard constraints and cannot converge efficiently to the optimum solution. If all of the constraints are equality constraints, Lagrange multipliers (λ_i) can be used to convert the unconstrained problem to a new optimization problem without constraint. In a mathematical form, the new optimization problem for the objective function of $f(x)$ subjected to equality constraints of Eq. (2.14) can be stated as Eq. (2.16) and called Lagrangian function.

$$\mathcal{L}(x_1, \dots, x_n, \lambda_1, \dots, \lambda_l) = f(x) + \sum_{i=1}^l \lambda_i g_i(x) \quad (2.16)$$

Lagrange theory states that stationary points for Eq. (2.16) are the points that all partial derivatives with respect to x and λ are zero. In other words, at optimum points of the objective function subjected to the equality constraints, the gradient of the objective function is equal to the linear combination of the constraint's gradient as shown in Eq. (2.17).

$$\nabla f(x) = \sum_{i=1}^l \lambda_i \nabla g_i(x) \quad (2.17)$$

It means any direction perpendicular to the gradient of the objective function is perpendicular to gradient constraints. This method has been used for many engineering problems without a need for explicit parameterization of the constraints. This method is generalized for inequality constraints by Karush–Kuhn–Tucker (KKT) conditions. The Lagrangian function for an optimization function of $f(x)$, equality constraints of Eq. (2.14), and inequality constraints of Eq. (2.15) can be rewritten by Eq. (2.18) and with new

multipliers called KKT multipliers.

$$\mathcal{L}(x_1, \dots, x_n, \lambda_1, \dots, \lambda_l) = f(x) + \sum_{i=1}^l \lambda_i g_i(x) + \sum_{j=1}^k \mu_j h_j(x) \quad (2.18)$$

In most of the real cases, the analytical solution is not available and KKT system of equations can be only solved numerically. This method is applicable if the objective function and constraints are all differentiable and convex, or at least have sub-derivatives (derivatives of convex functions that are not differentiable). For x^* as a local optimum of Lagrangian in Eq. (2.18), regularity conditions of stationary from Eq. (2.19) or Eq. (2.20), primal feasibility from Eq. (2.21), dual feasibility from Eq. (2.22), and complementary slackness from Eq. (2.23) should be satisfied as necessary conditions.

$$\partial f(x^*) + \sum_{i=1}^l \lambda_i \partial g_i(x^*) + \sum_{j=1}^k \mu_j \partial h_j(x^*) \ni \mathbf{0} \quad \text{for minimizing } f(x) \quad (2.19)$$

$$-\partial f(x^*) + \sum_{i=1}^l \lambda_i \partial g_i(x^*) + \sum_{j=1}^k \mu_j \partial h_j(x^*) \ni \mathbf{0} \quad \text{for maximizing } f(x) \quad (2.20)$$

$$g_i(x^*) = 0, \text{ for } i = 1, \dots, l \quad \text{and} \quad h_j(x^*) \leq 0, \text{ for } j = 1, \dots, k \quad (2.21)$$

$$\mu_j \geq 0, \text{ for } j = 1, \dots, k \quad (2.22)$$

$$\sum_{j=1}^k \mu_j h_j(x^*) = 0 \quad (2.23)$$

Necessary KKT conditions can be interpreted as moving a particle in the x space and balanced by constraint forces. In this interpretation, f is a potential field to be minimized (or maximized) and generates a force field of ∂f . The particle can move on the surface of $g - i$ as the equality constraint and inside of $h_j \leq 0$ as inequality constraints. The mentioned necessary conditions are sufficient in some special cases. For maximization of a concave objective function with convex and continuously differentiable inequality constraints and affine equality constraints, or for minimization of a convex objective function the necessary conditions are sufficient to find optimum points subjected to all constraints. For a non-linear but smooth problem, the second order condition of Eq. (2.24) should be satisfied in addition to the necessary conditions as a sufficient KKT condition.

$$s^T \nabla_{xx}^2 \mathcal{L}(x^*, \lambda^*, \mu^*) s \geq 0 \quad (2.24)$$

where s is a non-zero vector satisfying Eq. (2.25) for all active inequality constraints.

$$\left[\nabla_x g_i(x^*), \nabla_x h_j(x^*) \right]^T s = 0 \quad (2.25)$$

The KKT condition can be used to find the optimum solution in addition to the active constraints, but the objective function should be well-defined and gradients can be calculated or at least estimated in a convex domain. The KKT multipliers show the importance of any constraint. For inequality constraints, a zero multiplier demonstrates inactive corresponding constraints. In an optimization problem where the objective function or a constraint is not known or the derivatives are hard to get, other methods can be applied regarding the optimization problem. The penalty methods are usually used in non-gradient-based optimization problems to converge to the optimum solution by penalizing violating constraints. This method still deals with a solution in the infeasible area and does not necessarily converge to the optimum solution. But in non-gradient-based optimization problems, it can be useful to imply the effect of constraints while the other methods are inapplicable [85]. Using the Lagrangian method or KKT multipliers to add constraints to the objective function and penalize them is not applicable to the optimization problem of this work. Constraints from manufacturability cannot be invaded to have a feasible design. The objective of maximizing sensitivity is conflicting with constraints on manufacturability in the TO problem. While these constraints are invaded, the solution is not feasible and such solutions cannot be compared. So the optimization algorithm should consider manufacturing constraints as a hard limit during the optimization process [86, 87]. A comparison of the optimization algorithms showed that the SA algorithm can efficiently add this criterion to the topology optimization problem and deal with hard limits during the optimization process. The next section introduces the SA as an optimization algorithm with the mechanism of performance.

2.2.3 Simulated Annealing (SA) optimization algorithm

The concept of performance in the SA algorithm is inspired by the annealing process in metallurgy. The annealing process in metals starts with heating the material to a high temperature and then cooling it down slowly to a low temperature. From a microscopic perspective, atoms get a high level of energy with a high possibility of movements and then reduce their energy slowly till reaching a stable situation with a lower level of energy. The SA optimization method was first developed by Kirkpatrick et al. [88] to find an approximate solution for complex problems such as non-deterministic polynomial time complete problems which do not have an exact solution. Simulated Annealing (SA) is introduced as a type of stochastic global optimization algorithm with heuristic search in the domain. Heuristic search strategies can be classified as iterative improvement and divide-and-conquer methods. In the divide-and-conquer method, the optimization problem would be divided into sub-problems of manageable size to be solved. Then, solutions of each sub-problem are patched together to find (or approximately converge) the optimum solution. The divide-and-conquer method is applicable in optimization problems where the sub-problems can be selected with naturally disjoint properties. In the iterative

improvement method, the process starts from an initial solution and a standard operation rearranges the current solution to discover an improvement in the objective function. Then, the current solution would be replaced by a new improved solution. This process continues until reaching a solution that cannot be improved anymore. The iterative improvement method is a hill-climbing strategy that can get stuck in a local optimum. To use iterative improvement for finding a global optimum, the process should be repeated several times with different initial solutions. SA algorithm benefits from this strategy with statistical sampling with a probability distribution similar to the Metropolis-Hastings algorithm. The statistical mechanic is a method to observe the properties of a sampling material (containing a large number of atoms) by its most probable behavior in thermal equilibrium. Behaviors of atoms are characterized by small fluctuations about the average behavior of the system [88]. The probability distribution known as Boltzmann distribution defines that the probability of being in a certain state of i is proportional to its energy and temperature as shown by Eq. (2.26).

$$p_i \propto e^{\frac{-\epsilon_i}{K_B T}} \quad (2.26)$$

where ϵ_i is energy at state i , K_B is Boltzmann constant, and T is thermodynamic temperature. It can be seen from Eq. (2.26) that at low temperatures, the Boltzmann distribution collapses to the lowest energy state (ground state). But being in a low temperature is not sufficient to reach the ground state in the actual annealing process. In annealing, it is necessary to reduce the temperature slowly and give enough time to atoms in any temperature state (especially near the freezing point) in order to get single crystals (minimum energy state). Otherwise, the system goes out of equilibrium and defects appear in the crystal structure (meta-stable). Kirkpatrick et al. [88] used this process in the heuristic optimization process. They showed that iterative improvement for a heuristic search in optimization can be treated as the energy level of the annealing process. But only accepting improved solutions (as is in the iterative improvement method) is similar to fast cooling down in annealing and results in a meta-stable solution. To reach the equilibrium state at each temperature, enough population of solutions should be generated and evaluated. Metropolis algorithm adds a random-based probability of accepting not improving solutions to not stuck in local optimums. In this algorithm for an objective function of $f(x)$ to be minimized, the newly generated solution gets acceptance in two situations; First, if the new solution is less than the current solution (improvement in the objective). This is equal to decreasing the energy state of the system in SA which is defined in Eq. (2.27).

$$\Delta E = f(x_{new}) - f(x_{current}) \quad (2.27)$$

The second situation of accepting a new solution is when the energy state in Eq. (2.27) is increasing but the probability factor is more than a random number. The probability factor in SA is defined as the change in Boltzmann energy level in Eq. (2.28).

$$P(\Delta E) = e^{\frac{-\Delta E}{T}} \quad (2.28)$$

If the probability function in Eq. (2.28) is more than a random number in the interval $(0, 1)$, the solution gets acceptance and the new solution in SA becomes the current solution. This Metropolis criterion rescues the algorithm from local minima. It can be seen from Eq. (2.28) that this probability factor is getting smaller by reducing temperature and increasing the energy level difference. It means that in high temperatures, the algorithm accepts a variety of different solutions with high differences in the energy level (exploration). In low temperatures, it has a low chance of accepting non-improving solutions with high differences in energy levels (refinement). So, the SA algorithm for a general unconstrained optimization problem to minimize an objective works as shown in the flow chart of Fig. 2.5. As shown in Fig. 2.5, the optimization starts from an initial solution inside the domain and from a maximum temperature. The maximum temperature is a parameter that depends on the optimization problem and range of variables. It can be selected by experience and analyzing some trial runs. As a rule of thumb, the maximum temperature (T_{max}) at the beginning should be high enough to accept 80% of new solutions by the Metropolitan criteria. Since the maximum temperature depends on the scaling of the objective function, it can be estimated using acceptance probability (P) and average objective function increase (ΔE) in an initial search and putting in Eq. (2.29).

$$T_{max} = \frac{-\Delta E}{P} \quad (2.29)$$

In each temperature, some new solutions would be generated by the Monte Carlo method and evaluated by SA. The new solution is a local transformation of the current solution and must be able to sample the whole domain efficiently. If the new solution is better than the previous one, it gets acceptance. Also, if the new solution is not improving the objective function, the probability factor from Eq. (2.28) would be calculated for it and compared with a random number. If the probability factor is higher than a random number in $(0, 1)$, the new solution gets acceptance. The number of new required solutions to have enough evaluation depends on the domain of the optimization problem. The number of generated new solutions should be high enough to make enough exploration happen to converge to the global optimum [89]. After the generation and evaluation of sufficient candidates, the temperature reduces. The annealing schedule determines the next temperature and should be tuned based on the optimization problem. In most of the cases in the literature, the temperature reduction is linear with a cooling rate of α . A cooling rate is usually a number in the range of $0.8 - 0.99$. Using a linear cooling rate, the temperature in the $k - th$ iteration (T) can be calculated using Eq. (2.30).

$$T = T_{max}\alpha^k \quad (2.30)$$

Other approaches are also used to estimate the temperature in the literature. For example, the new temperature can be calculated by exponential cooling in Eq. (2.31).

$$T = T_{max}(1 - \frac{k}{k_{max}})^\beta \quad (2.31)$$

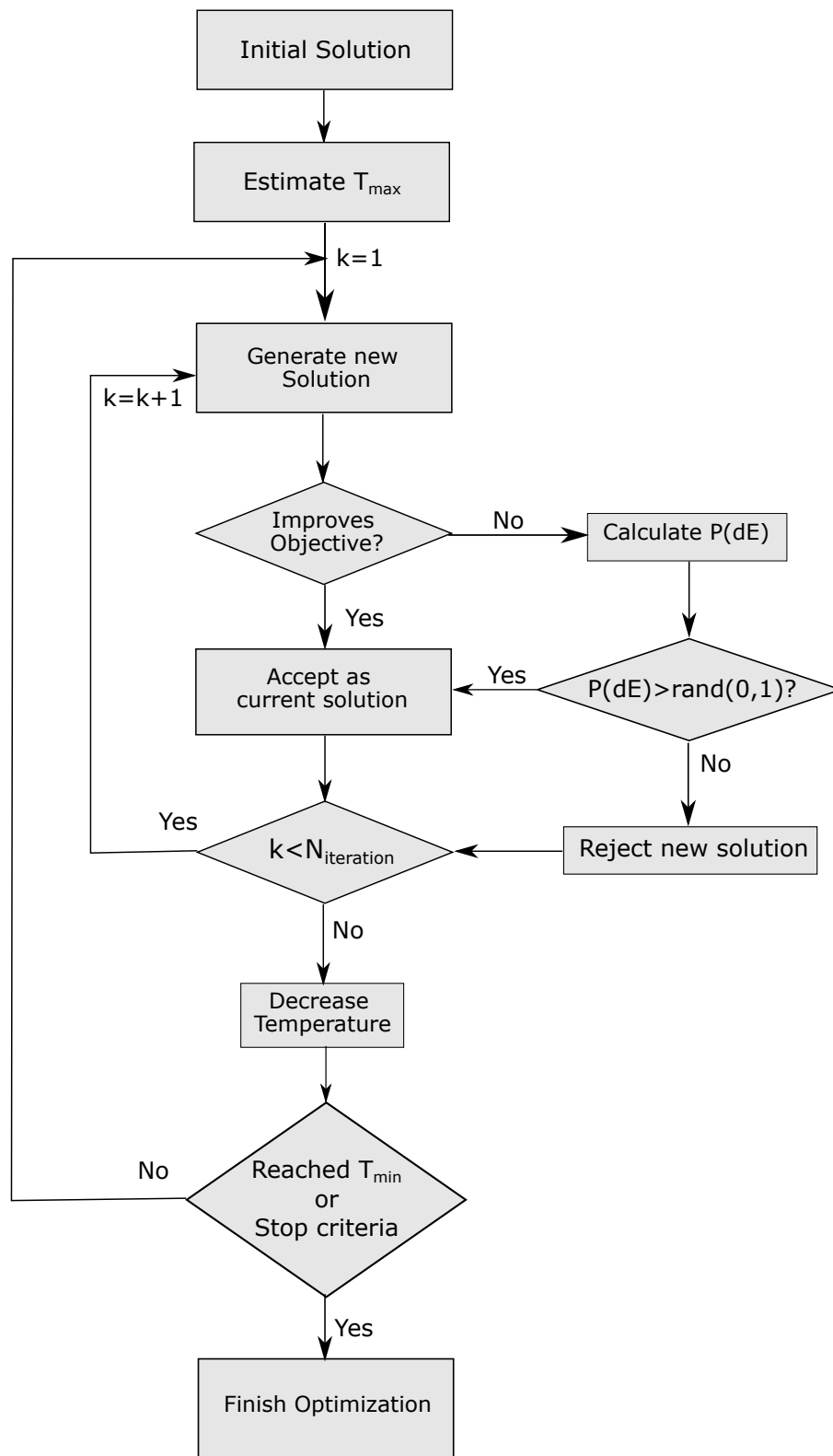


Figure 2.5 – Flow chart of unconstrained optimization with SA algorithm

where the exponent β is a number in the range of $1 - 4$ and can be selected based on the optimization problem and experience [90]. To make the annealing schedule more efficient, more advanced adaptive methods are developed based on laws of thermodynamics to adopt temperature by energy difference of two states [91]. The process of generation of new solutions and evaluations repeats $N_{iteration}$ times in any temperature and then temperature reduces till reaching the freezing state. The freezing state or reaching minimum temperature (T_{min} is the state to terminate the optimization. This is where no more improvement happens for the new solutions and the possibility of the acceptance ratio is smaller than a value (depending on the size of the problem). This temperature can be estimated by analyzing the number of accepted and rejected solutions in a trial run. For an optimization problem with constraints, usually SA algorithm performs the optimization with the same approach as an unconstrained problem with adding rejection criteria where any constraint is violated. This strategy is applicable for most of the constrained optimization problems except in problems with equality constraints or where the domain is disjoint by constraints. In the first case, violation of an equality constraint is very probable since new solutions are not necessarily moving on the constraints. In the second case, constraints are separating the feasible space, and moving between feasible solutions is hard or impossible due to the low probability of passing through infeasible space. In such cases, violated constraints can be added to the objective function as a penalty function similar to Eq. (2.18). To change the coefficient of effectiveness of penalized constraints of Eq. (2.18) with the SA algorithm, weighting coefficients are used for each constraint to get an augmented objective function $f^*(x)$ as Eq. (2.32).

$$f^*(x) = f(x) + \frac{1}{T} \left[\sum_{i=1}^l w_{1,i} g_i(x) + \sum_{j=1}^k w_{2,j} h_j(x) \right] \quad (2.32)$$

where w is the weighting coefficient and can be selected based on the importance of each constraint and its range. The inverse temperature increases the effect of each constraint near the optimum solution. The SA algorithm is selected as the optimization method in TO for this study. The ability to reach the global optima, no need for gradient information and the ability to deal with various constraints are advantages of SA that made it a proper candidate for this problem. In addition, some modifications to this algorithm in TO made it more efficient in convergence to the optimum solution and with low computational costs.

2.2.4 Gradient and non-gradient based Topology Optimization

A general topology Optimization (TO) problem can be defined as the distribution of variable density $\rho(x)$ in the design domain Ω to minimize an objective function F showed by Eq. (2.33).

$$\min: F = F(u(\rho), \rho) = \int_{\Omega} f(u(\rho), \rho) dv \quad (2.33)$$

where u is a static field. The density variable can be zero (for void elements) or one (for solid elements). The objective function can be calculated as the integral of a local function $f(u(\rho), \rho)$ in the domain. The TO problem in Eq. (2.33) can be subjected to constraints $G_j \leq 0$ as a function of material distribution in Eq. (2.34).

$$G_j(u(\rho), \rho) \leq 0 \quad j = 1, \dots, M \quad (2.34)$$

There are several approaches to finding the optimized topology for the problem in Eq. (2.33). In some cases, TO can be done using shape optimization methods with the possibility of adding or removing holes in the initial design. The other method that is commonly used in TO is the density approach that deals with local density variables instead of boundaries [92]. In the density approach, the domain of TO is discretized into N fixed Eulerian meshes. The density distribution is defined by N elements or nodal variables. So, the TO problem of Eq. (2.33) can be written as a summation of local objectives as Eq. (2.35).

$$\min: F(u(\rho), \rho) = \sum_{i=1}^N \int_{\Omega_i} f(u(\rho_i), \rho_i) dv \quad (2.35)$$

Therefore, objective function and constraints can be stated by combining the objective of optimization and constraints of Eq. (2.34). In many TO problems, the number of holes to be generated in the domain (new void elements in the discretized domain) can be increased by increasing the number of elements in the optimized design. It usually happens because of numerical instabilities. This leads to a design with checkerboards. Several approaches were applied to prevent rapid oscillations of density changes during optimization. Gradient-based topology optimization (GTO) approaches start from an initial density distribution and calculate the value of objective function and gradients for each element. GTO algorithms use a gradient-based optimizer to generate new solutions and move toward the optimum solution. To use a GTO method, the objective function and constraints should be well-defined mathematically with the availability of gradients for all elements in the design domain. Having a large number of variables in a TO problem makes it hard to find a solution where the elements can be only 0 or 1. An efficient approach that has been used in many TO algorithms considers the density of each element as a continuous design variable in $[0,1]$. For the continuous density approach, the same objective function of Eq. (2.35) can be used with a difference that the density of each element is a continuous number between 0 and 1. Mechanical properties of a material in each element can be calculated by interpolation of density as Eq. (2.36).

$$f(u(\rho), \rho) = D(\rho)f_0(u) \quad (2.36)$$

where $D(\rho)$ and $f_0(u)$ are density interpolation function and a function of the field for solid material, respectively. One of the most popular density methods is the power-law approach

or simplified isotropic material with penalization (SIMP). The SIMP is a simplified version of the homogenization approach and uses the power law to find the relation of density and material properties by Eq. (2.37).

$$E(\rho_i) = D(\rho_i)E_0 = \rho_i^p E_0 \rightarrow D(\rho_i) = \rho_i^p \quad (2.37)$$

where $E(\rho_i^p)$ is Young's modulus of i -th element with a density of ρ and E_0 is Young's modulus of solid material. For other mechanical properties, the same approach can be used with the power law in Eq. (2.37). In this approach, p is the penalization factor to penalize intermediate density to converge to 0 or 1 densities in the optimized solution. This penalization improves the convergence to the optimum solution, especially where there is a constraint in limiting volume. Similar approaches are developed to alleviate the non-concavity of SIMP. The rational approximation of material properties (RAMP) is a method to ensure convergence of optimization to a 0 or 1 solution in such situations. The RAMP approach interpolates the mechanical properties of each element by Eq. (2.38).

$$E(\rho_i) = \frac{\rho_i}{1 + q(1 - \rho_i)} E_0 \rightarrow D(\rho_i) = \frac{\rho_i}{1 + q(1 - \rho_i)} \quad (2.38)$$

where q is the penalization factor in RAMP. The RAMP interpolation can be useful for better convergence where void elements exist with 0 density to avoid singularity in the calculation of derivatives. The density approach can provide smooth and differentiable problems from Eq. (2.35). These problems can be solved by gradient-based optimization algorithms such as optimality criteria (OC) or the method of moving asymptotes (MMA). Density approaches can modify discrete TO problems to differentiable ones with slow density changes in many TO problems. But there is still a considerable number of TO problems that cannot be solved with GTO algorithms. One example of such cases is TO problems with no mathematical model. Where the physical system does not have a model, the calculation of derivatives is impossible or hard (with numerical methods). In a TO problem, it is more challenging to model and find derivatives due to a large number of variables. Another example of a TO problem that cannot be solved by GTO methods is non-convex problems with several local optimums. Since GTO moves in the direction of derivatives, the solution can be stuck in a local optimum. Even if the objective function of TO problem is convex, constraints on the domain can prevent convergence to the global optimum design. In such cases, the final design obtained from TO is dependent on the initial solution. Where GTO algorithms cannot be used efficiently to find the optimum design, non-gradient-based topology optimization (NGTO) algorithms can be used as an alternative to converge to the optimum design but usually with high computational costs. NGTO methods benefit from random search instead of moving in a gradient direction. Genetic algorithms, artificial immune algorithms, ant colonies, particle swarms, simulated annealing, harmony search, and differential evolution schemes are well-recognized NGTO methods. They deal only with objective functions or some local gradient information.

Despite the high computational costs, NGTO algorithms have some advantages that make them a reasonable method for specific TO problems. The first outstanding advantage of NGTO is convergence to a global optimum. While the GTO algorithms search locally in the domain, NGTO benefits from global searches with the possibility to converge to the global optima. It should be noted that for convergence to a global optimum in an NGTO, the whole design domain should be sampled by random search. This can lead to a very high number of evaluations and computational costs in an NGTO with a large number of variables. For a design domain discretized by N elements, the number of combinations of binary elements can be calculated from Eq. (2.39).

$$N_c = 2^N \simeq 10^{0.3N} \quad (2.39)$$

In the case of applying a volume equality constraint, the number of combinations will be reduced to N_{cv} and calculated by Eq. (2.40).

$$N_{cv} = \frac{N!}{(N-M)!M!} \quad (2.40)$$

where M is the number of solid elements in a binary discrete domain. The volume equality constraint is not a common constraint in TO problems but can be applied by trying various volume constraints and comparing resultant optimum designs. But even with using volume equality constraint, the number of combinations from Eq. (2.40) increases drastically for a large number of elements, which is common in TO problems. Even using a coarse mesh might still need high computational costs [93]. This can be improved by using smart searches and high explorations at the beginning of TO, to reduce computational costs. This issue and a method to reduce computational costs are proposed in this work. The method is introduced based on an NGTO method by simulated annealing and smart search strategy to reduce computational costs while keeping the efficiency to converge to an optimum solution. The other advantage of NGTO is its ability to deal with discrete domains. This functionality is also available in some GTO methods like evolutionary structural optimization and topological derivative approaches [93]. In most cases, the optimized design with GTO uses density approaches. Then it uses a threshold to change elements with intermediate density to solid or void elements. This approach is beneficial in many cases, especially by improving the Finite Element Analysis (FEA) of the structure. But in a non-self-adjoint TO problem or where singular solutions are available, using discrete binary elements is essential to directly converge to an optimum design. Furthermore, this is not the only advantage of NGTO methods. In some TO problems, using NGTO is inevitable due to the model and gradients of the objective function and constraints. It is important to use fine enough meshes in a discrete binary design to model the physic of the design correctly by numerical calculations like FEA. Though, the selection of the proper mesh is highly important in NGTO. Another important advantage of NGTO algorithms is working without a need for gradient information. In a convex or self-adjoint TO problem

such as minimizing strain energy, the gradient of the objective function is easy to find. This problem has been used in many studies of TO as a benchmark problem. It is also an important problem in the design of stiff structures with the minimum usage of material. But in a variety of TO problems, the objective function or constraints can come with a non-mathematical model such as a neural network model. In such cases, an NGTO algorithm is the only or most efficient TO model. Since the method does not use gradient information to move gradually to the optimum point, the connectivity issue may appear in the optimum design. The connectivity issues and checkerboards are common in NGTO algorithms because of random search performance. In GTO algorithms sensitivity filtering is usually used to address this problem and obtain a smooth and connected structure. Sensitivity filters are used in GTO to avoid numerical instabilities. A sensitivity filter modifies the gradient of the objective function to avoid rapid changes in the density of elements. A sensitivity filter for the derivative of objective function $f(x)$ can be calculated by Eq. (2.41).

$$\widehat{\frac{\partial f(x)}{\partial x_i}} = \frac{1}{\max(\gamma, x_i) \sum_{j \in N_i} H_{ij}} \sum_{j \in N_i} H_{ij} x_j \frac{\partial f(x)}{\partial x_j} \quad (2.41)$$

where γ is a small number to avoid singularity and H_{ij} is a weighting function defined by linear distance between point i and point j inside a neighborhood of N_i . This filter removes the dependency of the solution on the mesh size. The radius of the sensitivity filter to define the neighborhood of N_i is an important parameter that can even change the final design. In NGTO, generating a new solution is based on a random search and gets no effect from the neighborhoods, even if there is any gradient. In NGTO, the solution can converge to a continuous and checkerboard-free design if the optimization problem is self-adjoint. But even in such methods, numerical instabilities in FEA and optimizer can prevent the solution to converge to optima and make checkerboards. Additionally, in an optimization problem where singular solutions show an improvement in the objective function, singular or checkerboard connections are solutions with numerical improvements in the objective function but not an actual physical solution. Such solutions should be avoided to make sure feasibility of the optimum solution. There are some approaches proposed and validated in this study to consider the checkerboard problem and connectivity in the final solution.

2.3 Variable loading TO

The classic problem of minimization compliance in structures with constant external loads was studied in the literature with different approaches [73]. This problem can be written in the form of strain energy and be solved by GTO as a convex optimization problem. In some cases such as large civil structures or inertial elements, self-weight loading of structures has an important effect on the loading condition. The classical approaches

for TO are unable to reach an optimized topology for problems subjected to self-weight loading. Even in a convex problem of finding minimum compliance, the density-dependent body forces change the convexity of the TO problem. In such cases, adding high-density elements to the structure increases the stiffness of the structure, but adds forces that can increase the displacements. So, increasing the density of a region can increase or decrease compliance and causes several problems in convergence to an optimum solution. In addition, it can lead to having several local optimums instead of a global one and not increasing or decreasing proportionally with the volume fractions. Bruyneel and Duysinx [94] improved the MMA algorithm with the evolution of gradients to address the self-weight non-monotonous behavior of structural compliance. Their method successfully stabilized the optimization process to reach a stationary solution in minimizing compliance problems. For a non-self-adjoint TO problem, the gradient of the objective function is not useful to be used with this method due to fluctuations in sensitivity. In such cases, the loading of self-weight is not easy to deal with. For the TO of an accelerometer to increase sensitivity, the objective is proportional to the increasing displacement of a structure due to the inertial forces (self-weight). Though, adding density to a region reduces the flexibility of the structure (not favorable) but increases inertial forces (favorable). In addition, the displacement should be limited to finite values and constrained maximum allowed stress. By adding more constraints regarding other performance criteria, the TO problem is a complex problem with several local optima. So, using available GTO methods with self-weight considerations is not sufficient to reach an optimum solution. Therefore, using an NGTO would be more efficient in this problem by updating the density-dependent body forces in each evaluation. The TO with SA can cover this problem with the ability to efficient convergence to an optimum solution with a cost of more computations.

2.4 Manufacturability in topology optimization

In most engineering problems, TO as a mathematical algorithm is able to find the most efficient solution. But the feasibility of the design for manufacturing is the necessary condition for the usefulness of the TO in a practical problem. Depending on the manufacturing method, the constraints can vary for manufacturability. In machining oriented TO the manufacturability constraints can be considered by length scale control and removing overlaps in geometric features [95, 96]. In TO of the structures to be manufactured by injection molding/casting, control of rib thickness and avoiding interior voids is necessary to prevent undercuts. In the case of TO for additive manufacturing, length scale control is enough to build the results with the resolution of the 3D printer [97, 98]. In micromachining and lithography, avoiding minimum length scale is an important constraint to keep elements far from being etched away [99]. Adding manufacturing constraints to the TO results in a final design that can be manufactured with the desired accuracy [100]. Since

the objective of this work is to design a MEMS sensor with TO, manufacturing limits for MEMS microfabrication should be applied. The manufacturing method of MEMS devices is called microfabrication. In the next section, two common microfabrication methods for MEMS capacitive accelerometers (bulk and surface micromachining) are introduced. Manufacturing limits in microfabrication were determined with some trial experiments. These manufacturing constraints should be considered in the final design from TO.

2.5 Microfabrication

Microfabrication is a general word for any manufacturing method on the scale of micro and nanometers. According to very small sizes, traditional machining processes for 3D manufacturing are not applicable. So, micromachining is mostly limited to non-complex shapes patterned in 2D for photolithography and etching. In a system where several structural layers are required, additional layers can be added by thin-film deposition and bonding techniques. For making a suspended structure such as MEMS sensors, a sacrificial layer can be etched away to make space between two structural layers or two layers can be bonded by spacers. A pattern on the wafer can be etched using a mask. For this goal, the substrate should be covered by a material resistant to the etchant, such as silicon dioxide (SiO_2). Then an organic polymer would be deposited on that as photoresist material. The required pattern would be transferred by exposing it to ultraviolet radiation with the required mask pattern. Then the exposed photoresist would be removed by developing in a solvent. Then the pattern would be transferred to the hard mask by etching it (usually with hydrochloric acid). After removing the rest of the photoresist, the sample would be etched by a proper etchant to etch away the area without the hard mask. The hard mask would be removed after etching the pattern on the wafer. The thickness of the wafer and its directional etching rates determine the resolution of the etched pattern. Silicon is an anisotropic material with different etching rates in each direction. So it can be used to make better resolutions in higher thicknesses. Other methods of etching such as Deep Reactive Ion Etching (DRIE) are also used to increase directional etching speed and obtain high aspect ratio patterns with better resolution [54]. In addition to anisotropic etching rates in silicon, it is mostly used as the structural material for MEMS devices because of its ability to be deposited in thin films, having good electrical and mechanical properties, and being abundant. Fabrication of a MEMS device can be done with bulk or surface micromachining. The distinguishing parameter for these methods is the thickness of the silicon wafer which results in different approaches to building a MEMS device. The bulk and surface micromachining methods are briefly discussed in the following.

2.5.1 Bulk Micromachining

Bulk micromachining is a manufacturing process of etching (wet or dry) from a bulk substrate. The wet etching includes removing the pattern by immersion of the silicon wafer with a hard mask in an etchant bath. Anisotropic etchants such as potassium hydroxide (KOH) can make deeper etches by different etch rates in each direction. The etching rate of silicon is high in a crystal direction perpendicular to the (1 1 0) plane and is small in a crystal direction perpendicular to the (1 0 0) and (1 1 1) planes. By putting the desired etching direction in the high etch rate direction, higher aspect ratios and better resolutions can be achieved. In dry etching, reactive gases or vapors are used to etch silicon in the desired direction. Dry etching such as DRIE can provide higher aspect ratios in bulk micromachining. In the case of MEMS accelerometer, bulk micromachining such as silicon on insulator (SOI) is used in many research works to have a thick proof mass. That increases the sensitivity and reduces the mechanical noises in a MEMS accelerometer. The mechanical noise is mostly from Brownian noise and increases with the reduction of mass or increase in resonance frequency. This noise should be considered an important parameter in the design with fabrication methods where the proof mass is lightweight. To assemble parallel electrodes in bulk micro-machined accelerometers, the suspended electrode should be bonded by a spacer to the fixed electrode. Also, etching a thick wafer makes some undercuts beneath the mask and makes the design more limited to simple shapes. Especial attention should be paid to the design of accelerometers for etching and wafer bonding. Due to the complexity of design and difficulty in manufacturing, bulk micro-machined accelerometers are not the best choice for commercial uses.

2.5.2 Surface Micromachining

Surface micromachining as a newer microfabrication method was initiated in the 1980s and is getting a very popular method due to its ability to combine with CMOS (Complementary metal–oxide–semiconductor). In surface micromachining, several thin film structural layers can be added to the substrate. Layers can be grown chemically (chemical vapor deposition, CVD) or deposited physically (physical vapor deposition, PVD) as a thin film. Each film can be used as the structural layer or sacrificial layer (to be removed later and make space between adjacent layers). A structure with several fixed or suspended layers can be achieved by a repeating of depositing layers and lithography. Since all layers can be made with deposition and etching, the surface micromachining can be used with the CMOS process and build the sensor on a single chip. Parameters of layer thickness and etching are also more controllable in this process. Using this process in the fabrication of MEMS sensors is a developing area in mechanical and electrical engineering. Improving the performance of such sensors through a proper design of mechanical structures can increase their usability in commercial applications. Some cases used surface micromachining to build

a MEMS accelerometer with improved performance and are used in this study to compare the results from TO. To make the results comparable, a commercially available surface micromachining process called PolyMUMPs is used as the manufacturing technique. All of the dimensions and parameters used in the design are from this process. The three-layer polysilicon surface micromachining process as a Multi-User MEMS Process (PolyMUMPs) is a commercial surface micromachining process provided by MEMSCAP. In this process, polysilicon is the structural material, deposited oxide (PSG) is the sacrificial layer, and silicon nitride is the electrical isolation between the polysilicon and the substrate [101]. The PolyMUMPs process starts with a heavily doping surface of a 150mm n-type (1 0 0) silicon wafer with phosphorus in a standard diffusion furnace using a phosphosilicate glass (PSG) sacrificial layer as the dopant source. Then the PSG would be removed and a silicon nitride layer would be deposited by 600nm low-stress LPCVD (low-pressure chemical vapor deposition) to be the electrical isolation layer. Next, a 500nm LPCVD polysilicon film would be deposited as the first polysilicon structural layer. Photolithography makes the designed pattern on this layer. The photoresist layer is used as the mask to make a plasma etch in this process without a need for an extra hard mask. The sacrificial layer of 2.0 μm PSG would be deposited by LPCVD and annealed one hour in 1050°C. The annealing reduces residual stress in the structural layer and improves fatigue life. This layer can be patterned for making the anchors of the suspended structure and some dimples can be added to prevent the sticking of structural layers after removing the sacrificial layer. After patterning the anchors by RIE on the sacrificial layer, a 2.0 μm polysilicon layer would be deposited, a 200nm of PSG added to it, and annealed one hour at 1050°C for doping. This structural layer pattern uses the PSG layer as a hard mask. The hard mask would be removed by RIE after patterning. The second sacrificial layer of PSG with a thickness of 750nm would be deposited and patterned. The pattern makes space to connect the next layer to the previous polysilicon layer or to the first one. The third and last 1.5 μm polysilicon layer would be deposited followed by a 200nm of PSG as the hard mask and dopant. Then they would be annealed for one hour in 1050°C. After patterning of the polysilicon layer, the PSG would be removed and a 0.5 μm of metal would be deposited for probing, bonding, electrical routing, and highly reflective mirror surfaces. This layer would be patterned by lift-off and then the wafer would be diced. To release the suspended structures, the sacrificial oxide layers should be released by immersion in 49% HF (Hydrofluoric acid) at room temperature. The samples can be washed with deionized water and alcohol and dry in 110 °C oven [101]. In the design considered in this research, the first polysilicon layer is considered as the fixed electrode, the second polysilicon layer is etched away totally, and the third polysilicon layer is considered as the movable electrode. This made a higher air gap between electrodes, which is the thickness of both sacrificial layers (2.75 μm and the movable electrode thickness of 1.5 μm . In the case of a custom manufacturing process, the air gap can be considered a design variable in

topology optimization. The design of each layer for the PolyMUMPs process has limits and rules that should be satisfied for manufacturing. But there are some general limits that are available in any surface micromachining and photolithography. These limits are addressed in the design and the rest are adjusted later only for the PolyMUMPs process.

2.6 Limitation in surface micromachining

Any surface micromachining process such as PolyMUMPs makes the desired structure by several steps of deposition and patterning by lithography. Deposition of structural or sacrificial layers can have some deviation from the desired thickness but they are not considerable in most of MEMS applications. Patterning by lithography, on the other hand, has some errors regarding lateral etches and alignment errors. In lithography, the alignment of the mask with the previous patterned shapes and etching of the desired pattern comes with errors. These errors have a considerable effect on the performance of a MEMS device. These errors can be measured with metrology methods and applied to the design [102, 103]. Error compensation methods are already developed for traditional machining processes [104]. In this section, a process of photolithography has been performed in the clean room to find and measure possible errors in patterning by lithography. The process started with cleaning a $500\mu m$ borosilicate wafer as substrate, rinsed 5 minutes in piranha, and dried in a hotplate at $130^{\circ}C$ for 15 minutes. Then, a standard Sputter deposition was made for 900 seconds at a very high vacuum ($< 4 \times 10^{-7} Torr$) to get $100 - 110nm$ of Chromium. Then a layer of photoresist was deposited. Deposition of photoresist starts with a Spin coating the TI-PRIME adhesion promoter and baking the sample on the hotplate at $100^{\circ}C$ for 3 minutes. After cooling down for 1 minute, the photoresist (AZ1518) was deposited by spin coating and soft baked on the hotplate at $100^{\circ}C$ for 1.5 minutes. After alignment and hard contact with the mask, the photoresist is exposed by $47mJ/cm^2$ at $365nm$. Then the sample was developed by immersion in dilute AZ351 developer for 1 minute, rinsed in DI water, and blown dry with a nitrogen gun. The chrome is etched later with Chrome Etch 18, rinsed in DI water for 1 minute, and the rest of the photoresist was removed by AZ100 remover bath. Then samples were dried with blow dry and dimensions are measured with a microscope. The results from this simple photolithography patterning showed that having a small particle-like dust or impurity in a sample can make a considerable change in functionality. For example, Fig. 2.6 shows the effect of a small dust particle to prevent etching in a small location and make a short circuit in the accelerometer.

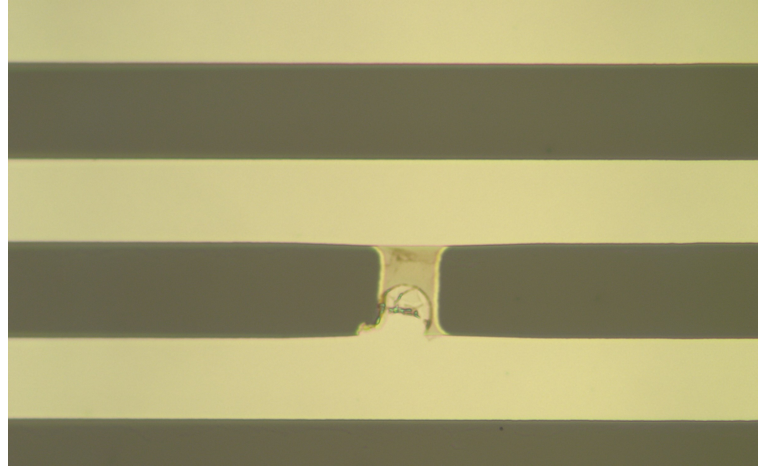


Figure 2.6 – Effect of a small dust particle on the patterns made with photolithography.

The error in the manufacturing shown in Fig. 2.6 comes from the experimental error. This type of error can be modeled as uncertainty in the design [105]. If this error is high in a case, the design should give more freedom to the thickness of elements to prevent or reduce the effect of such errors. Another error observed in the results of photolithography is over-etching by late removal of the sample from the etchant. As shown in Fig. 2.7, if the sample is removed from the bath of etchant just a few seconds later than the processing time or the density of chemical etchant is higher than the expected composition, the dimension of etched parts will be bigger than the nominal values.

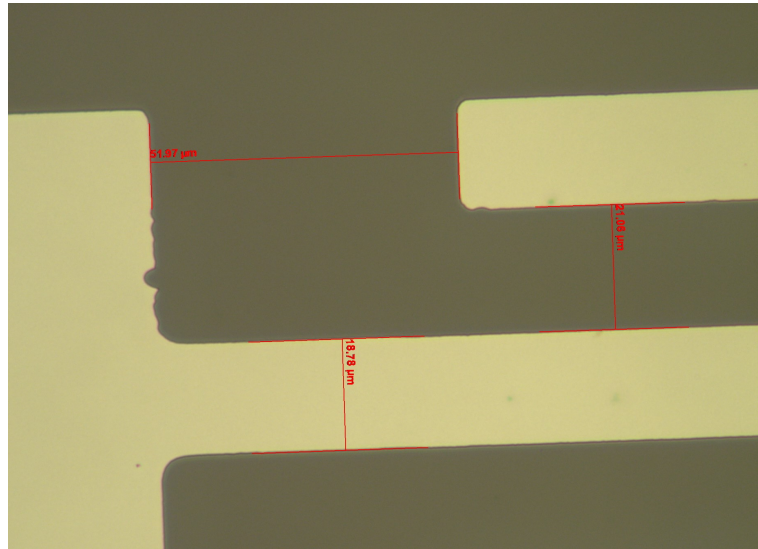


Figure 2.7 – Over etching and change of dimensions by keeping the sample in etchant for a longer time.

According to Fig. 2.7, extra time causes lateral etching in the sample and changes the dimensions of the pattern. In this experiment, an extra 30 seconds changed the dimensions by $1\mu m$ and $0.5\mu m$ in the horizontal and vertical directions, respectively. This is another parameter that should be in the design as uncertainty and if an element should be very

narrow in the design, special considerations would be necessary for keeping the required tolerances in the design [106]. Other properties of the etching process are minimum feature size and the possibility of making sharp edges. As shown in Fig. 2.8, inside of corners and outside of sharp edges change due to exposure surface to etchant in the lithography process.

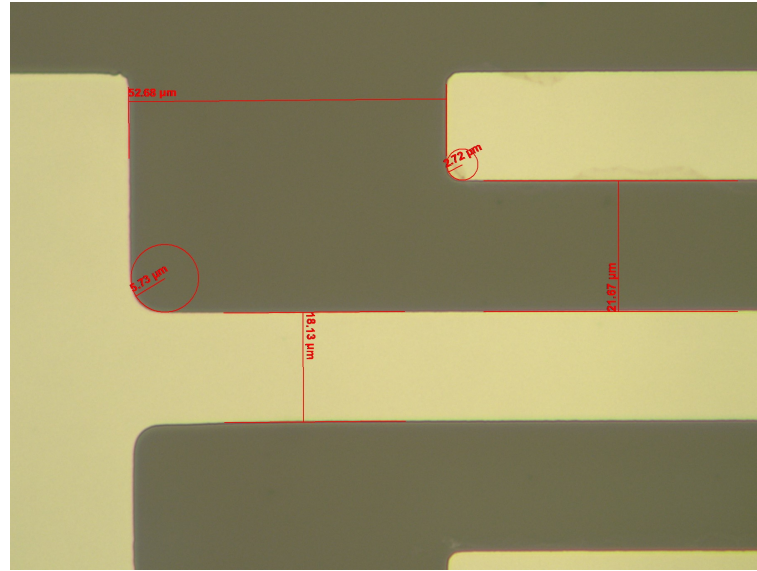


Figure 2.8 – Change of corners and edges in etching and measured radius.

As shown in Fig. 2.8, the corners and edges produce a round shape by chance of reaching the etchant to substrate and etch rates. This radius varies by the time of etching and angle of contact. It can be measured and modeled in a design. It has been shown in this study that morphological operators can model this phenomenon for edges and corners to predict the etching shapes and redesign the mask if necessary. The next section introduces morphological operators and their mechanism of performance for getting familiar with this concept. In the next chapter, these operators are used for the post-processing of the TO results.

2.7 Morphological operators

Term morphology, in general, is the study of shape and structural arrangement. Shape adjustment has various applications in image processing including a number of methods making a change in structure based on the relationships of different components in a shape. The primary goal of these operators is correcting flaws in a shape based on the final requirement. This way, key characteristics of a form will be preserved while imperfections are removed to enhance the required output. The fundamental concept behind the implementation of morphological operations is the basics of set theory such as union, intersection, complement, and reflection operators. Among a wide range of morphological operators, there are two fundamental ones called dilation and erosion which are mostly

used in various applications. As dependent operators, opening and closing are the most common ones that have been used efficiently in post-processing for micromachining and are introduced here in detail. Any morphological operation uses a small matrix structure to implement its algorithm. This matrix is called Structuring Element (SE) and its role is the same as a mask or convolution kernel in image processing. The structuring element is a small matrix working as a probe to analyze each subsection of a shape and decide the required change based on the interaction of the components inside the subsection. In better words, the purpose of using SE is to examine or extract the required properties in a predefined boundary. The dimension of SE is variable, but it is usually in rectangular form with odd dimensions. Each structuring element has a predefined origin that can be anywhere inside or even outside the element. But the more common form is defining the origin at the center of SE and that is the reason for using odd dimensions in forming SE. Origin of SE specifies the component of the shape that is under examination and other parts of SE specify the neighborhood consisting of components affecting the change. Translation of SE is based on its origin movement. Therefore, in order to examine the change in any component in a shape, the origin of SE should be placed on that component and then the calculations would be done. There are two general types of SE named flat and non-flat. A flat structuring element is a binary element consisting of zeros and ones with the option of not showing zeros in the matrix. Non-flat SE is a 3D element consisting of double numbers whose components are not used in the computation like zeros in flat SE. Deciding on the type and details of SE is among the important decisions that are dependent on the application. Following, four main morphological operators including dilation, erosion, opening, and closing are introduced. Each of these operators works with both binary and gray-scale elements (with intermediate properties). Explanation and formulation are based on flat SE since it is the type used in this study [107].

2.7.1 Dilation

Dilation is a morphological operator that enlarges a shape. This happens in two different ways for binary and gray-scale images. In binary images, a shape will grow by adding to the number of pixels in the foreground and reducing the number of zero pixels in the background. Dilation is used for removing holes or missing parts in a continuous area, repairing breaks, and smoothing the boundaries of an object. This is a type of repair for images or structures with non-smooth boundaries. Eq. (2.42) represents the formulation for dilating element A by structuring element B , where \oplus is the dilation sign and z represents the acceptable components' locations after dilation such that reflected SE around its origin, transferred to location z has any intersection with image A .

$$A \oplus B = \{z | (\hat{B})_z \cap A \neq \emptyset\} \quad (2.42)$$

To use dilation in gray-scale elements, some changes are needed. Eq. (2.43) represents formulation of dilation in gray-scale images, where $f(x, y)$ stands for the image, $b(s, t)$ shows flat structuring with (s, t) as active pixels in SE and D_b is the domain of SE b . Minus sign in term $f(x - s, y - t)$ is showing 180 degrees rotation. Therefore, instead of rotating SE before calculation, rotated coordination will be considered in the formulation. For example, if coordinate $(1, 1)$ is active in the SE, it is showing that the pixel of the image under the $(-1, -1)$ location should be considered active in the calculation.

$$[f \oplus b](x, y) = \max_{(s, t) \in D_b} \{f(x - s, y - t)\} \quad (2.43)$$

2.7.2 Erosion

The erosion operation, the opposite of dilation, causes an object in the image to lose its size. So the number of pixels in the foreground decreases and the number of pixels in the background increases. Erosion can remove features that are smaller than the selected SE, disconnect attached objects, delete noisy joints and sharpen the boundaries of an object. Eq. (2.44) represents the erosion of image A by structuring element B which consists of a set of all the acceptable components' locations z such that active components of SE translated to z by completely inside image A . This way, an eroded image would always be a subset of the input image. \ominus stands for the erosion operator in Eq. (2.44).

$$A \ominus B = \{z | (B)_z \subseteq A\} \quad (2.44)$$

Erosion in gray-scale images happens with the same goal but with a different formulation as represented in Eq. (2.45). In this equation, \ominus is the erosion operator sign, $f(x, y)$ is the input image representation, $b(s, t)$ is a flat SE, and D_b shows the domain of SE by consisting of active pixels. Based on the procedure represented in Eq. (2.45), the origin of the SE is moved to each pixel of the input image, the active pixels of the image in the created window is specified based on the ones in the SE, and the minimum gray-scale value between all the active pixels is found.

$$[f \ominus b](x, y) = \min_{(s, t) \in D_b} \{f(x + s, y + t)\} \quad (2.45)$$

2.7.3 Opening

The opening is a combination of erosion and dilation and happens when erosion operation takes place and then the output image would be dilated with the same structuring element. The opening can eliminate thin bridges and remove small regions of the foreground in a binary image and can smooth bright features in a gray-scale image which leads to a darker image in general. Eq. (2.46) represents opening formulation where image A is opened by SE B , \circ is the sign of opening, \ominus is the sign of erosion and \oplus is the sign of dilation. In the case of a gray-scale image, Eq. (2.43) and Eq. (2.45) would be used in

the opening operation and in the case of a binary image, Eq. (2.42) and Eq. (2.44) would be considered while opening operation is taking place.

$$A \circ B = (A \ominus B) \oplus B \quad (2.46)$$

2.7.4 Closing

Closing is a combination of erosion and dilation operations but with a change of order in the opening. It means that in closing, the dilation operation will be followed by erosion on the output image using the same SE. Closing fuses narrow breaks, removes thin gaps and eliminates small regions of background in a binary image, and smooths dark features in gray-scale images in a way that the output image will be seen brighter. Eq. (2.47) represents closing operation, where image A is closed by the SE B , and \bullet is the closing sign. As it is explained previously, the type of equation used for dilation and erosion is compatible with the type of input image.

$$A \bullet B = (A \oplus B) \ominus B \quad (2.47)$$

According to the mechanism of performance and ability to elaborate structures in binary or gray-scale design, morphological operations, and especially close operators are used in this study for the post-processing of mechanical structures obtained from TO.

3 Methodology and results

3.1 Topology Optimization with SA and crystallization factors

Simulated annealing optimization algorithm has been used successfully in the literature as an optimizer in TO problems [108]. In TO with SA, the same procedure of SA as shown in Fig. 2.5 can be used to evaluate the objective functions and converge to an optimum solution. The TO algorithm with SA starts from a random initial solution and a maximum temperature (T_{max}). The initial solution is the distribution of the discrete elements with random density. The domain should be discretized with meshes that are fine enough to cover the behavior of the structure, but coarse as much as possible to have reasonable computational costs. An external loop deals with the temperature and reduces the temperature by a cooling schedule (α). Inside this loop and for each temperature, several new solutions will be generated and evaluated. The evaluation uses Eq. (2.27) and Eq. (2.28) to calculate the change in the energy level of the objective function. Then, the SA criteria decides to accept or reject the new solution. If the solution gets acceptance it would be served as the current solution for the next iteration. Regardless of acceptance or rejection of the previous solution, the new solution would be generated in a random location and with random density in the implementation of conventional SA algorithms. This loop ends when $N_{iteration}$ solutions are generated and evaluated. Finally, the optimization ends by reaching the freezing temperature. Algorithm 1 briefly shows the TO algorithm with conventional SA.

The number of generated new solutions in each temperature is called the number of iterations ($N_{iteration}$). The number of iterations should be high enough to make sure the domain is sampled enough to find the global optima independent of the initial solution. The number of iterations is dependent on the physics of the optimization problem, domain, constraints, objective of optimization, and method of generating new solutions [109]. A practical rule of thumb to select a high enough number of iterations is to generate $20N$ new solutions in each temperature, where N is the number of discrete elements in the design domain [90]. In the case of TO, evaluation of the objective functions usually needs FEA which is usually expensive in the term of computations. Consequently, FEA and evaluation of $20N$ iterations in each temperature need a very high computational cost. It makes TO with SA an inefficient method for daily TO applications. Improving the random search strategy can make the optimization process more effective to find the optimum solution. Furthermore, a lower number of iterations would be enough to find the optimum topology without a need to perform high-cost computations. One of the search strategies that can

Algorithm 1 Topology Optimization with Simulated annealing

```

1:  $x_{current} = rand(0, 1);$                                 ▷ Random initial distribution of material
2:  $T = T_{max};$                                               ▷ Set initial temperature
3: while  $T > T_{min}$  do                                       ▷ Check temperature for external loop
4:    $v = 0;$                                                 ▷ Reset number of iteration in new temperature
5:   while  $v < N_{iteration}$  do                               ▷ Check number of solutions for internal loop
6:      $t = rand(1, N);$                                        ▷ Select a random element to change
7:      $x_{new}(t) = rand(0, 1);$                                ▷ Random change of selected element
8:      $\Delta E = F(x_{new}) - F(x_{current})$                  ▷ Calculate change of energy level
9:     if  $\Delta E < 0$  then                                     ▷ Acceptance for improving solution
10:       $x_{current} = x_{new};$ 
11:     else
12:       if  $P(\Delta E) < rand(0, 1)$  then                 ▷ Acceptance with probability function
13:         $x_{current} = x_{new};$ 
14:       end if
15:     end if
16:      $v = v + 1;$                                        ▷ Count number of iterations in the current temperature
17:   end while
18:    $T = \alpha T$                                          ▷ Reduce the temperature
19: end while

```

lead to generating more efficient new solutions in SA is the crystallization heuristic [110]. For a continuous variable, the crystallization heuristic controls the probability of density distribution. It increases the step size for the generation of a random solution at the early stages of optimization (exploration). However, it reduces step size near the convergence to the optimum (refinement). Crystallization heuristics helps to have enough sampling at the exploration phase of optimization with SA. So, lower numbers of iterations would be enough to reach the global optimum solution. Also, in the refinement jumps would be smaller in new solutions and the solution from SA reaches closer to the exact optimum. In a mathematical optimization problem with SA, the crystallization factor is a bounded number assigned to each location and can be used by the directional vectors to generate new solutions. Eq. (3.1) shows the generation of a new solution x^* using current solution x and crystallization factors (Bates distribution).

$$x^* = x + \frac{1}{C_i} \sum_1^{C_i} rand(\frac{-1}{2}, \frac{1}{2}). \Delta r_i . e_i \quad (3.1)$$

where i represents locations in the neighborhood of x with a predefined distance, C_i is the crystallization factor for the i -th variable, Δr_i is the fixed step size associated with the i -th variable, and e_i is the direction of the i -th variable. The step size Δr_i depends on the search interval and can be estimated by Eq.(3.2) with enough exploration [110].

$$\Delta r_i = \frac{(max_i - min_i)}{4} \quad (3.2)$$

where $[min_i, max_i]$ is the range domain for the i -th variable. In TO with SA, the design domain can be discretized by N elements and a crystallization factor of C_k is assigned to

the k -th element. where k is the number of each element from 1 to N . At the beginning of the optimization, a minimum value of 1 is assigned to the crystallization factor of each element. That means the jumps are in the highest possible level. Using the density approach for each element, variables of optimization are densities of each element that can vary in $[0, 1]$. Mechanical properties of each element such as local stiffness matrix and mass matrix can be calculated using the power law in Eq. (2.37). Any new solution can be generated using the current densities and crystallization factors in the neighborhood of the targeting element. So, a new solution in the domain can be generated by random selection of an element ($t = rand(1, N)$), and changing its current density ($x_{current}(t)$) to the new density ($x_{new}(t)$) using Eq. (3.3).

$$x_{new}(t) = x_{current}(t) + \frac{1}{C_i} \sum_1^{C_i} rand(\frac{-1}{2}, \frac{1}{2}). \Delta r_i . e_i \quad (3.3)$$

where Δr_i is the step size in each direction. Then, the new solution of x in the domain is the current solution (initial solution for the start and accepted solutions in the later steps) with replaced t -th variable with the new density from Eq. (3.3). Now, it is time to check the feasibility of the new solution regarding constraints. As discussed earlier, constraints can be added to the objective function with weighting coefficients as shown in Eq. (2.32). But it can distract the convergence of optimization when many different constraints are applied. Since in this study we are applying various constraints from various points of view, it is more efficient to check the constraints separately after the generation of new solutions. So, for any newly generated solution, it would be checked for all of the constraints before further evaluation. If the new solution invades any constraint, the process of generating random new solution repeats till reaching a solution that satisfies all of the constraints. The next step is to evaluate the new solution by SA criteria. A finite element analysis (FEA) calculates the mechanical behavior of the system such as displacements and resonance frequencies. Then the energy level change ΔE would be calculated by Eq. (2.27) and the new solution gets acceptance for improving solutions ($\Delta E < 0$ or by the probability function of Eq. (2.28)). If the new solution gets acceptance, the value of the crystallization factor for the changed element t and its neighborhood in a radius of Δr will be reduced (negative feedback). The reduction can be applied by dividing the previous crystallization factor by two (for faster convergence) or by subtracting a constant number (for slower changes). In this study, a reduction of 1 showed better convergence for several structural TO problems. It should be noted that the crystallization factor reduction can be continued till reaching a minimum value of 1. After that, more reduction cannot be applied and the crystallization factor remains as the minimum value. The opposite strategy applies when the new solution gets rejection by SA. The value of the crystallization factor for the t -th element and its neighborhood increases by a constant number of 1 (positive feedback). If the value of the crystallization factor reaches more than the maximum value (20 in the benchmark problems studied here), it will get the maximum value. Change in

the crystallization factor means that if the change in the randomly selected element of t improves the objective function, that element or its neighbors have an important effect on the improving objective function. Consequently, that element gets a higher possibility of changes the next time when selected for a change. If the acceptance is due to the probability factor of Eq. (2.28), the crystallization factor still gets negative feedback to keep the possibility of exploration, especially at the early stages of the TO and it helps to escape from local minima. The value of the crystallization factor also can be used to analyze the convergence of a solution and monitor any element in the design domain. At the end of TO, the values of the crystallization factor reach or get near their maximum value due to the high rate of rejections. After repeating the generation of $N_{iteration}$ new solutions and evaluation, the temperature decreases similarly to conventional TO with SA. The crystallization factors for each element stay the same in the new temperature and only changes when accepting or rejecting a new solution. The process stops by reaching the predefined rejection ratio or the freezing temperature. The proposed algorithm for TO with SA and crystallization heuristic search showed in algorithm 2.

Algorithm 2 TO with SA and crystallization heuristic

```

1:  $x_{current} = rand(0, 1);$                                 ▷ Random initial distribution of material
2:  $C_j = 1; \quad j = 1, \dots, N$                                 ▷ Set initial crystallization factor
3:  $T = T_{max};$                                                 ▷ Set initial temperature
4: while  $T > T_{min}$  do                                        ▷ Check temperature for external loop
5:    $v = 0;$                                                 ▷ Reset number of iteration in new temperature
6:   while  $v < N_{iteration}$  do                                ▷ Check number of solutions for internal loop
7:      $t = rand(1, N);$                                         ▷ Select a random element to change
8:      $\Delta r_i = ||x(t) - x(i)|| < r$                         ▷ Neighboring elements inside a radius of r
9:      $x_{new}(t) = x_{current}(t) + \frac{1}{C_i} \sum_1^{C_i} rand(\frac{-1}{2}, \frac{1}{2}).\Delta r_i.e_i;$     ▷ Generate new solution
10:     $\Delta E = F(x_{new}) - F(x_{current})$                     ▷ Calculate change of energy level
11:    if  $\Delta E < 0$  or  $P(\Delta E) < rand(0, 1)$  then          ▷ Acceptance
12:       $x_{current} = x_{new};$ 
13:       $C_i = C_i - 1;$                                         ▷ Negative feedback
14:    else                                                    ▷ Rejection
15:       $C_i = C_i + 1;$                                         ▷ Positive feedback
16:    end if
17:
18:    if  $then C_i < 1$ 
19:       $C_i = 1;$                                             ▷ Minimum crystallization factor
20:    else
21:      if  $C_i > 20$  then
22:         $C_i = 20$                                           ▷ Maximum crystallization factor
23:      end if
24:    end if
25:     $v = v + 1;$                                             ▷ Count number of iterations in the current temperature
26:  end while
27:   $T = \alpha T$                                             ▷ Reduce the temperature
28: end while

```

To evaluate the proposed approach, three benchmark problems are solved by the GTO algorithms in the literature and are compared with the results obtained from the proposed method. The first benchmark TO problem is the maximization of stiffness in a cantilever beam with a point load at the free end as shown in Fig. 3.9. The thickness of the beam is considered constant and TO determines the distribution of the material in a two-dimensional design domain.

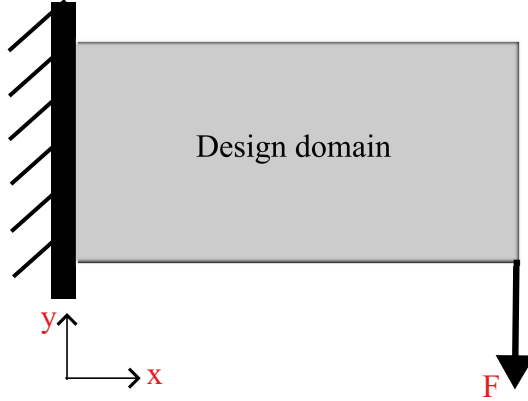


Figure 3.9 – Schematic of the cantilever beam with point load (F) at the free end.

The design domain in Fig. 3.9 divided by N discrete elements and density of the i -th element ($i = 1, \dots, N$) can be anything in the range of $[0,1]$. Using the SIMP method, mechanical properties of elements can be obtained from Eq. (2.37). A penalization factor of $p = 3$ is used to penalize mechanical properties [73]. Using the global stiffness matrix K and the load matrix F , the displacement matrix U can be calculated by Eq. (3.4):

$$KU = F \quad (3.4)$$

The objective of TO is to minimize compliance. The compliance of a structure can be defined as the strain energy from the work done by the force in the direction of displacements as shown by Eq. (3.5):

$$c(x) = F^T U \quad (3.5)$$

Combining Eq. (3.4) and Eq. (3.5) gives the strain energy as a relation of displacement and stiffness matrix. For the whole structure, the strain energy can be written as a summation of strain energy for each element as shown by Eq. (3.6).

$$c(x) = \sum_{e=1}^N (x_e)^p u_e^T k_e u_e \quad (3.6)$$

where x_e , u_e , and k_e are the density, displacement, and stiffness matrix for each element. The compliance defined here is differentiable and the partial derivatives of the objective function can be calculated using Eq. (3.7) for each element to be used in GTO.

$$\frac{\partial c}{\partial x_e} = \sum_{e=1}^N -p(x_e)^{p-1} u_e^T k_e u_e \quad (3.7)$$

Then the sensitivity filter from Eq. (2.41) can be used to smooth the changes in GTO in the literature [111]. a volume constraint is applied to the TO problem to see the optimized topologies in different volumes. The desired volume is a constraint defined by the ratio of the desired volume to the volume of the whole domain as Eq. (3.8).

$$VF = \frac{V(x)}{V_0} \quad (3.8)$$

The design domain is discretized to $N = (90 \times 45)$ elements and optimized for different volume fractions by the GTO method in the literature [111] and the proposed method. For the TO with the proposed method with SA, the optimization algorithm was selected by a few trial runs and analyzing the convergence to an optimum solution. Table 2 shows the SA parameters selected for the cantilever beam problem.

Table 2 – Parameters of SA for the design of the cantilever beam.

Parameter	Description	Value
T_{\max}	Initial temperature	100
T_{\min}	Freezing temperature	0.001
α	Cooling schedule	0.85
$N_{iteration}$	Number of iterations in each temperature	1000
$C_{min}(i)$	Minimum crystallization factor	1
$C_{max}(i)$	Maximum crystallization factor	20
Δr	step size	2

To select parameters of SA in Table 2, some information about the convergence should be analyzed. To find the lowest but sufficient number of iterations, the optimization process has been done several times with an increasing number of iterations till seeing that by increasing the number of iterations, the objective function not improving significantly. Fig. 3.10 shows the value of the objective function (compliance) versus the number of iterations in a logarithmic scale for a volume fraction of 0.5.

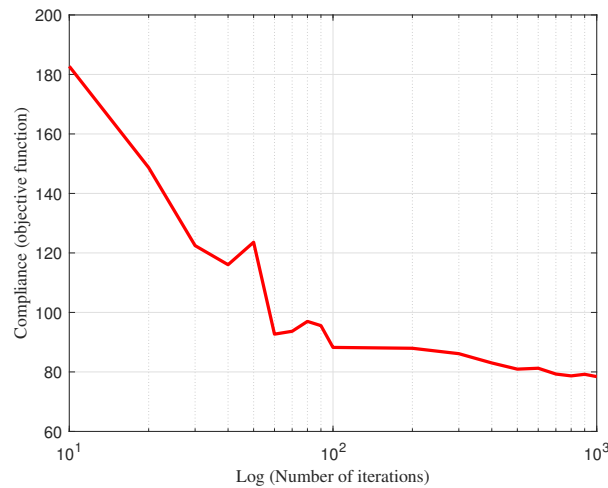


Figure 3.10 – Minimized compliance from the proposed method versus the number of iterations for the cantilever beam problem.

As shown in Fig. 3.10, the optimized solution decreases considerably by increasing the number of iterations from a few iterations to a hundred. After that, the compliance decreases slowly by increasing the number of iterations, which means the solution of TO is converging to the optimum solution. Even for 100 iterations in each temperature, the solution is close to the optima and can be used for fast convergence if necessary. Usually in TO problems, a few fast runs can be helpful in generative design to select a design and then use a more detailed TO to reach the optimum design. Besides the number of iterations, the maximum and minimum temperatures (start and end temperature) are important parameters in TO with SA. The maximum temperature should be high enough to explore the design domain and have a high probability to jump to different solutions and sample the whole domain. Therefore, the number of accepted and rejected solutions are good parameters to study to track behaviors of the optimization process. As a rule of thumb in SA, 80% of solutions get acceptance in exploration and they gradually reduce to reach a value of zero. In some algorithms, it is also suggested to reduce the temperature when reaching 50% of accepted solutions to avoid extra explorations. But in both cases, the number of accepted solutions should reduce gradually till reaching zero or a very small number. Fig. 3.11 shows the number of accepted and rejected solutions in each temperature with a logarithmic scale.

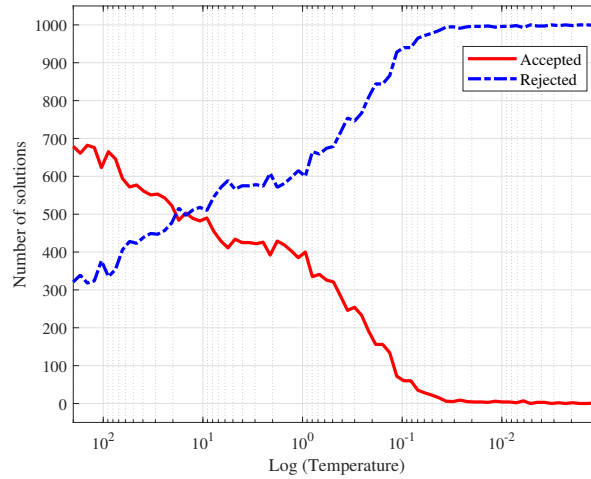


Figure 3.11 – Number of accepted and rejected solutions versus temperature in TO with SA for the cantilever beam problem.

As shown in Fig. 3.11, the number of accepted solutions is higher than the number of rejected solutions at the beginning of the optimization. This exploration situation should last for a few temperatures to accept enough solutions and get close to the global optimum. Then accepted solutions decrease and more new solutions get rejected. It happens gradually to make sure that the solution can still escape from a local optimum. When the solution gets close to the optimum solution, new solutions are mostly rejected and no further improvement is expected (or is not considerable). A few accepted solutions at the end of the process can still remain due to the possibility of accepted solutions with no change when the energy level change is zero. It usually happens in the case of binary TO where changes in density are from zero to one or vice versa. So, the new solutions can oscillate around the optimum point. In such cases, the value of the objective function can be analyzed with decreasing temperature and the freezing temperature (minimum temperature) is where the objective function is not improving anymore by decreasing temperature. Another parameter that can be analyzed to get information about the convergence of solutions in the proposed method is the crystallization factor of each element. The crystallization factor starts from a minimum value of 1 and varies between this minimum and a maximum of 20. Acceptance of a new solution results in decreasing the crystallization factor of the changed element and its neighbors. Rejection of a new solution, on the other hand, increases the crystallization factor in the targeting area. At the beginning of the TO, most of the generated solutions get acceptance to explore the domain. By converging to the optima, new solutions get more rejection and consequently, increase crystallization factors. So, the values of crystallization factors suppose to be the maximum value at the end of the TO for all elements. The changes of crystallization factor versus temperature showed in four different locations of the cantilever beam in Fig. 3.12

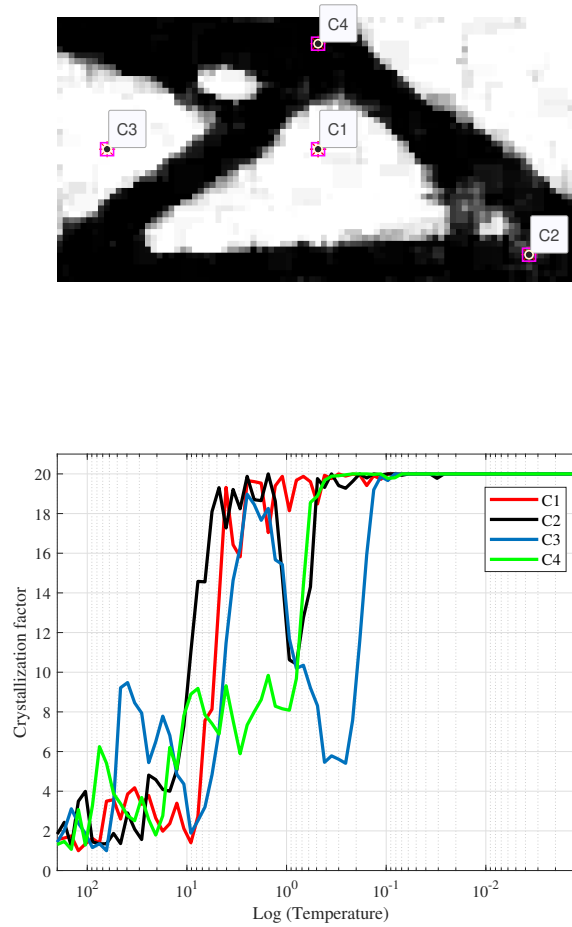


Figure 3.12 – Crystallization factor versus temperature for four locations of the cantilever beam in proposed TO method with SA.

As shown in Fig. 3.12, the values of the crystallization factor are reaching the maximum value faster in some areas of the design domain. These are the locations where elements and their neighborhoods should be void or solid in the optimum solution. So, the crystallization factors in such locations reach their maximum values faster, and changing these elements is not desirable anymore during the TO. On the other locations such as the borders of voids and solids in the optimum solutions, various changes happen during the optimization to find the exact locations of voids or solids. Crystallization factors in such areas converge to the maximum value slowly to give enough chance to the elements for changing their density and finding the best combination. If in a region values of crystallization factors stay small at the end of the optimization, it can be interpreted with several scenarios. One reason for having small crystallization factors is not evaluating enough solutions in the domain. In this situation, even if the objective function reaches a value and not improving anymore, it can be a local optimum and could change in another optimization run. An increase in the number of iterations or the cooling factor can help in this case to make sure converging to the optimum topology and reaching maximum crystallization factors at

the end of the optimization. Another scenario for having small crystallization factors in an area is the high sensitivity of that area such as boundaries of solids and voids. In this situation, reducing or increasing the density of elements can improve the objective function. It is similar to oscillating around the optimum point in a gradient-based optimization with large step sizes. To address this issue, a smaller step size should be used to select the neighboring elements for changing the crystallization factors and generate a new solution in Eq. (3.3). Also, refinement of the mesh size in that area can improve the convergence. For a more precise convergence, the mesh size and the step size can be refined in the last stages of the TO. It helps to get a better convergence with only a small increase in computational costs. The converged optimum solutions are verified with the results from GTO presented in [111]. Table 3 showed the minimum compliance of the cantilever beam in Fig. 3.9 from both methods with the same design parameters. Effective parameters such as modulus of elasticity are considered as one unit in both algorithms.

Table 3 – Compliance (C) of optimized cantilever beam from the GTO in the literature and the proposed method herein.

VF	GTO by Sigmund [111]	Proposed method	Error %
0.5	76.0523	80.6385	6.03
0.6	63.8762	65.7934	3.00
0.7	56.3239	59.3256	5.31
0.8	50.8085	52.4961	3.32
0.9	47.2017	48.4574	2.66

The results of minimum compliance from the proposed method in Table 3 show a good agreement with the results from the literature. The maximum error is about 6% in 0.5 of volume fraction. This small error is acceptable in many TO problems, while the proposed method has the main benefit of not needing gradient information of the objective function or constraints. In addition, the proposed method decreased the computational costs 3-times in comparison to the traditional TO with SA. Since the compliance is calculated from the strain energy in Eq. (3.6), any high-density element outside the domain with large displacement can increase compliance. Due to the random search nature of TO with SA, some gray elements (with intermediate density) still exist in the design domain as can be seen from the optimized topologies shown in Fig. 3.13. They can be removed by decreasing the minimum temperature in SA. But it will increase the computational costs considerably and in most cases removing them by post-processing can be more efficient. A post-processing algorithm for this TO is proposed in this research and discussed in the next section in detail.

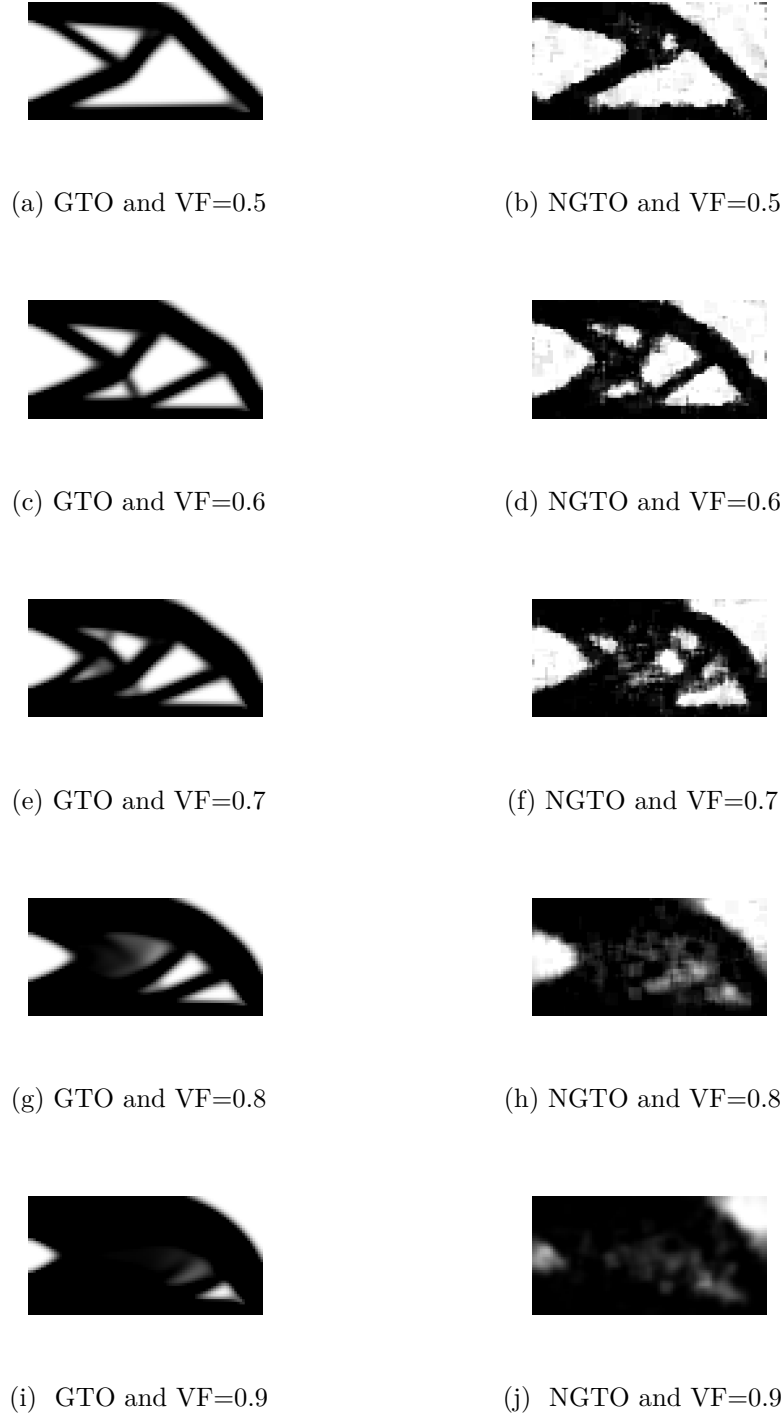


Figure 3.13 – Optimized topology of the cantilever beam for minimizing compliance with GTO from the literature (left) and the proposed method (right) for different volume fractions.

Optimized topologies shown in Fig. 3.13 have similar shapes in GTO and the proposed method. The gray area exists in GTO in the boundaries because both the existence or absence of material in these regions can be beneficial to improve the objective function. In the proposed method, the gray areas exist for the same reason and also because of the

random search nature of the method. In the other words, the density of some elements may not be covered many times in the random selection of targeting element to completely change it to a zero or one. Therefore, some gray elements can exist randomly in the domain with small effects on the objective function. But still, the values of minimized compliance in Table 3 and optimized shapes in Fig. 3.13 show a good agreement between the proposed method and the GTO in the literature [109].

The second benchmark problem that is used to verify the proposed method is the Messerschmitt–Bolkow–Blohm (MBB) beam. Fig. 3.14 shows the loading and boundary conditions in the MBB beam.

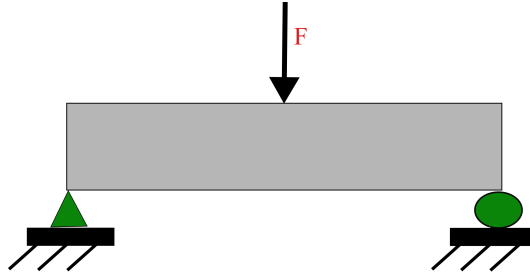


Figure 3.14 – Schematic of the MBB beam with a point load (F) at the middle.

The MBB beam in Fig. 3.14 is symmetric with a symmetry line in the middle. So the TO problem can be applied to half of the beam by considering no horizontal displacement at the middle of the beam. The design domain and boundary conditions in the half-MBB beam problem showed in Fig. 3.15.

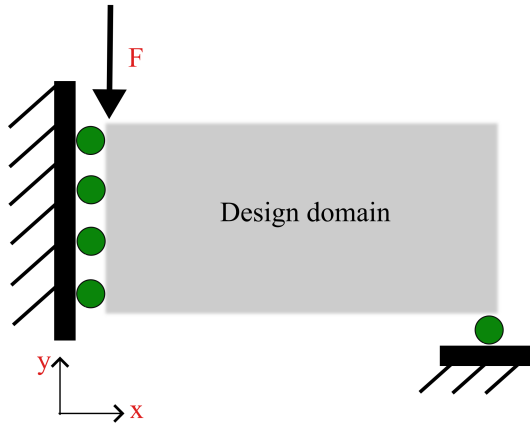


Figure 3.15 – Schematic of the half-MBB beam with a point load (F) and new boundary conditions.

The design domain of the half-MBB beam problem is divided by $N = 90 \times 45$ elements similar to the cantilever beam. The objective function of TO for the MBB beam problem with the point load in the middle is minimizing compliance subjected to volume fraction constraints. The objective function can be stated as minimizing strain energy of Eq. (3.6).

A few trial optimizations were performed with different numbers of iterations and the results are shown in Fig. 3.16.

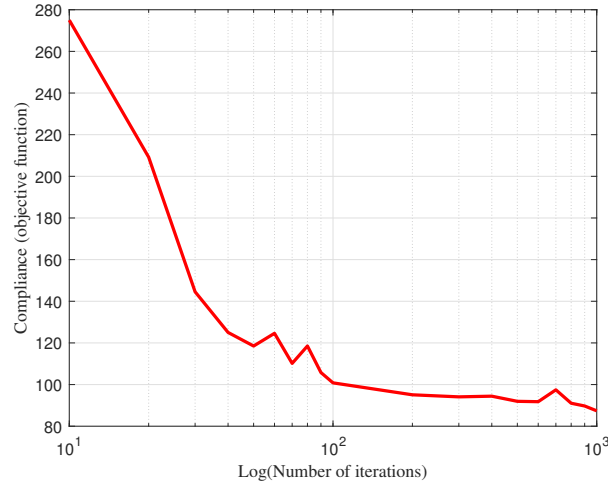


Figure 3.16 – Compliance from TO by the proposed method versus different numbers of iterations in the half-MBB problem.

It can be seen from Fig. 3.16 that the objective function (compliance) is staying almost in the same range for a number of iterations of more than one hundred. The convergence can be considered with any number of iterations of more than a hundred and more accurately with a thousand. This is a similar situation to the cantilever beam problem. It can be concluded that the number of iterations and other parameters in TO with SA are dependent on the size of the problems (number of elements) and the objective function. A similar analysis has been performed on the number of accepted and rejected solutions versus temperature to find out the proper maximum and minimum temperatures in SA. Based on the analysis and as expected because of similarity to the cantilever beam problem, the same parameters of optimization with SA from Table 2 used for the half-MBB TO with SA. The results of minimized compliance for the half-MBB beam problem showed in Table 4 at different volume fractions.

Table 4 – Compliance (C) of optimized half-MBB beam from the GTO in the literature and the proposed method herein.

VF	GTO by Sigmund [111]	Proposed method	Error %
0.5	84.1076	87.3889	3.90
0.6	71.1597	75.3780	5.93
0.7	62.1848	64.1766	3.20
0.8	56.3879	58.4739	3.70
0.9	52.0194	53.5109	2.87

The compliance of optimized topology with the proposed method shows a good agreement with the results from [111] in Table 4 by a maximum error of about 6%. This error is acceptable in many TO problems and can be reduced more by post-processing the results [112]. Optimized topologies of the half-MBB beam problem showed in Fig. 3.17 for various volume fractions.

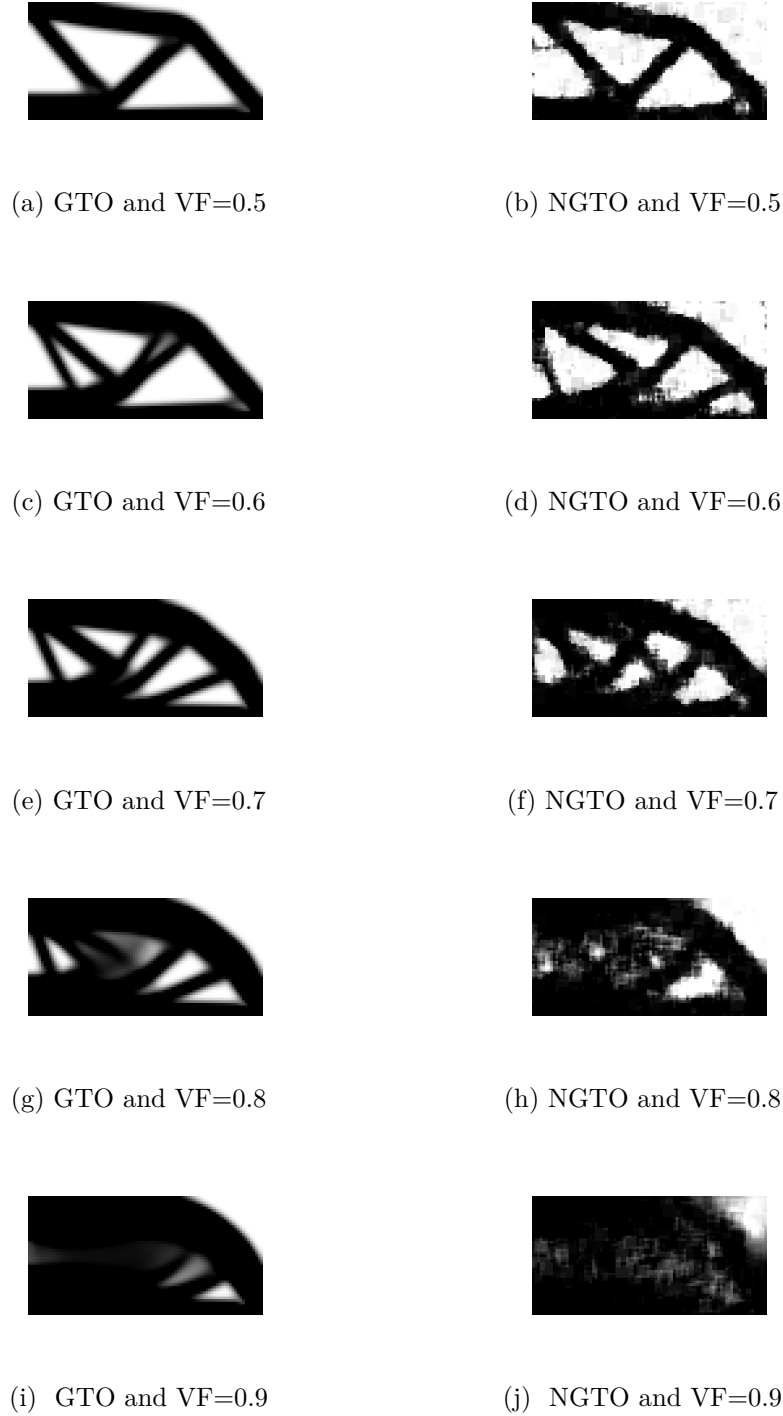


Figure 3.17 – Optimized topology of the half-MBB beam from the GTO in the literature (left) and from the proposed method (right) with different volume fractions.

The results presented in Fig. 3.17 show the optimized topologies from the proposed method for different volume fractions are similar to the results in the literature. The notable difference is having randomly distributed gray areas in the results from the proposed method. That is a consequence of using random search in the optimization process. Similar to the optimized topologies in the cantilever beam problem, the gray areas can be removed by increasing the resolution of the search or post-processing.

The third benchmark problem that is used here to verify the proposed method is a 3D heat transfer problem. For two systems with different temperatures, energy transfers from the system with a higher temperature to the system with a lower temperature to reach thermal equilibrium. In thermal equilibrium, the heat transfer problem can be written in the same format of Eq. (3.4), but U is finite element global nodal temperature vector, F is global thermal load vector, and K is global thermal conductivity matrix. Similar to Eq. (3.5), this compliance can be minimized to reach the maximum conductivity. So, Eq. (3.6) can be used to calculate thermal compliance by using the thermal conductivity matrix of each element k_e and the temperature of each element u_e . The heat transfer problem considered here is a 3D plate with a heat sink attached to the top middle as shown in Fig. 3.18.

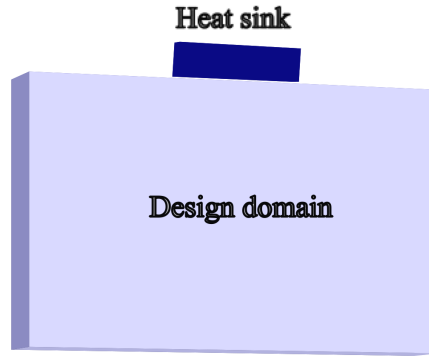


Figure 3.18 – Schematic of the heat conduction problem with a heat sink on the middle top.

To find the acceptable number of iterations in each temperature to sample the whole domain, the number of iterations gradually is increased for a 0.5 volume fraction in a few runs. The optimized compliance for each number of iterations is shown in Fig. 3.19 versus temperature in a logarithmic scale.

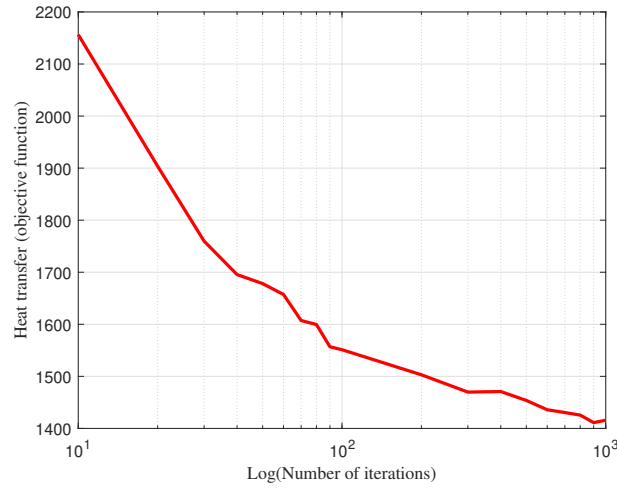


Figure 3.19 – Heat compliance from TO by the proposed method versus the number of iterations for heat transfer problem.

Fig. 3.19 shows that the objective function converges to a minimum value by increasing the number of iterations before $N_{iteration} = 1000$. So this number is selected as the number of iterations in the TO. The problem of maximizing heat transfer by TO is solved by the method of moving asymptotes (MMA) in the literature [113] and the proposed method. The design domain is considered as a 40×40 plane with a thickness of one element to make the results comparable. The same parameters in Table 2 has been used for optimization with SA. The results of the heat transfer compliance from [113] and the proposed method are presented in Table 5.

Table 5 – Heat transfer compliance (C) for a 3D plate with a heat sink on middle top from GTO in literature and proposed method.

VF	C from [113]	C from the proposed method
0.5	1504.5	1347.4
0.6	1271.0	1178.7
0.7	1139.3	1093.6
0.8	1081.1	1041.0
0.9	1025.4	1014.6

Comparison of results from the proposed method and the results from the literature in Table 5 show improvement of the heat transfer compliance in the proposed method. But it should be noted that in the case of conductive heat transfer, gray areas and checkerboards can improve the objective function. Therefore, small improvements in the objective function are because of the gray area and checkerboards at the boundaries of the optimized shape. Optimized topologies from the GTO in [113] and the proposed method are shown in Fig. 3.20 for different volume fractions.

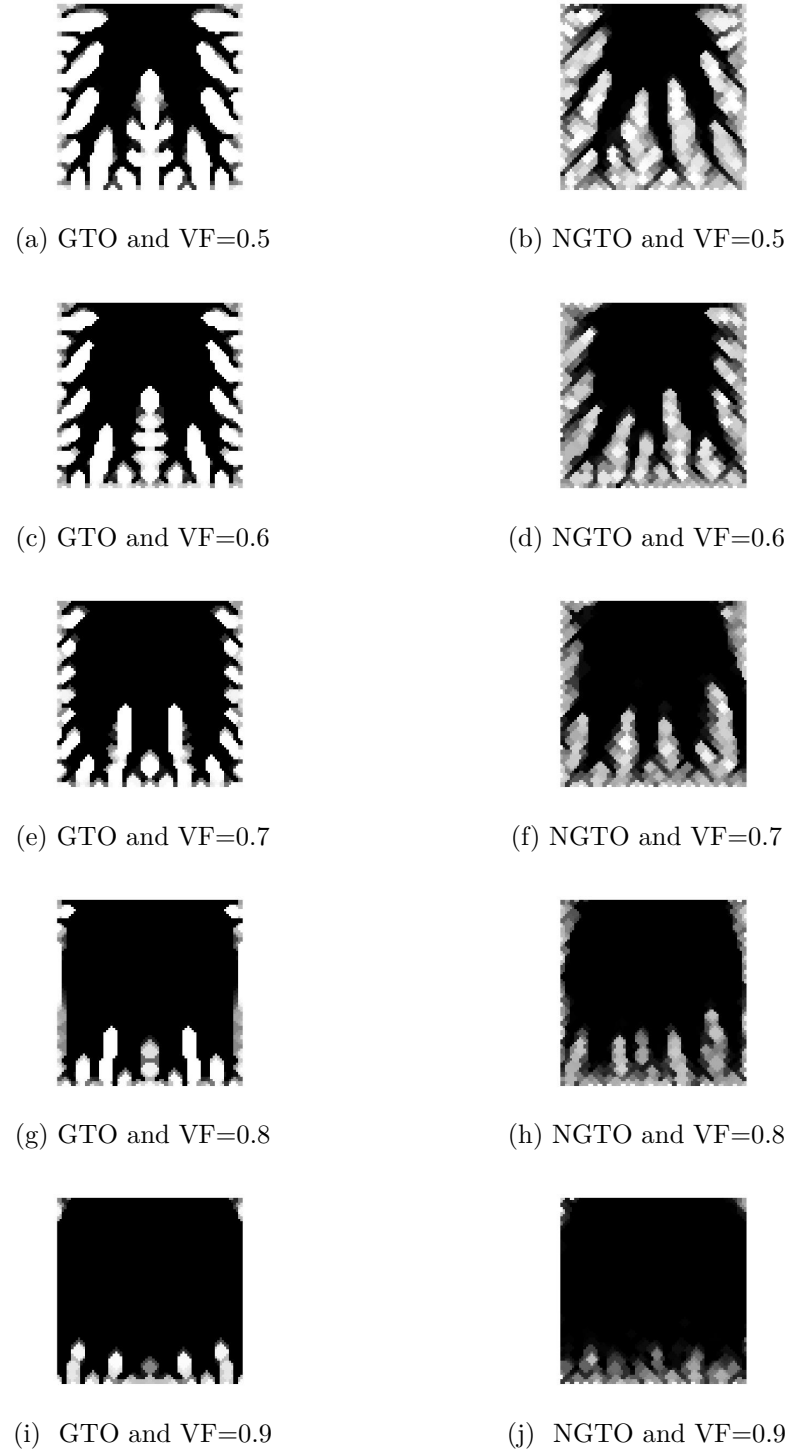


Figure 3.20 – Optimized topology of the heat transfer problem from [113] (left) and the proposed method (right) with different volume fractions.

The results of TO in Fig. 3.20 show a similar topology from the literature and the proposed method. Since this method is not using gradient information, the optimized design is not necessarily symmetric. But the optimum design is not obligated to be symmetric from the physic of the problem and while the compliance is the same, it can be considered as the optimum solution. After validating of the proposed method by

comparing it to some benchmark problems, it can be used for different TO problems. Fig. 3.21 shows the optimum design from the proposed method in a 3D cantilever beam with point force at the free end and constraint on 0.5 of volume fraction.

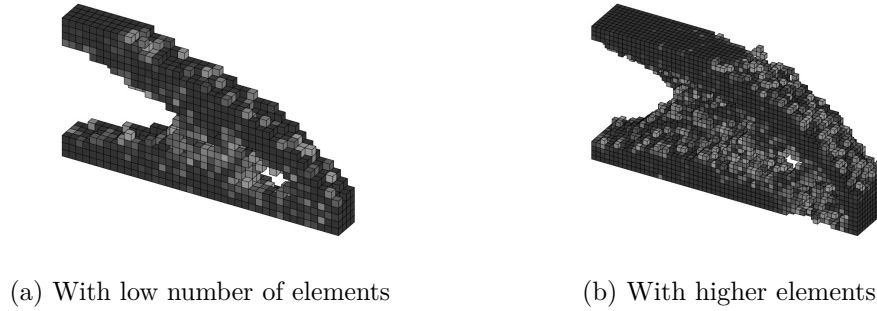


Figure 3.21 – Optimized topology of a 3D cantilever beam with 1000 iterations in each temperature and the proposed TO with SA and 0.5 volume fraction.

Optimized topology in Fig. 3.21 shows the 3D problem can be solved efficiently with just 1000 iterations in each temperature. Even by increasing the number of elements in the design domain, the algorithm can show a good estimation of the optimum solution with a reasonable computational cost. So, for more complex problems this algorithm still stays useful with fair accuracy that can be enough for a generative design comparison. To sum up, the proposed TO with SA and crystallization factors proved its functionality in various problems. As a meta-heuristic and NGTO algorithm, the proposed method can be used in a variety of TO problems. There is no need to calculate gradients of the objective function and constraints in this method. Non-convex and non-self-adjoint objective functions can be solved with this method according to the algorithm for generating new solutions and evaluations. It also can deal with different types of constraints including manufacturing constraints. Adding crystallization factors to this TO algorithm improved its convergence to the optimum solution with reasonable computational costs. This algorithm would be used in TO of the MEMS sensor in this research.

3.2 Post-Processing

The results from TO with SA showed a good agreement with the results from GTO in the literature. But there are some gray areas and non-smooth borders in the optimized design due to the random search nature of SA and numerical instabilities in FEA. So, the results should be elaborated to become feasible for manufacturing. In the case of GTO, the checkerboard problem is addressed by using sensitivity filters [73]. Sensitivity filters prevent rapid changes in sensitivity by applying the effect of neighboring elements' sensitivity by a weighting function. Consequently, the sensitivity of each element changes gradually and converges to smooth borders without checkerboard effects. Optimized designs from

GTO only have some gray areas in the borders. These gray areas can be changed to solids or voids simply by putting a threshold in the density. A threshold of 0.5 in density changes the elements with lower densities to void and the rest to solid elements. In the case of NGTO, there is no gradient information to be used with sensitivity filters. The crystallization factor introduced in this study for the TO with SA can be used to stabilize the convergence of TO with gradual changes in the generation of new solutions. But at the last stages of TO, crystallization factors are reaching their maximum value and cannot be used to smooth the boundaries or remove checkerboards. A design with checkerboards is not desirable in most manufacturing processes. But in the case of micromachining, the design has to meet more requirements to be feasible for manufacturing. Fig. 3.22 shows the simulation of surface micromachining for a mask with checkerboards. The mask is the optimized topology of a cantilever beam without post-processing and only changed gray elements to void or solid by a threshold.

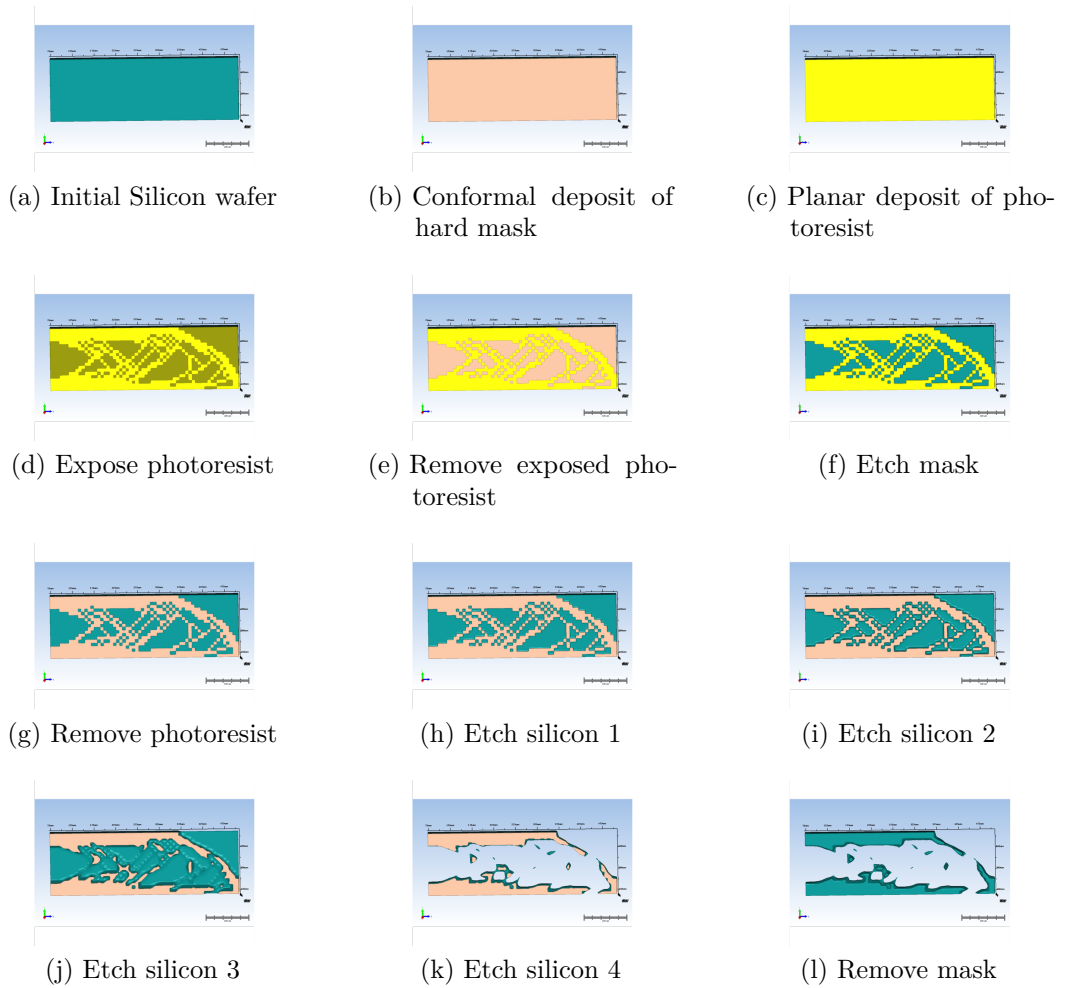


Figure 3.22 – surface micromachining process with a mask from TO without post-processing.

As shown in Fig. 3.22, an improper mask results in etching away the silicon wafer in tiny elements. Depending on the thickness of the silicon wafer, the minimum required size

of elements can be determined. The anisotropic properties of silicon in etching can increase these limits in some specific directions. Different strategies are used in the literature for applying manufacturing constraints in NGTO. Here a few methods are developed and tested for post-processing and filtering the results of TO with SA. One of the strategies is to apply density filters directly to the optimized topology. A density filter changes the density of each element by getting effects from the density of neighboring elements. The new density of each element can be calculated using Eq. (3.9).

$$x_i = \frac{\sum_{j=1}^N w_{ij} x_j}{\sum_{j=1}^N w_{ij}} \quad (3.9)$$

where w_i is the weighting function. The conic weights can be calculated using Eq. (3.10) as a linear decaying function outwards from the center of a circular area.

$$w_{ij} = R - d_{ij}; \quad \forall |d_{ij}| < R \quad (3.10)$$

where d_{ij} is the distance of element i from element j . The application of density filters makes the design more smooth and reduces small checkerboards. Simulations showed that using the density filter from Eq. (3.9) in the post-processing is more efficient by repeatedly applying the filter several times. Applying density filters to the results from TO with SA and simulation for micromachining showed performing density filters to the final topology by 100 times has efficient effects for manufacturability with micromachining. The TO results of the cantilever beam problem in Fig. 3.13 post-processed with density filters (applied 100 times to the final design) and used a threshold of 0.5 to change gray elements to solid or void. In the case of GTO from the literature, applying density filters does not make considerable changes to the design. In the case of NGTO, the application of density filters can make the design more suitable regarding the continuity and smoothness of boundaries. The topologies of the optimized cantilever beam problem with different volume fractions after post-processing are presented in Fig. 3.23.

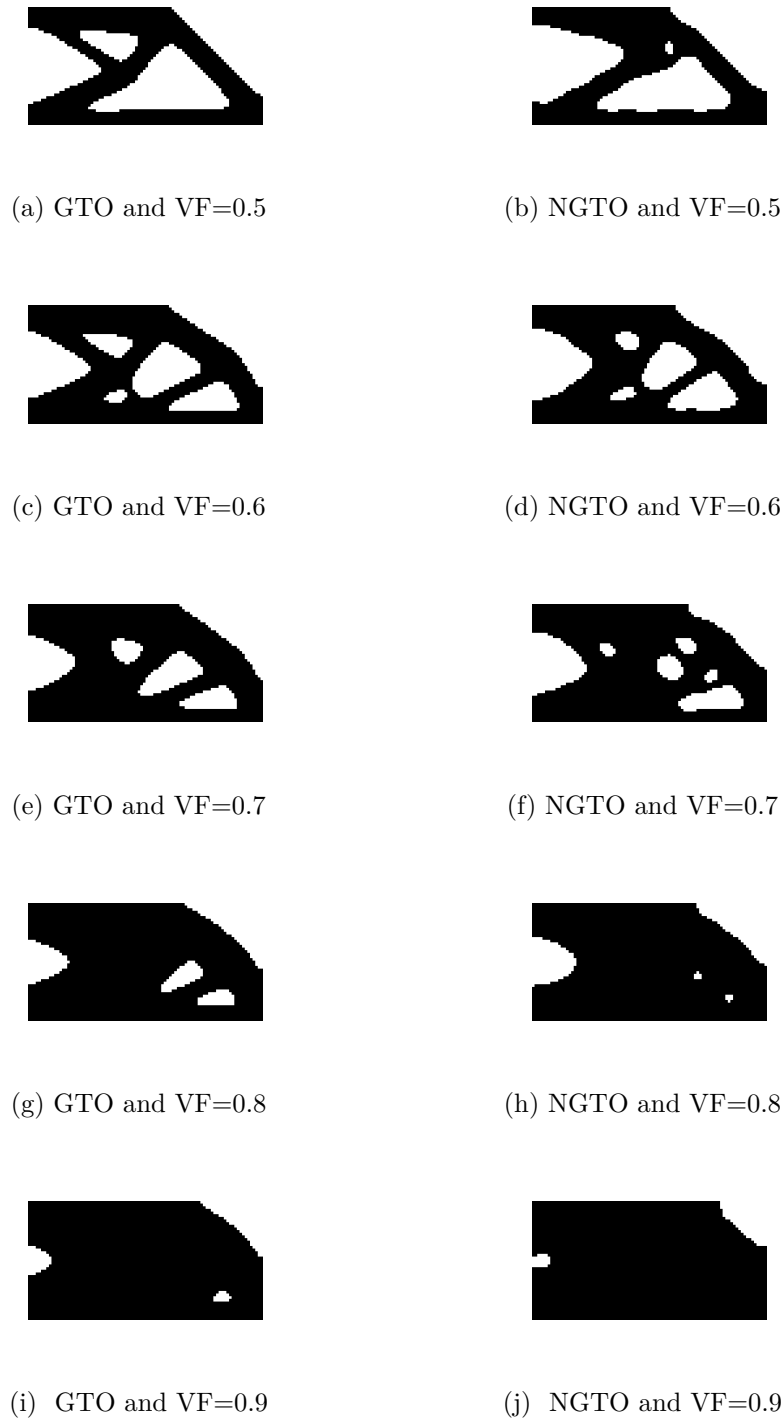


Figure 3.23 – Post-processed results of GTO and TO with SA in a cantilever beam problem with different volume fractions.

As shown in Fig. 3.23, post-processing with density filters can improve the results from TO by smoothing the boundaries and removing discontinuities. The values of compliance for the cantilever beam TO problem after the proposed post-processing are presented in Table 6.

Table 6 – Compliance (C) of optimized cantilever beam from the GTO in the literature and NGTO with SA after post-processing (PP).

VF	PP of GTO	PP of proposed NGTO
0.5	69.3000	72.4798
0.6	58.9102	59.7166
0.7	52.9039	52.9507
0.8	48.6857	48.3379
0.9	46.5597	46.3868

Table 6 shows improvement in the compliance of the cantilever beam after post-processing. It is mostly because of removing gray elements and smoothing the shapes. This post-processing method is not volume preserving. So, the results can not be compared directly to the results of TO. The post-processing algorithm can be used for the optimized topologies of the half-MBB beam at Fig. 3.15. The results for GTO and NGTO with SA are shown in Fig. 3.24 in different volume fractions.

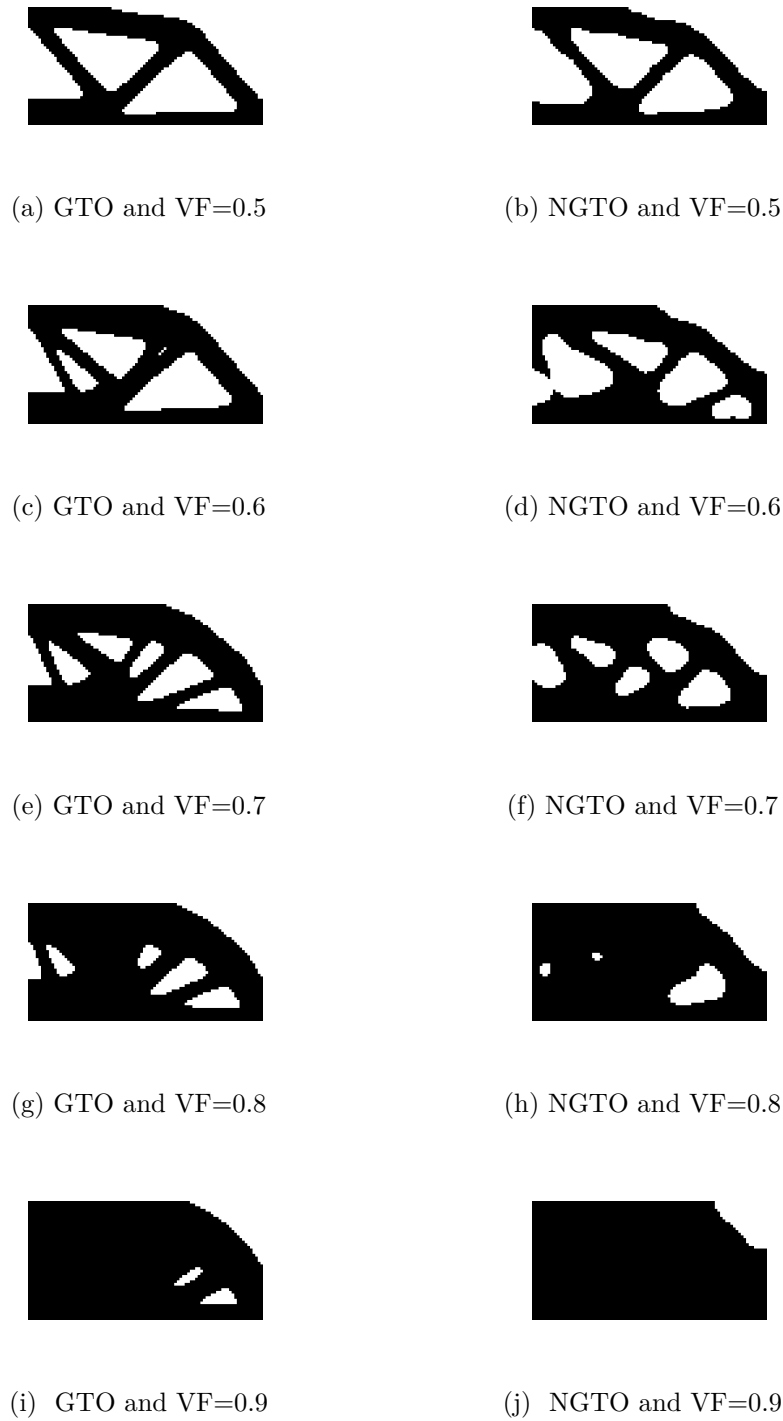


Figure 3.24 – Optimized topology of the half-MBB beam with GTO of reference and NGTO with SA after post-processing in different volume fractions.

Results of post-processing in Fig. 3.24 for a half-MBB optimized beam show improving the checkerboards, smoothing boundaries in NGTO, and removing gray areas. The values of compliance after post-processing of optimized half-MBB beam by GTO and NGTO with SA are presented in Table 7.

Table 7 – Compliance of optimized half-MBB beam from the GTO in the literature and NGTO with SA after post-processing (PP) in different volume fractions.

VF	PP of GTO	PP of proposed NGTO
0.5	79.4737	83.5807
0.6	67.7038	82.5454
0.7	60.1899	61.2962
0.8	54.6958	53.7438
0.9	51.3126	50.8605

Results in Table 7 and Fig. 3.24 show notable improvements in the shape and compliance of the optimized design after post-processing with density filters. But still, minimum feature sizes and thickness of elements are not applied in the design, which is important in manufacturing with micromachining. The post-processed shapes are used as a hard mask in surface micromachining to check the compatibility of the design with the final etched silicon. An example of the simulation for the cantilever beam is shown in Fig. 3.25 to show the effectiveness of post-processing with density filters.

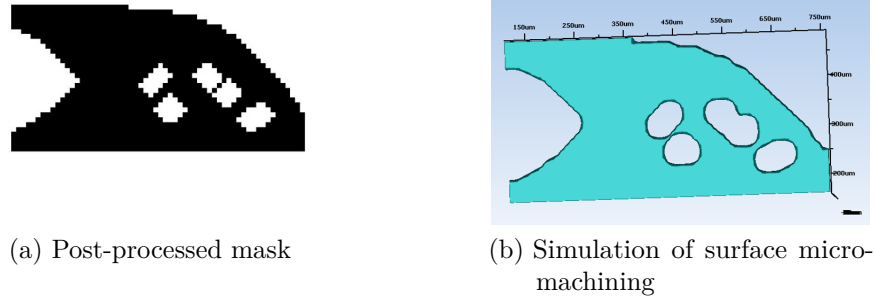


Figure 3.25 – Effect of post-processing by density filters on products of surface micromachining.

Fig. 3.25 shows that density filters can make smooth boundaries that are favorable in surface micromachining. A shape with a smooth boundary can be used as an etching mask in surface micromachining and the product is very similar to the initial mask. But the tiny elements are etched away in the etching of silicon and should be avoided in the design to have a final product equal to the mask and not lose any property or element due to the manufacturing by micromachining. Therefore, other post-processing strategies are required to have a more compatible design for micromachining. Application of a combination of morphological operators showed that they can be used in addition to the density filters for post-processing with consideration of microfabrication limits. Fig. 3.26 shows micro-machined results of an optimized topology for the cantilever beam

after post-processing with only density filters and post-processed with density filters and morphological operators.

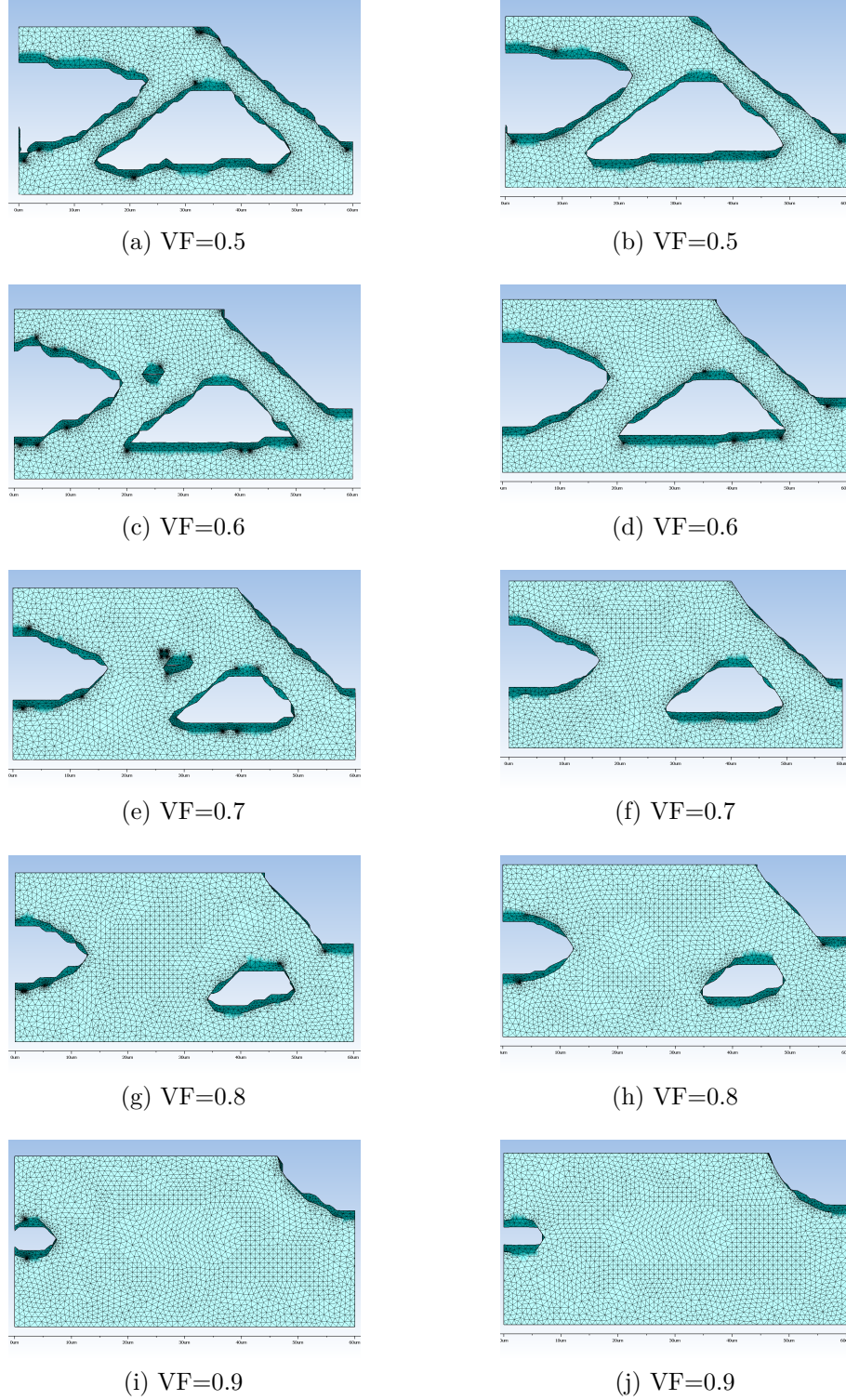


Figure 3.26 – Simulated etching for the optimized topologies of the cantilever beam with only density filters post-processing (left) and by adding morphological operators (right).

The results in Fig. 3.26 are obtained by using density filters and then performing a

close morphological operation. The close operator dilates topology with a disk structural element and then erodes it with the same structural element. The radius of the structural disk element can be selected as the minimum achievable size by micromachining, which is dependent on the process and thickness of the silicon wafer [114]. It can be concluded from Fig. 3.26 that using morphological operators make the mask more compatible with the etching process in micromachining and the results do not have any uncompleted etch hole or narrow elements discontinued in etching. The main advantage is to perform a design that is feasible for manufacturing with micromachining and modify it if necessary. It should be noted that post-processing with density filters and morphological operators can change the volume of the design by adding or removing elements. In the case that the volume is an important constraint in a TO problem, this post-processing method should be used carefully to keep the volume at the desired level. Post-processing also can change the design from the optimum point and in the case of changing very sensitive elements, it can change the results considerably. In the next section, another method will be proposed to work directly with TO for obtaining an optimized design without a need to post-processing and apply the connectivity constraints directly in the optimization process.

3.3 Binary Topology Optimization

Post-processing of the optimized topologies with gray areas is not always an efficient way to make the design feasible for manufacturing. The post-processing can change the volume or deviate the design from the optimum point. In a case where intermediate density helps improve the functionality of the structure, post-processing will remove the gray area and the design will totally change [115]. For example, in the case of maximizing compliance or minimizing the natural frequency of a structure, which is common in the design of sensors, the optimum solution will be a structure suspended by low-density elements. This area would be removed or changed significantly by post-processing and would be far from the optimum solution. In such cases, dealing with binary elements (solid or void) is more beneficial [116]. In the case of binary elements, checkerboards and singular elements are common problems, regardless of the convexity of the optimization problem. In both GTO and NGTO this problem leads to instability of the design and convergence to a design with checkerboards and tiny elements that are not possible to be fabricated with micromachining. Several methods are suggested in the literature to converge to a checkerboard-free solution [73]. In the case of NGTO, the application of density filters and generating solutions with continuity is more challenging. In this study, two strategies are adopted for NGTO with SA to have checkerboard-free and continuous solutions. The first strategy calculates the connection of elements to the other elements and adds it to the objective function. The connection of each element is a number assigned to that targeting element regarding the similarity of the neighboring elements by density. In a 2D design

domain as shown in Fig. 3.27, the targeting element ($x_{i,j}$) has up to 8 elements in the neighborhood. The connectivity number counts how many of the neighboring elements have equal density to the targeting element. Since in the borders of the design domain the neighboring elements are less than 8, the connectivity number is divided by the number of available neighbors. This number is between zero and one for each element. Subtraction of this number from one is called connectivity criteria.

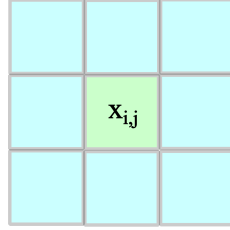


Figure 3.27 – A targeting element and neighbors in a 2D discretized domain.

The summation of the connectivity criteria is added to the objective function by a weighting coefficient. Minimizing the new objective function leads to minimizing elements with different densities in the neighborhoods and leads to a design with fewer checkerboards. The selection of the weighting coefficient depends on the number of elements in the design domain and the magnitude of the original objective function. Fig. 3.28 shows the application of this strategy in the binary TO with SA in a cantilever beam problem with a 0.5 volume fraction. It shows the solution of binary TO in minimizing compliance of the cantilever beam when no connectivity criteria are added to the objective function, when added with a small weighting coefficient, and when a proper weighting coefficient is added to the objective function.



(a) Binary TO with no connectivity criteria



(b) Added connectivity criteria to the objective function with a small weighting coefficient



(c) Added connectivity criteria to the objective function with a proper weighting coefficient

Figure 3.28 – Effect of adding connectivity criteria to the binary TO with SA.

Convergence of the new objective function to the optimum solution showed in Fig. 3.29 versus temperature in the SA algorithm.

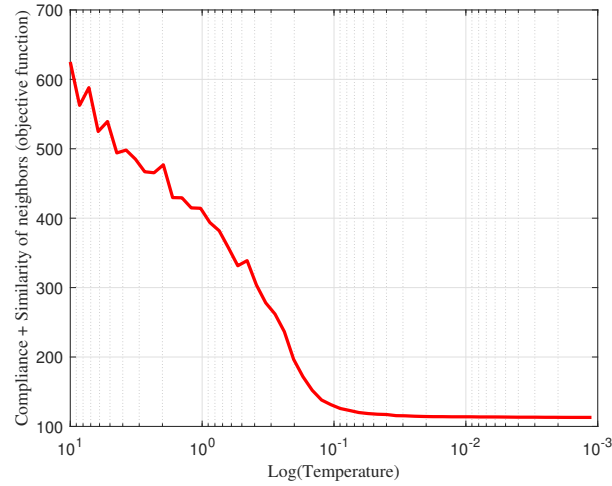


Figure 3.29 – Convergence of compliance and connectivity versus temperature in binary TO of cantilever beam with SA.

As shown in Fig. 3.29, the convergence of the new objective function including compliance and connectivity criteria is gradual as expected in an optimization problem with SA. The number of accepted and rejected solutions are also shown in Fig. 3.30. A higher number of iterations is used in this case due to the complexity of the optimization problem and some information from trial runs.

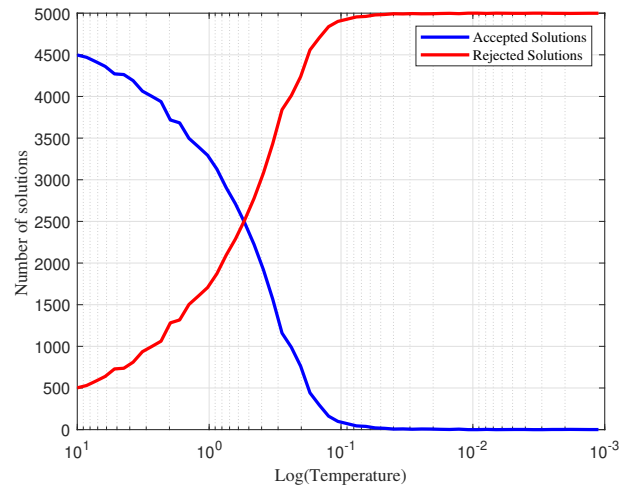


Figure 3.30 – Number of accepted and rejected solutions versus temperature for the objective of compliance and connectivity in binary TO with SA.

As shown in Fig. 3.30, the number of accepted solutions are decreasing during the optimization process. But the number of accepted solutions never reaches zero in this case because of changing some elements in the design domain which have no effect on the original objective function or the connectivity criteria number. So the energy level change in SA is zero and the new solution would be accepted by the SA acceptance rule. In this case, when the number of accepted solutions is small enough and not changing

considerably, the temperature can be selected as the freezing temperature to stop the optimization. The results showed that this connectivity criterion is very efficient to find the checkerboard-free optimum solution in a convex binary design domain. It also could be extended by increasing the number of neighboring elements to penalize structural elements with tiny thicknesses. The disadvantage of this strategy is the need for a high number of iterations. Since the newly generated solutions are favored to be connected to the rest of the structure, changes are limited and more iterations are required to sample the whole design domain. Also, the calculation of connectivity adds more computations to the algorithm. But the main disadvantage of this strategy is considering constraints as a soft limit and penalizing them to reach the optimum design. In the case of convex objective functions and flexible constraints, this algorithm can converge to an optimum solution. But in a TO problem such as maximizing the sensitivity of the accelerometer with the manufacturing constraint, the manufacturing limits should be considered as a hard limit. In this problem, disconnected elements can improve the objective functions by having infinite displacement but do not provide a feasible design. Therefore, generated solutions in each step of TO should be feasible for manufacturing. Adding constraints to the objective function and penalizing them does not provide valid designs for evaluation in TO. So, this method only can be used where invading manufacturing constraints will not change the feasibility of the design. The other strategy that is modified to be used in binary TO with SA is generating only connected solutions in any new solution. In this strategy, a new solution would be generated randomly by changing the location of one or a few random elements. Before the evaluation of the new solution by SA, the connection of elements to the rest of the structure is checked. To avoid the checkerboard, any element in the new solution must have at least two connected elements in the neighborhood, where the neighboring elements are defined as shown in Fig. 3.31.

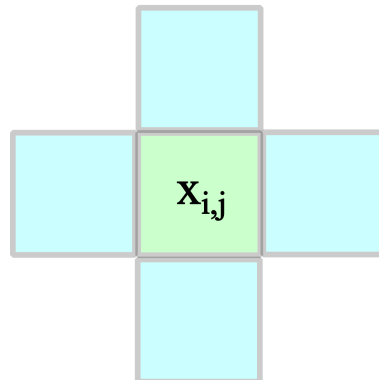


Figure 3.31 – Neighboring elements defined for the generation of connected solutions.

If the newly generated solution is not connected to two or more elements, it will not proceed to the evaluation by SA, and another solution would be generated randomly. While the new solutions have one or more disconnected elements, the process of random generation of the new solution will repeat. This ability to check the constraints as a

hard limit at any single step of TO is beneficial where invading a constraint changes the optimized design. The result of minimized compliance in a cantilever beam by binary TO with SA and this strategy is shown in Fig. 3.32.



Figure 3.32 – Results of binary TO with SA by checking connection in new solutions.

As shown in Fig. 3.32, this method shows a totally connected design without checkerboards or narrow elements. The main advantage of this method in comparison to adding connectivity criteria to the objective function is the ability to search only in the feasible design. Any set of constraints can be checked this way by the TO with SA and converge to a feasible solution [117]. In addition, this method does not need a very high number of iterations. The objective function converges to the optimum solution similar to the previous cases. If a new solution has disconnected elements, it will be ignored before FEA and entering the evaluation process of SA. This will make the computations faster than the previous case where all of the new solutions are evaluated by SA. The disadvantage here is needing fine meshes in the design domain. For a coarse mesh, there would be small spaces to be void and most of the domain should be solid. So the optimization algorithm does not have enough flexibility to search for the optimum solution. Fine meshes lead to a high number of elements and more computational costs. Therefore, a combination of these methods can be used depending on the TO problem. In this work, manufacturing constraints and other constraints are checked after the generation of a new solution and before the evaluation by SA. This strategy showed a very good performance for this type of TO and is discussed in the next section.

3.4 Concept design of the accelerometer

An out-of-plane capacitive MEMS structure is selected as the best fit for the low-g MEMS accelerometer application. The PolyMUMPs surface micromachining process has been selected based on its availability and similarity to CMOS process. The design domain is a structure that can be used for suspension of the proof mass and also a part of the proof mass. According to some trial runs, having an initial mass at the center helps convergence

to the optimum design. Fig. 3.33 shows the initial design domain containing a central proof mass, fixed boundaries, and changeable elements in between.

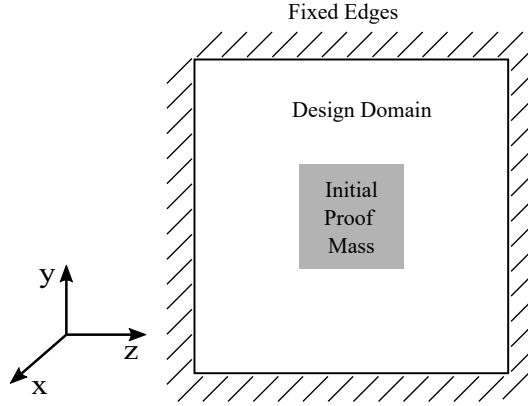


Figure 3.33 – The boundary condition, design domain, and initial proof mass.

The optimum design is a suspended mass as the movable electrode is moving out-of-plane and the capacitance between this electrode and a fixed electrode can be measured to determine the position of the proof mass. The design domain is considered symmetric with two symmetry lines in the y and z directions. The symmetric design makes the movements of proof mass more uniform. Then the measured data is more reliable, especially where lateral accelerations exist. The size of the initial design domain is selected based on the similar sensors in the literature and some trial runs to see the sensitive elements based on the limited displacement. Table 8 shows the dimensions of the design domain and the number of discretized elements. In addition, it contains parameters of the SA algorithm for efficient optimization from the analysis of the convergence and acceptance rate. The thickness of the structural layer and the initial air gap is from the PolyMUMPs process [101].

Table 8 – Dimensions of the design domain and parameters of SA for TO of out-of-plane MEMS accelerometer.

Parameter	Description	Value
T_{\max}	Initial temperature	1000
T_{\min}	Freezing temperature	0.001
α	Cooling schedule	0.9
$N_{\text{iteration}}$	Number of iterations in each temperature	1000
$N_y \times N_z$	Number of elements in the domain	40×40
$dy \times dz$	Size of each element in the design domain	$40 \times 40 \mu m^2$
t	Uniform thickness of the suspended structure	$1.5 \mu m$
d	Air gap between electrodes in zero accelerations	$2.75 \mu m$

The design includes the application of TO with SA for maximizing a desired performance

while several constraints are applied. The optimization process starts from an initial random solution and in each step of TO with SA, new solutions are generated and evaluated. Evaluation of the new solutions regarding objective function and constraints needs to simulate the behavior of the structure. The simulation has been done with a finite element analysis (FEA) to have an accurate calculation of static and dynamic behaviors. Kirchhoff quadrilateral plate elements with 4 nodes in each element and 4 degrees of freedom in each node are used in this study based on the physic of the problem. The Kirchhoff–Love plate theory assumes that the thickness of the plate is not changing during the deformation and straight lines normal to the mid-surface stay normal and straight after deformation. This theory models static out-of-plane displacement and dynamic vibration modes with high accuracy [118]. Figure 3.34 shows the process of TO in this design.

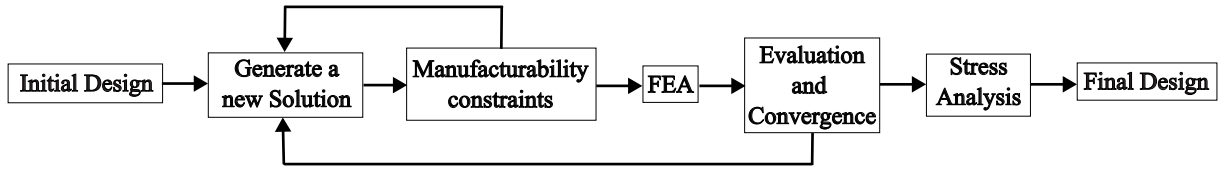


Figure 3.34 – flow chart of the topology optimization in the sensor problem.

3.5 Objective and constraints of Topology Optimization

The goal of using TO in this research is to maximize the sensitivity of the accelerometer and minimize cross-axis sensitivity while considering constraints from microfabrication and physical limits. Selection of the objective the proper objective function and constraints have an important effect on the convergence to optimum design. In the design of this sensor, some constraints and objective functions are conflicting and could cause it to get stuck in local optima. In such situations, information of objective function and acceptance ratio of new solutions can be analyzed for investigation of the convergence to a global optimum. The maximization of sensitivity is proportional to the maximum change of capacitance between two electrodes after applying inertial loading. According to Eq.(2.4), it is dependent on the displacement of the moving electrode for constant external acceleration. A larger surface area also provides stronger signals that are easier to measure. But the pull-in voltage in Eq. (2.5) should be avoided. The force that causes displacement in the moving electrode comes directly from the inertial force according to Eq. (2.1). In similar TO methods, the proof mass is constant and consequently, a constant inertial force is applied to the structure. The proposed TO method with SA in this research gives this ability to consider the inertial load as a variable and local force. After the generation of a new solution, the force is recalculated in the new topology and it is used to find the displacement of the structure. So adding or removing an element changes the surface area between electrodes, stiffness matrix, and inertial force (location and magnitude). Then the new topology is evaluated by the SA criteria to find the optimum

design. The process should also satisfy several constraints including maximum stress limit, dynamic behavior by natural frequencies and vibration modes, and micromachining limits. A combination of these objectives and constraints can lead to an optimum design, and depending on the application, each of them can be desired. In this section, different objectives and constraints are optimized by the proposed TO with SA. The results are analyzed for efficiency of optimization and applicability of a combination of objectives and constraints. The transfer function for Eq.(2.2) can be written by defining the natural frequency ($F_n = \sqrt{K_m/m}$) and damping ratio ($\zeta = b/2\sqrt{K_m m}$).

$$H(s) = \frac{X(s)}{A(s)} = \frac{m}{ms^2 + bs + K_m} = \frac{1}{s^2 + 2\zeta\omega_n s + \omega_n^2} \quad (3.11)$$

According to Eq.(3.11) reducing natural frequencies in a vibration mode is proportional to increasing movements in that mode. For a sinusoidal external acceleration with a magnitude of a_0 and frequency of ω , the steady-state deflection would be sinusoidal with the same frequency and a phase shift of ϕ . The magnitude of steady-state deflection can be calculated using Eq. (3.12).

$$X_0(\omega) = \frac{a_0}{\omega_n^2 \sqrt{[(\frac{\omega}{\omega_n})^2 - 1]^2 + 4\zeta^2(\frac{\omega}{\omega_n})^2}} \quad (3.12)$$

The first case of TO has an objective function of minimizing the first natural frequency. The first natural frequency has a vibration mode in the direction of out-of-plane motion. So decreasing the first natural frequency is proportional to increasing the displacement of the mass and sensitivity. Three constraints are applied to this TO case. The first constraint is the connectivity of each element to at least two neighboring elements, including a connection by one node. This is a very important constraint regarding the manufacturability of the optimized design. As discussed in the previous section, this constraint is applied before evaluation by SA and if it invades manufacturing constraints, another solution would be generated. The second constraint is the ratio of second to first natural frequency to be more than two. This constraint keeps the second and first vibration modes far away and does not let the mode switch happen or add local modes in the solution. Additionally, it helps to reduce the sensitivity of the motion in the principal direction of motion (out-of-plane) to the lateral or rotational accelerations. This constraint is very important to guide the optimization process and was selected after several trial runs with unsuccessful convergence. The third constraint is the maximum out-of-plane displacement in each element to be less than one-third of the initial gap between electrodes in $1g$ of acceleration. This constraint is applied to prevent a breakdown of the capacitor. The result of the TO for this case is shown in Fig. 3.35.

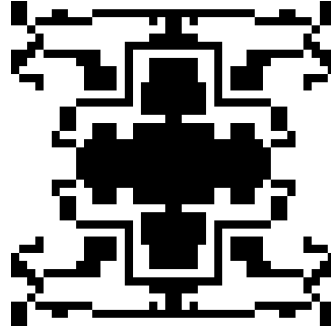


Figure 3.35 – Optimized topology of the sensor for minimizing the first natural frequency and constraints on the ratio of frequencies, connectivity, and maximum displacement in a trial run.

As shown in Fig. 3.35, the initial central mass is suspended by a combination of folded beams. The minimizing first natural frequency is selected in this case because it is proportional to the maximizing displacements of the proof mass. Since there is no volume fraction constraint in this optimization, it is possible to accept some solutions with the same objective function and with some added or removed elements in the borders. The extra solid elements in Fig. 3.35 with no effective connection to the proof mass or the suspension structure are obtained because of this effect, but they can be removed by post-processing without any change in the optimized objective function. Fig. 3.36 shows the number of accepted and rejected solutions versus temperature to analyze convergence to the optimum solution.

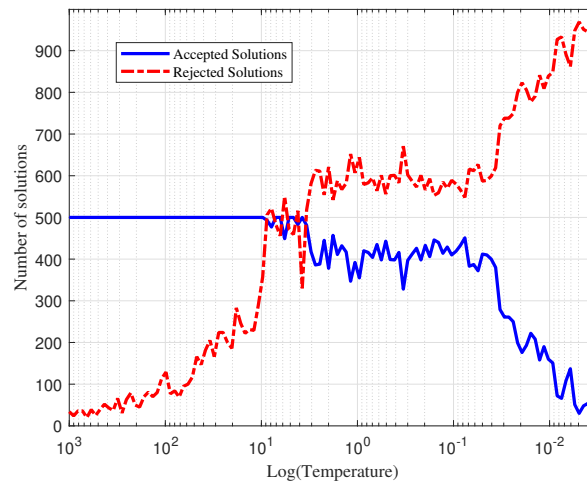


Figure 3.36 – Number of accepted and rejected solutions in minimizing first natural frequency and constraints on the ratio of frequencies, connectivity, and maximum displacement in a trial run.

As shown in Fig. 3.36, the number of rejected solutions increases gradually with temperature till reaching the optimum solution. It shows that the optimum solution is

an optimum point in the neighborhood and it is not near a singular point. As a rule of thumb in optimization with SA, if the number of accepted solutions is more than half of the number of iterations, it is possible to decrease the temperature without changing the performance of optimization [90]. This is applied in this study to decrease computational costs if in case the initial temperature is selected higher than necessary or the number of accepted solutions is decreasing slowly. The objective function in this case, which is minimizing the first natural frequency, converges to the optimum solution as shown in Fig. 3.37 versus temperature.

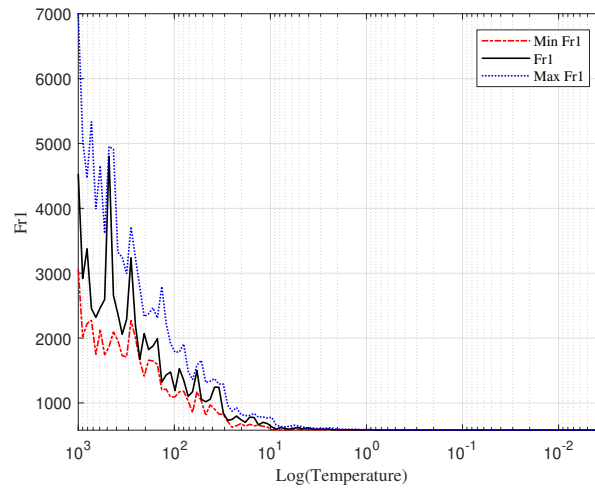


Figure 3.37 – Convergence of objective function versus temperature in minimizing first natural frequency and constraints on the ratio of frequencies, connectivity, and maximum displacement in a trial run.

According to Fig. 3.37, the first natural frequency reaches the optimum point rapidly in high temperatures and after that, it is not improving significantly. It means the solution is improving very slowly near the optimum point. The maximum and minimum values of the objective functions are also presented here to show the deviation of solutions but they present almost the same information as the number of accepted and rejected solutions. The effect of minimizing the first natural frequency on the sensitivity is shown in Fig. 3.38 by sensitivity representative versus temperature. It is not the actual value of sensitivity but it is the summation of out-of-plane displacement of all solid elements in the domain.

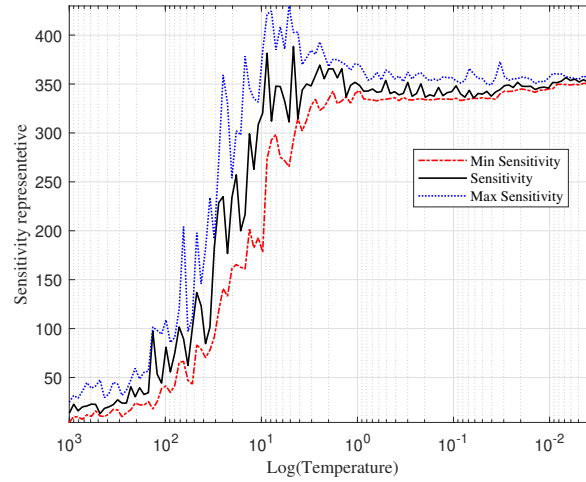


Figure 3.38 – Change of sensitivity in minimizing first natural frequency and constraints on the ratio of frequencies, connectivity, and maximum displacement in a trial run.

Fig. 3.38 shows the sensitivity is not increasing permanently in the optimization. The reason is the effect of inertial force and surface area of the proof mass on sensitivity. Increasing the proof mass is desired for decreasing the natural frequency and also increasing the inertial force. But it is limited by the maximum displacement. It also affects the surface area which is important in increasing the capacitance between electrodes [119].

Another case of trial run is maximizing the sensitivity while the same constraints of the previous case are applied. The ratio of the second to first natural frequency kept more than two, the maximum out-of-plane displacement is less than one-third of the air gap, and each element should be connected at least to two other elements. The results from TO are shown in Fig. 3.39.

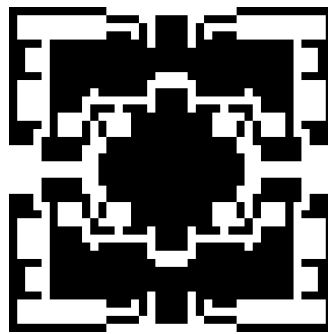


Figure 3.39 – Results of TO for maximizing sensitivity and constraints on the ratio of frequencies, connectivity, and maximum displacement in a trial run.

The optimized topology in Fig. 3.39 shows that some extra masses are connected to the fixed boundary around the design domain. These elements have no effect on the objective function and are accepted due to zero energy level change in the SA optimization algorithm.

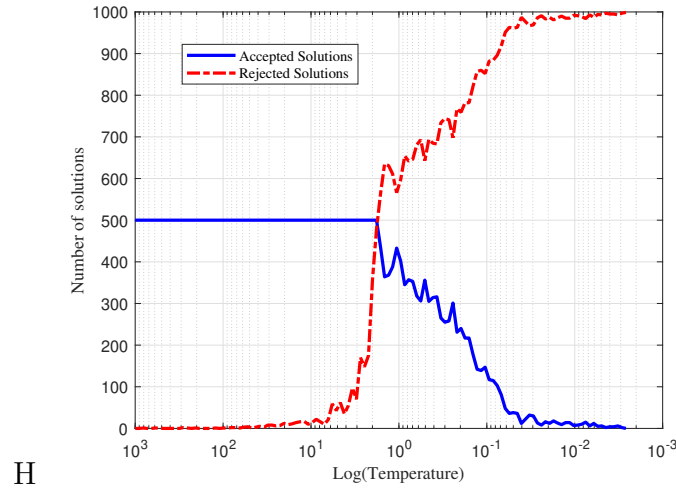


Figure 3.40 – Accepted and rejected solutions for maximizing sensitivity and constraints on the ratio of frequencies, connectivity, and maximum displacement in a trial run.

There are also some masses that are not a part of the effective suspension structure but are in this shape by increasing the surface area of electrodes and improving the objective function. More solid elements in this region would give more sensitivity but the limit on the maximum displacement stops it. It should be noted that increasing the surface area of the electrode increases the capacitance of the sensor. But sensitivity is actually proportional to the change of this capacitance when acceleration is applied. So, a better representative of sensitivity can be the change of capacitance before and after applying acceleration. The results of these trial TO problems can lead to such improvements in the next optimizations. Fig. 3.40 shows the number of accepted and rejected solutions in the TO process of this case.

The number of accepted and rejected solutions in Fig. 3.40 shows that the solution is gradually converging to a solution and enough search has been done in high temperatures. This graph is important to make sure that maximum and minimum temperatures are selected reasonably. The convergence of sensitivity as the objective function versus temperature is shown in Fig. 3.41.

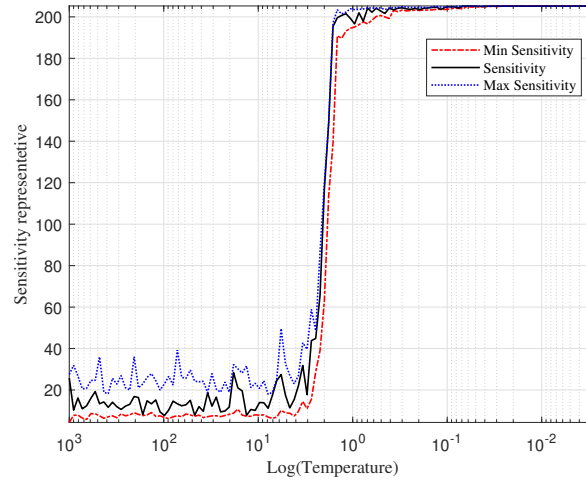


Figure 3.41 – Sensitivity versus temperature for maximizing sensitivity and constraints on the ratio of frequencies, connectivity, and maximum displacement in a trial run.

As shown in Fig. 3.41, the objective function changes rapidly to a higher value and stays there as the optimum point. It can be concluded from this graph that the objective function can have other options to reach solutions with different configurations and similar objectives. The sensitivity would be increased in this design by increasing the proof mass and reducing the stiffness of the suspension structure and it can be continued to reach infinite values. But the constraint in maximum displacement stops the optimization process. Depending on the value of this constraint, several of the resultant structure can have various shapes with the same objective function value. Since it can be more than one solution, the point is not a unique optimum but is a solution by the best possible performance with these constraints. Repeating this TO process can give solutions with similar performance parameters but different shapes. The generative designs can be analyzed for other limits such as manufacturing or maximum stress to select a feasible design for manufacturing. Changes in the first natural frequency versus temperature shown in Fig. 3.42 demonstrate the same behavior in frequency. It changes rapidly and reaches a solution and stays there with no more improvements.

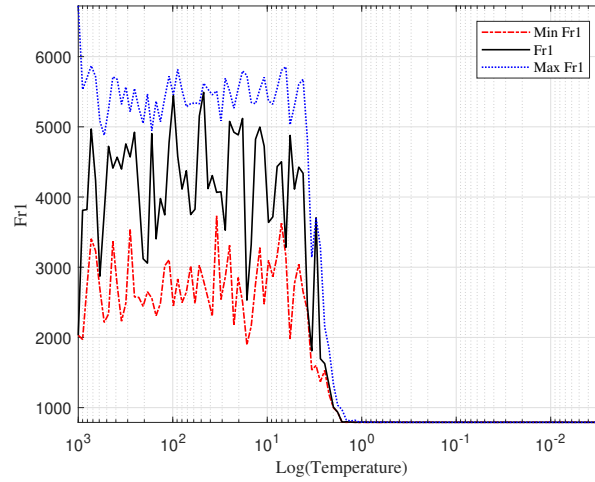


Figure 3.42 – First natural frequency for maximizing sensitivity and constraints on the ratio of frequencies, connectivity, and maximum displacement in a trial run.

The next case of the trial run is maximizing sensitivity with the same constraints. This problem is completely similar to the previous case and it is used to see other alternative solutions. Fig. 3.43 shows the results for this optimization problem.

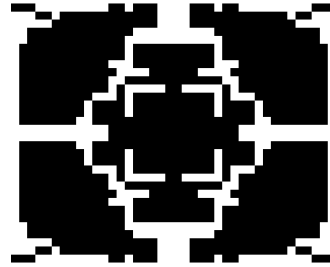


Figure 3.43 – Results of TO for maximizing sensitivity and constraints on the ratio of frequencies, connectivity, and maximum displacement in the second trial run.

The results of TO in Fig. 3.43 show a shape different from Fig. 3.39 while they have the same objective functions and constraints. But the values of the objective function and natural frequencies are very close in both results. This is because of not uniqueness of the solution and stopped optimization by the constraint on the displacement. Without a constraint on the displacement, the objective function goes to infinity without converging to any solution. Fig. 3.44 shows the number of accepted and rejected solutions for this case in each temperature.

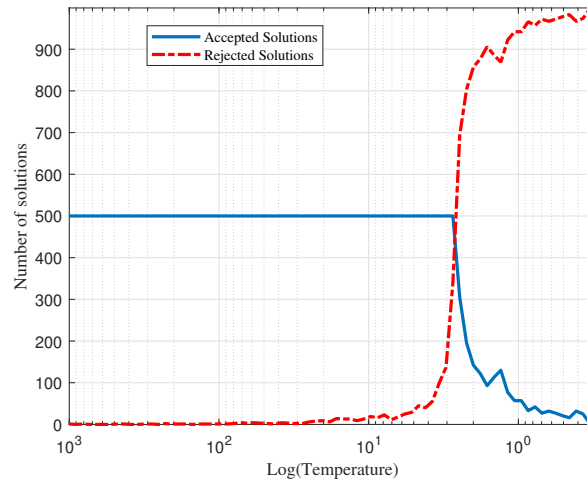


Figure 3.44 – Number of accepted and rejected solutions versus temperature for maximizing sensitivity and constraints on the ratio of frequencies, connectivity, and maximum displacement in the second trial run.

The number of accepted and rejected solutions in Fig. 3.44 shows that the algorithm stays in a random walk situation and explores the domain for many solutions and then reaches the equilibrium point. That means the maximum temperature is higher than necessary and can be selected around a hundred. It also shows enough solutions were accepted to sample the whole domain and the domain is searched properly. The convergence of sensitivity is shown in Fig. 3.45 versus temperature.

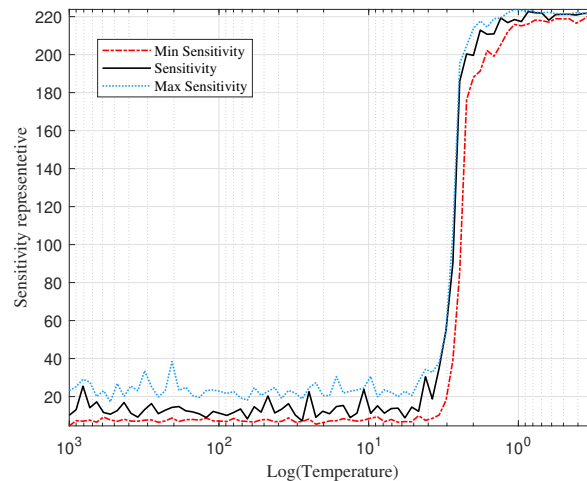


Figure 3.45 – Sensitivity versus temperature for maximizing sensitivity and constraints on the ratio of frequencies, connectivity, and maximum displacement in the second trial run.

Fig. 3.45 shows a rapid convergence to the final solution which is similar to Fig. 3.41. It can be interpreted as this solution is not unique and different solutions can be reached in this problem, but they have similar sensitivity and natural frequencies. Fig. 3.46 shows the behavior of the first natural frequency.

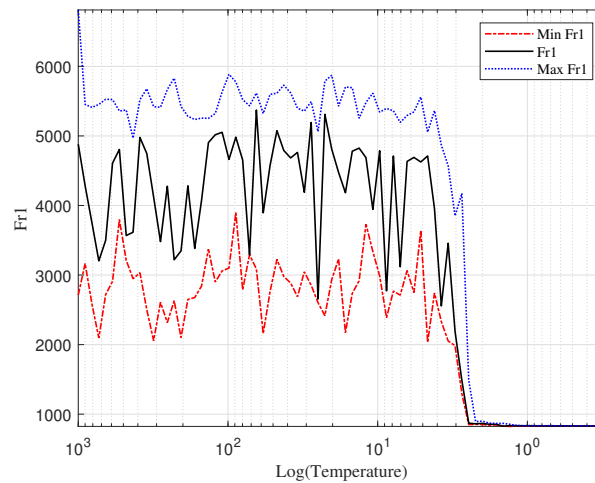


Figure 3.46 – First natural frequency for maximizing sensitivity and constraints on the ratio of frequencies, connectivity, and maximum displacement in the second trial run.

The first natural frequency in Fig. 3.46 reaches rapidly to a small value during the optimization process. It is similar to the behavior of the objective function (maximizing sensitivity) and shows that this is not a unique solution. The objective functions and constraints for trial runs are selected based on the investigation of many possible situations and analysis of behavior. For example, the constraint of putting the ratio of second to the first natural frequency more than two is important to make the design more stable and less sensitive to lateral accelerations. Fig. 3.47 shows the result of TO for the same problem of maximizing sensitivity. In this case, only connectivity and maximum out-of-plane displacement are applied as constraints.

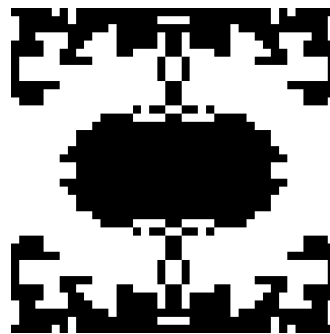


Figure 3.47 – Results of maximizing sensitivity with the constraint on connectivity and maximum out-of-plane displacement.

Fig. 3.47 shows that releasing the constraint on the ratio of the second to first natural frequency can get a more flexible design but is very sensitive to the lateral accelerations and rotations. In this case, the first natural frequency has more freedom to be decreased but the second natural frequency would be very close to it. The maximum out-of-plane

displacement and connectivity constraints can be replaced by a constraint on the minimum first natural frequency. Fig. 3.48 shows the results of TO for minimizing the ratio of the first natural frequency to the average of six first natural frequencies. The only constraint in this problem is that the first natural frequency cannot be smaller than $4000Hz$.



Figure 3.48 – Results of minimizing ratio of first natural frequency to the average of six first natural frequencies and constraint on a minimum of first natural frequency.

As shown in Fig. 3.48, the resultant structure is supported properly to avoid lateral movements. The minimum first natural frequency constraint also helps to avoid disconnected elements or any large displacement.

After trying several combinations of objectives and constraints in the TO problem such as the examples mentioned above, three problems are selected for good convergence and ability to reach the desired performance. The first design (D1) made with TO is with the objective of maximizing sensitivity. Constraints are the ratio of second to the first natural frequency more than two ($F_2/F_1 > 2$), connectivity constraint (CC), and maximum displacement of each element less than one-third of the initial gaps between electrodes when applying $1g$ of acceleration. The optimization process starts with a random initial solution in the design domain and with parameters mentioned in Table 8. In each iteration, a new solution is generated by the selection of a random element in one-quarter of the domain and changing the density of that element and its neighboring elements. This new solution would be replicated in the other quarters to have a fully symmetric design. Then the FEA calculates the static and dynamic behavior of the new solution. If all of the constraints for maximum displacements, the ratio of the second to the first natural frequency, and connectivity are satisfied, the new solution goes to the next step in the SA algorithm. Otherwise, it would be ignored and another random solution is generated. This process continues till finding a new solution that satisfies all of the constraints. It should be noted that if the constraints are imposing too many limits on the new solution, the TO process spends a long time generating a new solution. So it would be with high computational costs. After evaluation of enough solutions in SA, the temperate is reduced with the cooling factor and this process continues till reaching the

minimum temperature or no accepted solutions in a temperature. Similar TO problems for maximizing sensitivity in Fig. 3.39 and Fig. 3.43 showed that the displacement of solid elements is more important in the sensitivity. So here the objective function is calculated by summation of sensitivity for each element, which is the displacement times density of each element at the center. So it neglects the effect of elements near the fixed boundaries and removed unusable elements in that region. The results of TO for this problem are shown in Fig. 3.49.

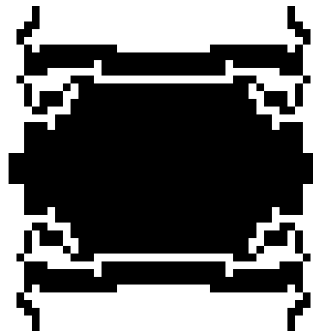


Figure 3.49 – Optimized topology for maximizing sensitivity and constraint on connectivity, maximum displacement, and the ratio of second to first natural frequencies (D1).

As shown in Fig. 3.49, there are some elements that are connected just by one node. That is due to using coarse meshes to reduce computational costs. Instead of increasing the number of elements, the post-processing method proposed earlier in this study is applied to this design to reach a design manufacturable by the micromachining process. The post-processed design is shown in Fig. 3.50.

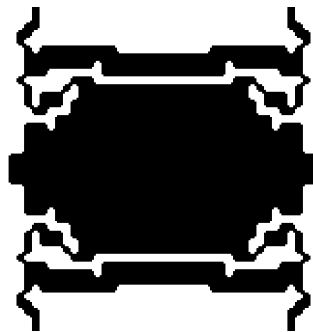


Figure 3.50 – Post-processed design for maximizing sensitivity and constraints on the maximum out-of-plane displacement, connectivity, and ratio of natural frequencies (D1).

The design in Fig. 3.50 shows that the proof mass is concentrated mostly in one part and the displacement of this part as an electrode changes the capacitance. To analyze the

convergence information for this problem, the number of accepted and rejected solutions is shown versus temperature in Fig. 3.51.

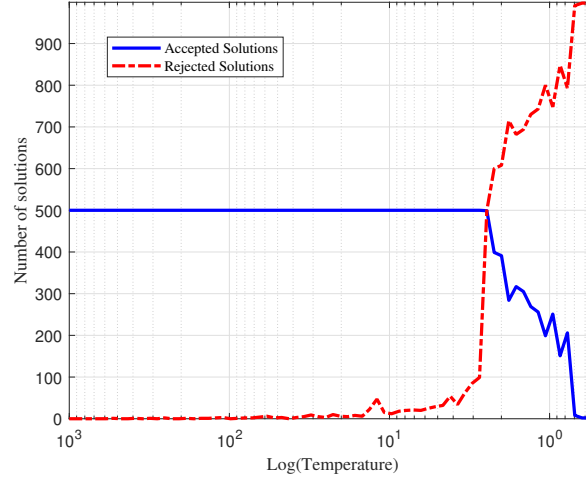


Figure 3.51 – Number of accepted and rejected solutions in each temperature for TO with SA in design (D1).

As shown in Fig. 3.51, rejected solutions increase almost gradually and reach the point that all of the iterations get rejected. It shows that enough samples were investigated at higher temperatures and before the convergence. From the design domain and the physic of the problem, this problem does not have a unique solution but the TO with SA finds the maximum possible performance with the imposed constraints. The convergence of sensitivity in this problem versus temperature is shown in Fig. 3.52.

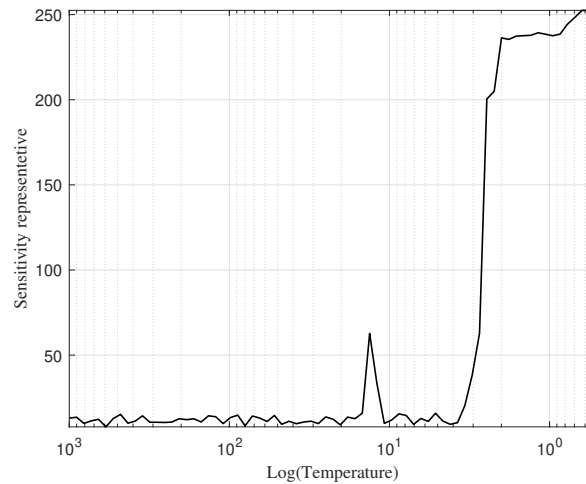


Figure 3.52 – Convergence of sensitivity in TO with SA in design (D1).

According to the convergence graph in Fig. 3.52, the objective function (sensitivity) is converging to the maximum value slower than the other cases in Fig. 3.41 and Fig. 3.45. So, it can be concluded that limiting the sensitivity calculations to the central elements and neglecting the elements near the boundary for the objective function can improve the

search in this problem. The static and dynamic behaviors in this design are first compared with other optimized designs in Table 9. Then, the performance properties are compared with designs in the literature.

The second design (D2) is performed with TO for minimizing the first natural frequency (F1). The connectivity constraint (CC), the maximum displacement of less than one-third of the initial gap, and a constraint on the ratio of the second to the first natural frequency to be more than two ($F2/F1 > 2$) are applied to this design. From the trial runs, the result for this problem is a flexible structure but it does not have many solid elements to increase the capacitance and sensitivity. The design from TO with SA is shown in Fig. 3.53.

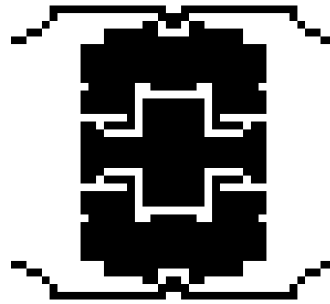


Figure 3.53 – Results of TO for minimizing the first natural frequency and constraints on connectivity, maximum displacement, and the ratio of second to first natural frequencies.

The topology in Fig. 3.53 is a flexible structure in the out-of-plane direction (principal vibration mode) while satisfying all of the constraints. The constraint of maximum out-of-plane displacement and frequency ratio determine the optimum solution herein. Similar to the previous case, coarse mesh causes one-node connections and needs to be post-processing for micromachining and stress analysis. The post-processed topology for design D2 is presented in Fig. 3.54.

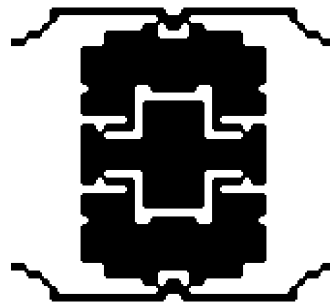


Figure 3.54 – Post-processed results of TO with SA for minimized first natural frequency and constraints on connectivity, maximum out-of-plane displacement, and the ratio of natural frequencies (D2).

To check the optimization process and convergence, Fig. 3.55 shows the number of accepted and rejected solutions versus temperature.

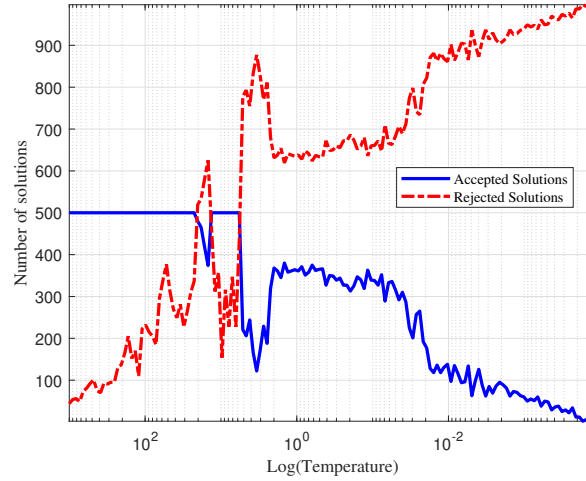


Figure 3.55 – Number of accepted and rejected solutions for design (D2).

The number of accepted and rejected solutions in Fig. 3.55 for design D2 shows a good exploration and enough sampling at high temperatures and reaching the optimum point gradually. This solution is reached by sampling enough solutions in the design domain and is an optimum point, even if it is not necessarily unique (due to the type of problem and physic behind it). Convergence of the objective function (minimizing first natural frequency) is shown in Fig. 3.56 for design D2.

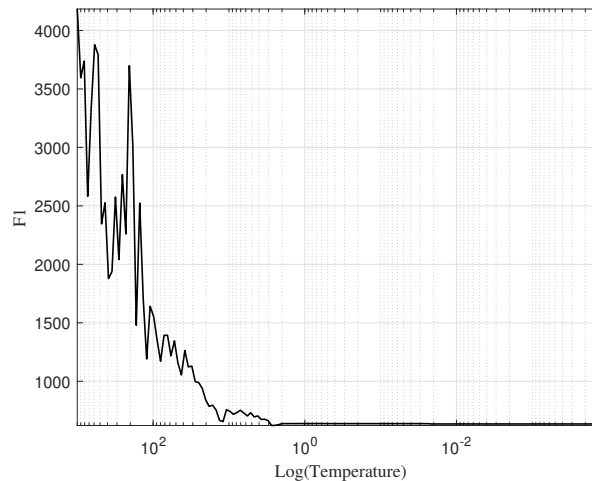


Figure 3.56 – Convergence of minimizing the first natural frequency in Design (D2).

As shown in Fig. 3.56, the objective function converges to the final value with some oscillations and stays constant at the end. It shows that the objective function is not changing significantly after a temperature. The few accepted solutions after this temperature are with small or no improvement in the objective function. So the freezing

temperature (minimum temperature) can be selected in a higher value. The third design (D3) is performed with TO for maximizing the ratio of the second to the first natural frequency. The constraints are keeping the maximum out-of-plane displacement less than one-third of the initial gap and connectivity constraint. But since the maximization of this ratio converges to a stiff structure, the maximum displacement constraint is not active near the optimum solution. But it is useful to add this constraint to avoid any singularity in the calculation and prevent getting local modes with a very small first natural frequency. The design obtained from TO is shown in Fig. 3.57.

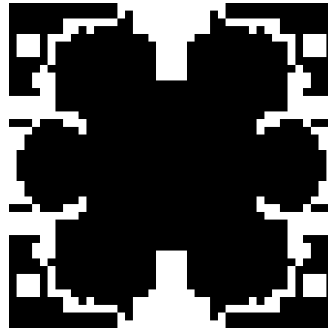


Figure 3.57 – Optimized topology for maximizing the ratio of the second to the first natural frequency with constraints on maximum displacement and connectivity (D3)

The optimized topology in Fig. 3.57 has some one-node connections due to the coarse mesh. Similar to the previous designs, the post-processing method presented in this study can elaborate the design and make it feasible for micromachining as well as suitable for stress analysis. The post-processed design of D3 is shown in Fig. 3.58.

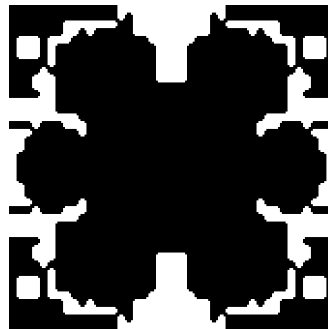


Figure 3.58 – Post-processed topology of design (D3).

The post-processed design in Fig. 3.58 can be used for a more accurate FEA. The optimization process with SA can be analyzed by checking the convergence information. The number of accepted and rejected solutions in each temperature is shown in Fig. 3.59.

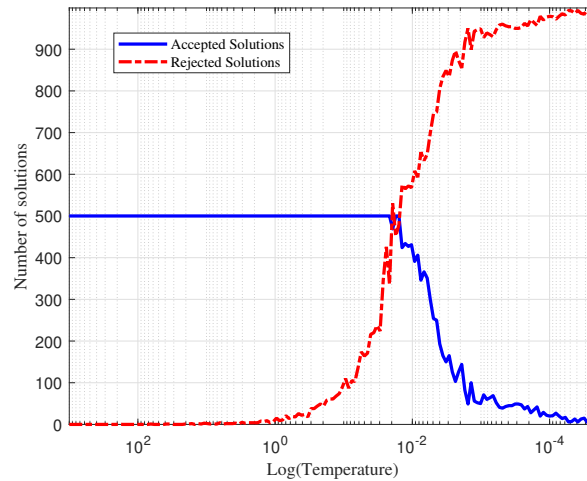


Figure 3.59 – Number of accepted and rejected solutions in each temperature for D3.

The number of accepted and rejected solutions in Fig. 3.59 shows enough exploration in the domain in high temperature. Then the number of rejected solutions gradually increases till all solutions get rejection. So enough explorations and refinement are done in the SA to reach the optimum solution. Convergence of the objective function during the TO with SA is shown in Fig. 3.60.

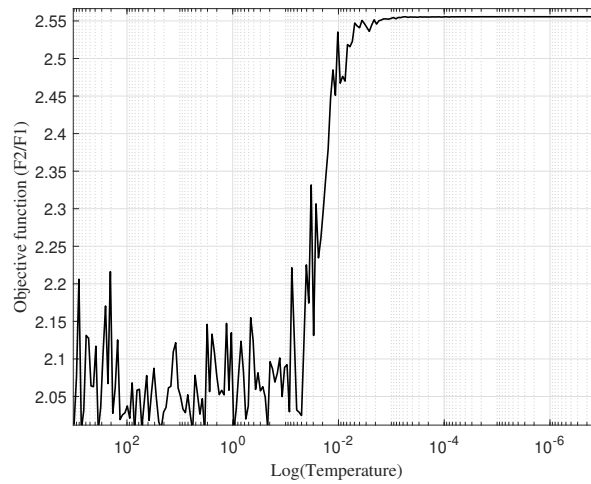


Figure 3.60 – Convergence of the objective function (ratio of second to first natural frequency) to the optimum solution for design (D3).

The ratio of second to first natural frequency increases with some oscillations as shown in Fig. 3.60. It can be concluded from this graph that the optimum point is reached for this optimization and imposed constraints. A comparison between the three designed structures has been shown in Table 9 from the dynamic and static behaviors point of view.

Table 9 – Design specifications of the optimized structures.

Parameter/Design	D1	D2	D3
Objective	Max S	Min F1	Max F2/F1
F1 (Hz)	896.65	618.43	3594.30
F2 (Hz)	1794.41	1234.55	9172.88
F3 (Hz)	1865.81	1347.68	9176.48
F4 (Hz)	3114.60	2270.37	14765.40
F5 (Hz)	3341.11	4083.26	15683.71
Max Ux (μm)	0.4090	0.5709	0.1157

Table 9 shows the first five natural frequencies(F1-F5) and maximum out-of-plane displacement (Ux) for each design. The results show that for designs D1 and D2, the ratio of second to first natural frequency works as an active constraint. The connectivity constraint is only preventing the disconnected elements and helps to get reasonable results without numerical instabilities. The constraint on the maximum allowable out-of-plane displacement is not reached with other constraints in non of the designs, but it prevents acceptance of alternative solutions with very low stiffness suspension. A sensitivity representative is a number calculated for each design based on the displacement and density of its element. To have a better comparison of sensitivity, the actual sensitivity is calculated for each design and some similar reference designs in the next section.

3.6 Verification of Performance

To verify the performance of the presented designs, first, a static FEA was performed to calculate stress and displacement in each design and compared with allowable values. Then a dynamic analysis was performed to show the first five mode shapes and compared them in each design. Since the structural material is polysilicon, the mechanical properties of silicon are used in the FE as shown in Table 10.

Table 10 – Mechanical properties of Silicon as the structural material.

Property	Symbol	Value	Unit
Elastic modulus	E	1.124^{14}	N/m^2
Poisson's ratio	ν	0.28	-
Shear modulus	G	4.9×10^{10}	N/m^2
Mass density	ρ	2330	Kg/m^3
Yield strength	σ_y	1.2×10^8	N/m^2

For design D1, the structure is fixed at the boundaries of design, and gravitational acceleration of $1g$ is applied in the out-of-plane direction. The structure meshed with solid standard mesh, 16 Jacobian points, and 23.42 microns of the element size. A total of 19865 elements and 42728 nodes are used to mesh this structure with a tolerance of 1.17 microns. The mesh is shown in Fig. 3.61.

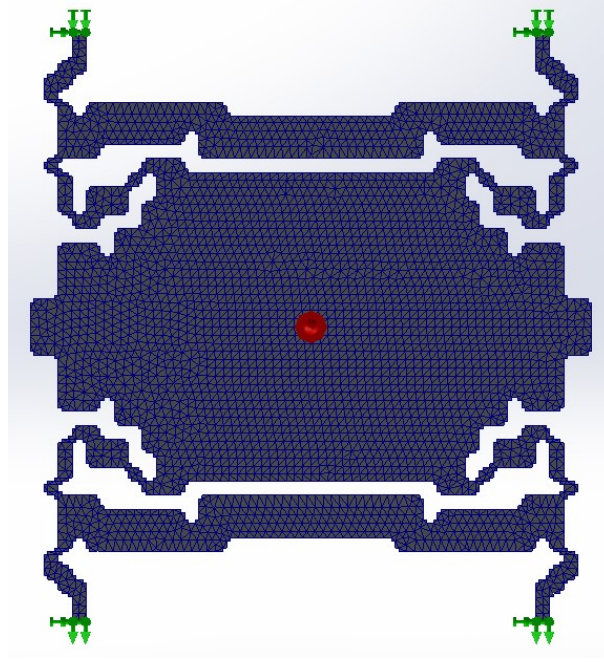


Figure 3.61 – Mesh for FEA of design (D1).

The static FEA was used to calculate the total displacement of the structure for $1g$ of external out-of-plane acceleration and the results showed in Fig. 3.62.

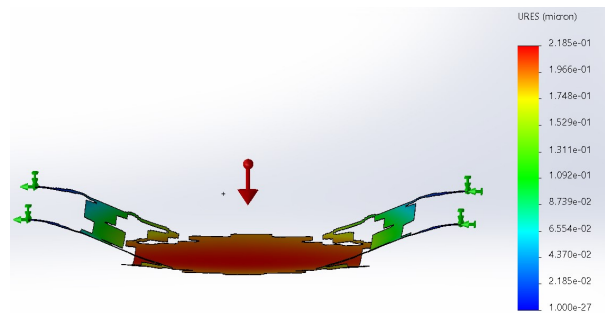


Figure 3.62 – Total displacement in design (D1) from FE simulation with a scale of 1000.

As shown in Fig. 3.62, the displacement of the proof mass is almost uniform. The maximum displacement occurs in the whole proof mass as a movable electrode in the capacitive sensor and will present the maximum possible change in the capacitance. This is due to selecting proper constraints and objectives, especially the constraint on the ratio of second to the first natural frequency. The maximum total displacement of 0.2185 microns is in the middle of the structure. This is slightly different from the results in the initial

simulations before post-processing. But it still remains near the optimum solution and has the specifications required in the design. Because of this difference, the results after post-processing are used in the simulations to calculate the performance parameters and compared to the designs in the literature. The simulation results for Von Mises stress are shown in Fig. 3.63 to check the maximum stress in $1g = 9.81m/s^2$ of acceleration.

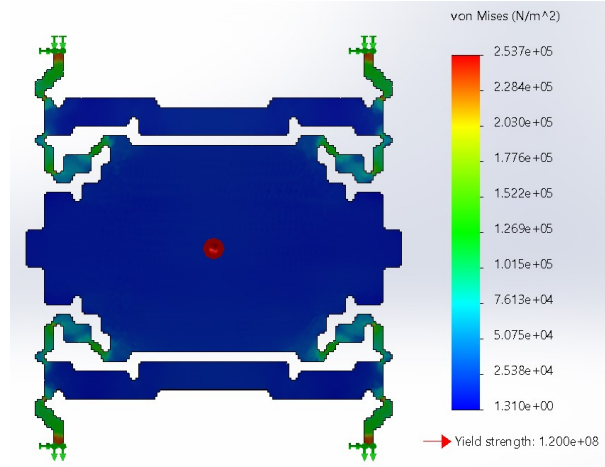


Figure 3.63 – Von Mises stress in design (D1) by applying $1g$ of inertial acceleration.

The maximum stress of 253.7 KPa is calculated in some regions which is much smaller than the yield stress of silicon (1200 KPa). It gives a safety margin to the design for uncertainties in the manufacturing process. Also, it increases the fatigue life for the structure in the cyclic loading. In addition, the etching process by itself removes sharp edges which results in more resistance to initiate cracks and fatigue failure. According to Alsem [120], the fatigue lifetime of polysilicon thin film structures is more than 10^{11} cycles when the maximum stress is in 70% of the fracture strength. In this case, the maximum stress reaches less than 20% of the fracture stress and can be interpreted as a safe limit for fatigue failure. The next FEA was performed to calculate natural frequencies and mode shapes. The first five mode shapes and corresponding natural frequencies are shown in Fig. 3.64.

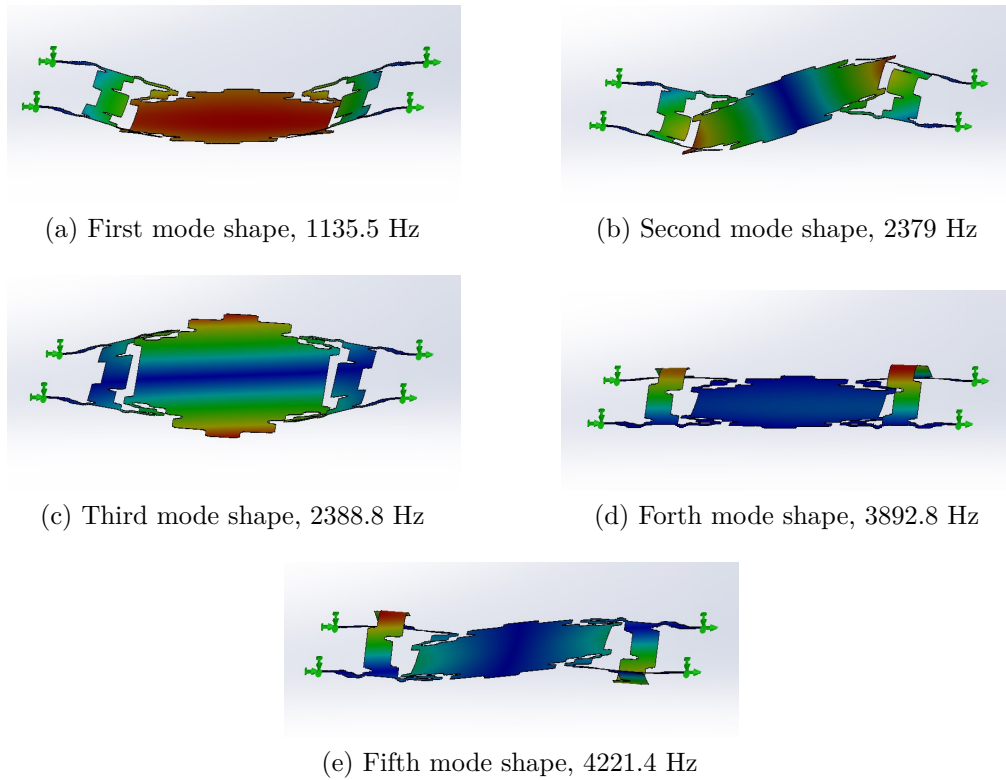


Figure 3.64 – Mode shapes and natural frequencies from FEA in design (D1).

The mode shapes for design (D1) in Fig. 3.64 show that the first mode shape (principal mode) is in the direction of desired motion in the accelerometer. This mode shape stays in this direction because of keeping the ratio of second to first natural frequency higher than two during the optimization process. It prevents the mode switch between these two vibration modes. In addition, the difference between modes reduces the sensitivity of movements in the lateral directions (directions not aligned with the principal mode direction). It reduces the cross-axis sensitivity which is beneficial for higher resolution of tilt measurement. For FEA of design D2, the domain meshed by solid standard mesh with 16 Jacobian points and 18.27 microns element size. A total of 23209 elements and 50460 nodes were used to mesh this structure with a tolerance of 0.91 microns as shown in Fig. 3.65.

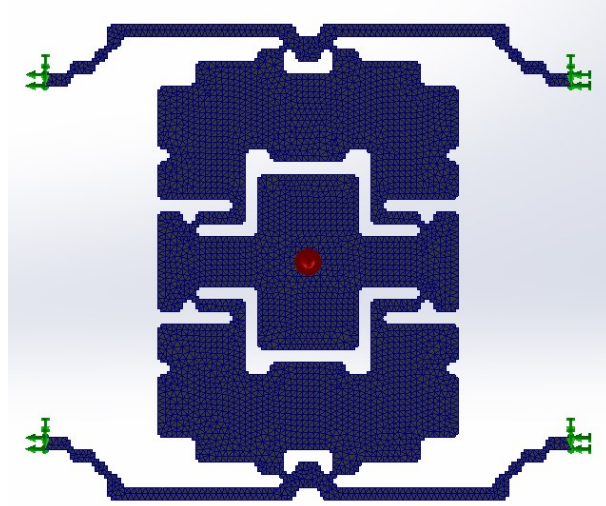


Figure 3.65 – Mesh for FEA of design (D2).

Similar to the previous case, an acceleration of $1g$ is applied as a gravity load in the out-of-plane direction while the boundaries are fixed. It will result in a displacement as shown in Fig. 3.66 with a maximum displacement of 0.55 microns at the center of the design.

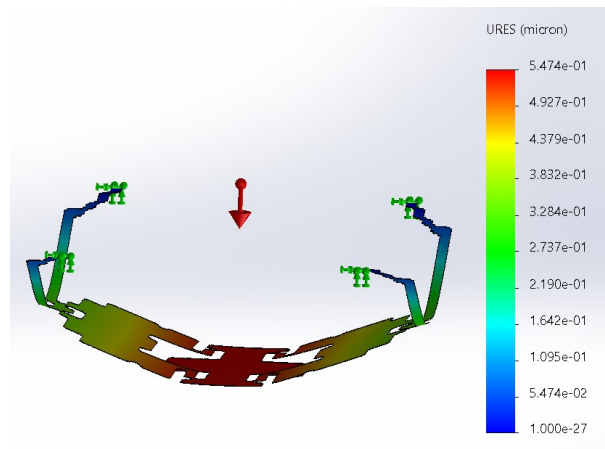


Figure 3.66 – Total displacement in design (D2) from FE simulation with a scale of 1000.

From the displacement of design D2 in Fig. 3.66, it can be seen that even though the maximum displacement in this design is more than in design D1, most of the movable electrode does not have a uniform motion. Consequently, this design cannot represent higher sensitivity even if its displacement is bigger than the previous case. So, the sensitivity is not necessarily maximized while the first natural frequency is minimized. In addition, this design has more delicate suspensions with more local stresses. The stress distribution in this design is simulated by FE and it is shown in Fig. 3.67.

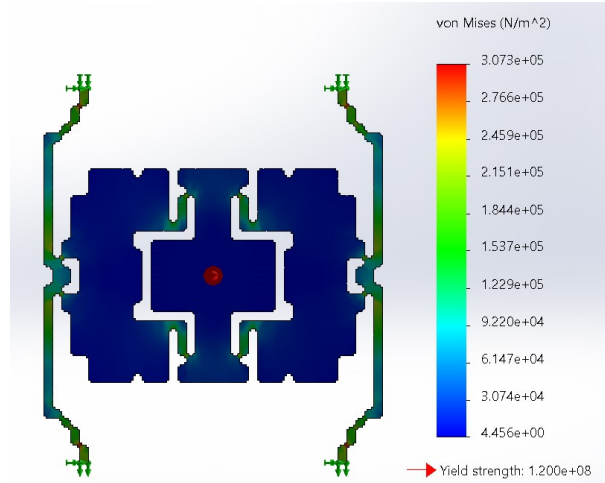


Figure 3.67 – Von Mises stress in design (D2) by applying $1g$ of inertial acceleration.

Maximum local stress of 307.3 KPa is reported in the simulation results for this design. This maximum stress is higher than design D1 but still far from the yield stress of silicon. Higher stress and displacement reduce fatigue life. Similar to the previous design, keeping the ratio of second to first natural frequencies higher than two prevents the mode switch and the principal mode stays in line with the sensing direction of the sensor. Fig. 3.68 shows mode shapes and natural frequencies of the design D2 simulated by FE.

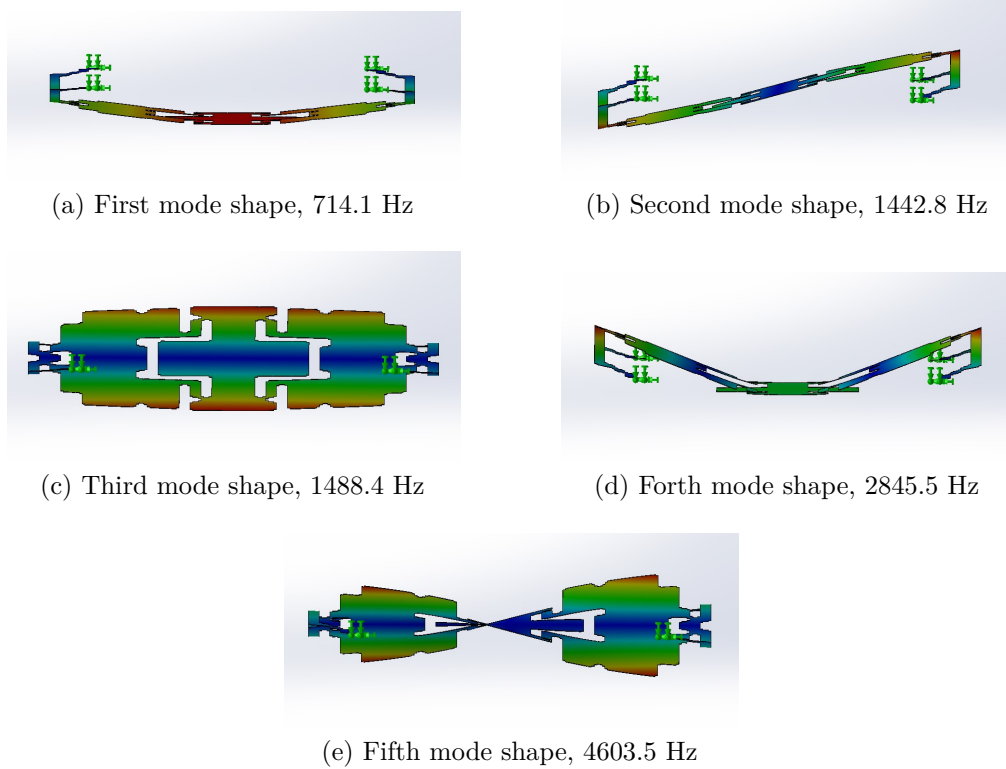


Figure 3.68 – Mode shapes and natural frequencies from FEA in design (D2).

In the third design for maximizing the ratio of second to the first natural frequency, design D3, the domain is meshed by a solid standard mesh with 16 Jacobian points and

20.84 micron element size. A total of 32193 elements and 67504 nodes are used to mesh this structure with a tolerance of 1.04 microns as shown in Fig. 3.69.

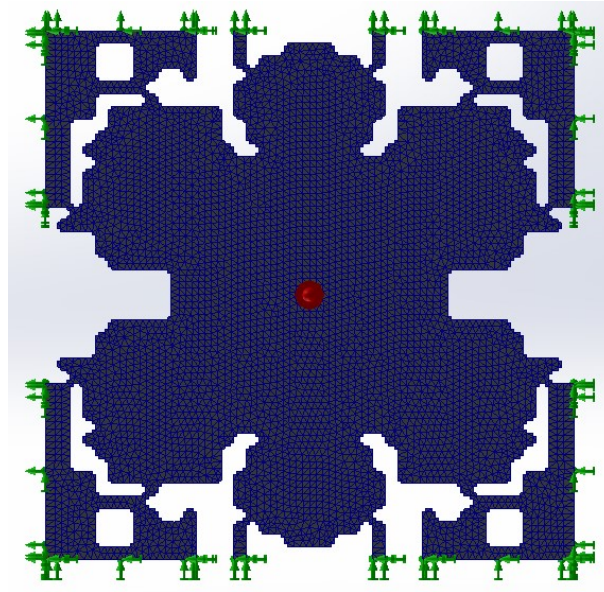


Figure 3.69 – Mesh for FEA of design (D3).

Applying a gravitational acceleration of $1g$ to this structure with fixed boundaries moves each element as shown in Fig. 3.70 with a maximum displacement of 0.02 micron at the center of the design.

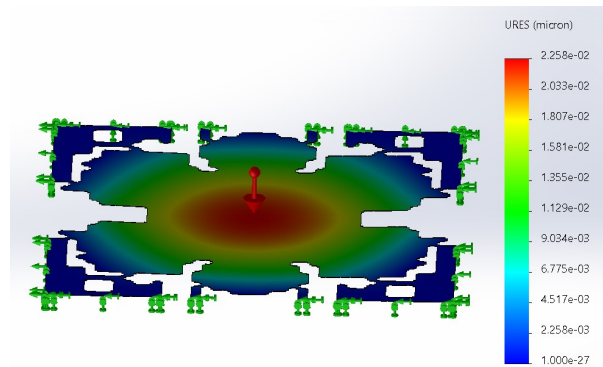


Figure 3.70 – Total displacement in design (D3) from FE simulation with a scale of 1000.

The displacement in design 3 is very limited because of the objective function in the optimization problem. This small and not uniform displacement results in a very low sensitivity in the principal direction. But the cross-axis sensitivity would be very smaller according to the high ratio of second to the first natural frequencies. The maximum stress in this design is 68.2 KPa which is very far from the yield stress. The stress distribution is shown in Fig. 3.71.

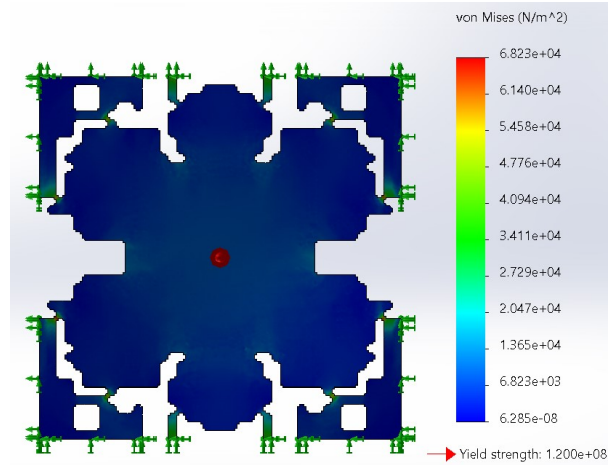


Figure 3.71 – Von Mises stress in design (D3) by applying $1g$ of inertial acceleration.

The first five mode shapes and natural frequencies for design D3 are shown in Fig. 3.72.

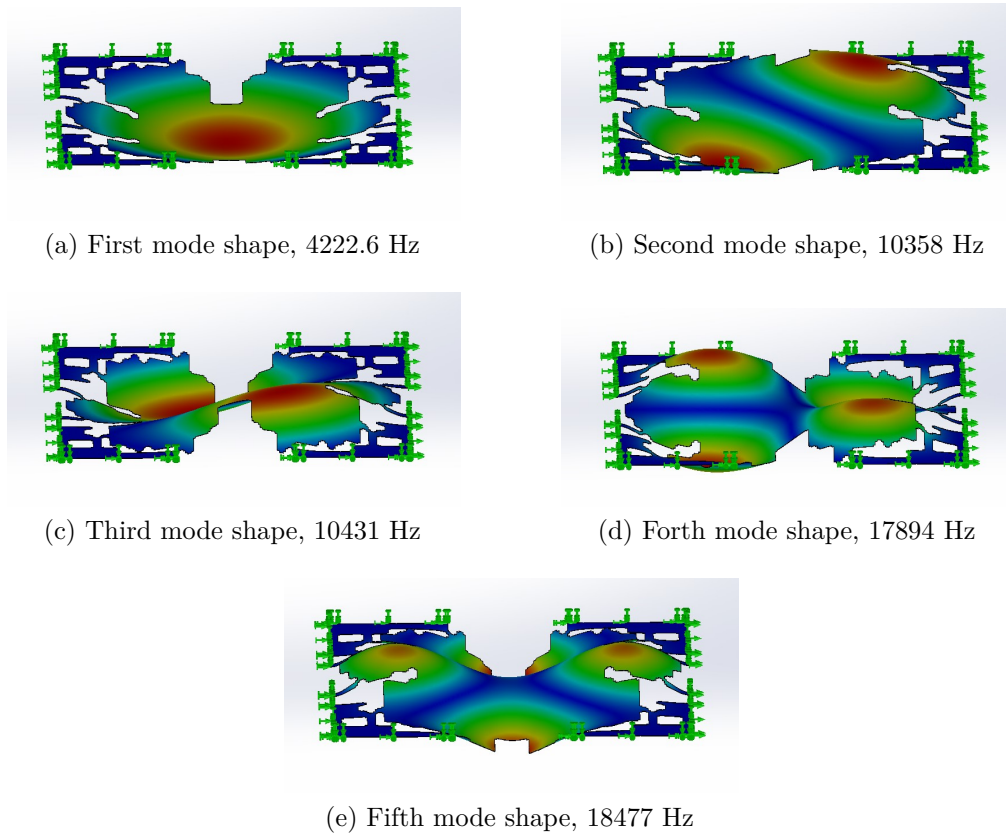


Figure 3.72 – Mode shapes and natural frequencies from FEA in design (D3).

Natural frequencies and mode shapes in Fig. 3.72 for design D3 show more differences rather than other designs. But since the natural frequencies are higher than in previous cases, cross-axis sensitivity is not necessarily smaller.

The results showed that optimized designs can improve a required specification by using the proposed TO method. Since a combination of several parameters changes in a

new design, they give a better view if compared by all of them. So, several parameters are calculated for the proposed designs and compared to the literature.

The cut-off frequency is the frequency bandwidth in which the magnitude of deflection drops $3dB$ and can be calculated by Eq. (3.13). This frequency is referred as bandwidth and is used to calculate bandwidth in each design.

$$\omega_c = \gamma F_n = F_n \sqrt{1 - 2\zeta^2 + \sqrt{(1 - 2\zeta^2)^2 + 1}} \quad (3.13)$$

where ζ is damping ratio and can be calculated by Eq. 3.14.

$$\zeta = \frac{c}{c_c} = \frac{c}{2m\sqrt{K_m/m}} = \frac{c}{2\sqrt{mK_m}} \quad (3.14)$$

where c is the damping coefficient and can be estimated using Eq. 3.15 for squeeze film damping [121].

$$c = \frac{12\mu_a A^2}{N\pi d^3 G(A_h)} \quad (3.15)$$

where μ_a is viscosity of air, A is the parallel surface area of electrodes, N is the number of perforations in the electrode, d is initial distance of electrodes as shown in Fig. 2.1, and $G(A_h)$ is a parameter calculated by Eq. 3.16 from fraction of open area (A_h).

$$G(A_h) = \frac{A_h}{2} + \frac{A_h}{8} - \frac{Ln(A_h)}{4} - \frac{3}{8} \quad (3.16)$$

To compare the results with available designs, some performance parameters and specifications are shown in Table 11.

Table 11 – Comparison of specifications and performance in proposed designs and similar designs in the literature.

Parameter	D1	D2	D3	Farahani et al. [60]	Hsu et al. [122]	Tsai et al.[123]
Size (μm^2)	1600 ²	1600 ²	1600 ²	1272 × 632	5000 ²	400 ²
Fabrication	PM	PM	PM	PM	SOI	0.18 μm CMOS
$S_{x,x}(fF.g^{-1})$	48.3	83.4	28.9	2	42.5	2.68
$S_{x,z}/S_{x,x}(\%)$	5.6×10^{-4}	1.2×10^{-3}	5.9×10^{-4}	-	1.94	5.2
$S_{x,y}/S_{x,x}(\%)$	4.8×10^{-2}	1.7×10^{-2}	2.1×10^{-1}	-	1.32	5.3
Pull-in vol. (V)	0.414	0.3441	1.5644	2.519	-	-
$F_1(Hz)$	1135.5	714.1	4222	6750	3050	6100
$F_2(Hz)$	2379	1442.8	10358	7063	-	7100
Bandwidth (Hz)	448	343	1854	340	100	-

The results mentioned in Table 11 are from the TO in this study referred by D1, D2, and D3. Three similar cases are mentioned in the literature with similar performance. The first reference is from the design presented by Farahani et al. [60]. This design uses the PolyMUMPs (shown by PM in this table) with the same parameters for a parallel plate accelerometer. It can be seen that the proposed designs in this work improved out-of-plane sensitivity($S_{x,x}$) by using the TO method. The bandwidth is also similar to the reference value. The other design in the literature presented by Tsai [123] also uses a similar surface

micromachining process for the fabrication of an accelerometer. The sensitivity in the proposed designs in this study is considerably higher than this reference due to the higher thickness of proof mass and optimized topology. The cross-axis sensitivity is also reduced in the proposed design by the optimization process. The cross-axis sensitivity is already low in accelerometers made by surface micromachining because the dimensions of elements are much smaller in the out-of-plane directions. The other case presented in the literature is from Hsu et al. [122], where they used bulk micromachining to fabricate a MEMS accelerometer. The sensitivity from the proposed method by TO is compatible with this bulk micro-machined accelerometer. In designs where the objective is maximizing sensitivity (D1) and minimizing the first natural frequency (D2), the sensitivity is higher than the value in the reference. It should be noted that according to higher surface area and lower stiffness in the measurement direction, the pull-in voltages are smaller in the proposed designs. So the measurement voltages should be smaller than the similar designs, but it still provides more sensitivity than the designs in the literature. The main advantage of the two first designs is higher sensitivity in addition to low cross-axis sensitivity. They have an acceptable bandwidth and pull-in voltage for the required application. The design optimized for minimizing cross-axis sensitivity (D3) have only smaller cross-axis sensitivity in one direction, while the sensitivity is smaller than in other cases. So this design and objective function is not reasonable to be used in this design. This is because the maximum ratio of second to first natural frequencies accrues about $F1 = 4200Hz$ and it is not in the range of desired sensitivity in this case. Maybe in another case with different design parameters, this objective function is beneficial to find an efficient design.

3.7 Design for Microfabrication

The design for the PolyMUMPs process needs extra steps to pass the fabrication limits that are not covered in the post-processing. These limits are mainly for adding electrodes and anchors for suspended structures. The fabrication process with all details is simulated with SEMulator3D software from COVENTOR. PolyMUMPs process starts with an n-type (100) wafer heavily doped with phosphorus in a diffusion furnace. Then a low-stress silicon nitride with $600nm$ thickness is deposited on the wafer. This layer is covered by the first structural layer of silicon with $500nm$ thickness and then covered by a photoresist. The shape of fixed electrodes is patterned by exposing this photoresist to UV light. All of the designs and two designs from the references are put in a single sample of $4.75 \times 4.75mm^2$ of the wafer. The photoresist is developed to remove the exposed areas and the photoresist mask is used later in RIE to remove unwanted polysilicon. The rest of the photoresist is removed after RIE and leaves behind fixed electrodes for each accelerometer. Extra parts are added to these electrodes for external connections to electronics. In the next step, $2\mu m$ of PSG is deposited by low-pressure chemical vapor deposition (LPCVD) as the

first sacrificial layer (a part of the air gap for accelerometers). Complete lithography with photoresist could make $750nm$ dimples if it is any of it in this design. So this step will be done with no mask. Another lithography for making anchors of the second polysilicon layer is also made with no mask since this layer is not considered in the design. The rest of the process for deposition of the second polysilicon layer and its patterning is skipped from PolyMUMPs since this layer is not available in this design. Then anchors for connection of the third polysilicon layer are opened on the first PSG layer by lithography. Then a $0.75\mu m$ of PSG layer is deposited as the second sacrificial layer. Both sacrificial layers together are making the air gap between the first and third polysilicon layers. The Second Oxide layer, $0.75\mu m$ of PSG, is deposited on the wafer. This layer is patterned twice to allow it to connect to both Poly 1 and substrate layers. Then the anchors to connect the third polysilicon layer to the nitride or first polysilicon layer are patterned by lithography. Then the third polysilicon layer with $1.5\mu m$ of thickness is deposited by LPCVD on the top of the sample. This layer is patterned with a mask from the structures designed and from the literature. Then some holes are etched on it for shorter release etch paths to remove sacrificial layers. Then the photoresist and PSG mask are removed and $500nm$ of gold is deposited by evaporation in a vacuum chamber. Then unwanted metal on structural layers is removed by lift-off metal patterning. This metal layer is for connecting electrodes and external connections. The manufacturing process is complete and can be protected by a layer of photoresist for dicing and transfer. Then the suspended structure would be released by immersion in a 49%HF solution. Fig. 3.73 shows the surface micromachining process in PolyMUMPs for the fabrication of this design.

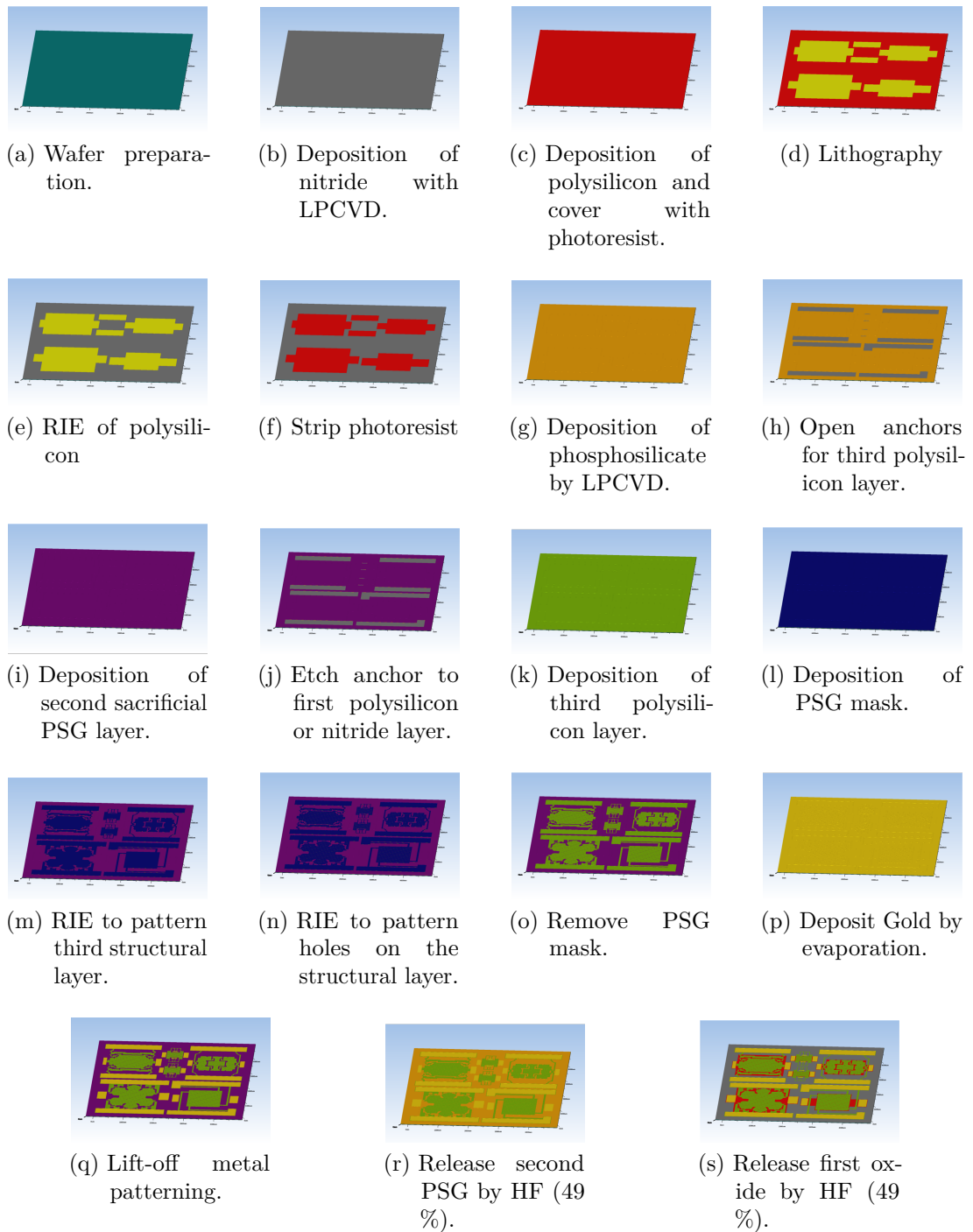


Figure 3.73 – Simulated fabrication process with PolyMUMPs.

There are some design rules to keep distance and provide enough space for each layer to be deposited. These rules should be satisfied to make sure the design is manufacturable. In this case, the whole design is arranged for a PolyMUMPs run and checked with a design kit from Canadian Microelectronics Corporation (CMC).

4 Conclusion and future works

This research introduces the Topology Optimization (TO) method to design surface micro-machined MEMS sensors for landslide monitoring applications. Common types of landslide mechanisms reviewed and showed accurate measurement of displacement is an important parameter to predict landslides. Similarly, in structural health monitoring, displacements in different locations can be used to predict the collapse of infrastructures like dams and bridges. According to these applications, maximization of sensitivity and reduction of cross-axis sensitivity are the objective of the design. Several constraints from manufacturing and performance limits are applied to this TO problem. This non-convex and multi-constraint TO problem are not solvable by available TO methods. So, a meta-heuristic TO based on Simulated Annealing (SA) and crystallization factors is developed here. This method works directly with the objective function of TO, but the new solutions are generated by a history of previous evaluations. Thus, it improves convergence to the optimum solution in a meta-heuristic TO. This method has the ability to consider several constraints as hard limits and perform topology optimization without invading constraints. It provides a valid design from a manufacturing perspective and improves it in each step of optimization. The proposed TO method is validated by some benchmark TO problems in the literature. It shows that the proposed method can effectively solve various types of TO problems without a need to calculate gradients of objective functions or constraints. Even though this method only works with the objective function of the optimization problem, it still presents some information about the optimization problem that can be analyzed for selecting TO parameters and investigating convergence to the optimum solution. Since there is no sensitivity information in this method, the common sensitivity filters cannot be applied to this TO method. To avoid checkerboards and improve manufacturability, some filtering and post-processing methods are used in this study. Filters and post-processing techniques developed here based on the density filters and morphological operators and they elaborate the optimized topologies to be manufactured by the surface micromachining process. In addition, another TO method was developed with binary elements to consider connectivity in two ways; penalizing the connectivity criteria as a weighting function of the objective function, and only evaluating of new solutions with all connected elements. Both methods showed that they can improve the connectivity of the optimum design and reduce the checkerboards. Developed TO methods are applied to design an out-of-plane capacitive accelerometer with different objective functions and constraints. Then the TO algorithm is used successfully to design a surface micro-machined MEMS accelerometer with the PolyMUMPs process. Design topologies are analyzed for convergence to an optimum point and then they are compared based on the objective functions and constraints. It shows that maximizing sensitivity or minimizing the first natural frequency with a constraint

on connectivity ratios second to the first natural frequency, and maximum allowed displacement is a proper combination to get to an optimum solution. The results are compared with a similar design in the literature and show considerable improvements in sensitivity and a reduction in cross-axis sensitivity. In addition to the proposed method and the design strategy in this work, there are possibilities for using the proposed method to solve non-convex optimization problems and topology optimization with manufacturing constraints. Some suggestions are proposed in the following for future works:

- Development of the proposed method for non-gradient topology optimization with faster convergence.
- Use of the proposed method for different topology optimization problems with several hard constraints and manufacturing limits.
- Using directional vectors and radius in the application of crystallization factors for topology optimization in anisotropic material with high aspect ratio.
- Use the proposed topology optimization method for a flexible manufacturing design and improve the design by having more design variables.
- Add electronics and test the performance to check the compatibility of electronics and design proper electronics.
- Combine different designs to increase the accuracy of linear and angular measurements simultaneously.

Bibliography

- 1 CHAE, B.-G. et al. Landslide prediction, monitoring and early warning: a concise review of state-of-the-art. *Geosciences Journal*, Springer, v. 21, n. 6, p. 1033–1070, 2017. Cited 2 times in pages 2 and 7.
- 2 LACERDA, W. A.; NETTO, A. C.; SATO, A. M. Technical report on landslide related disasters in brazil. In: *Slope Safety preparedness for impact of Climate Change*. [S.l.]: CRC Press, 2017. p. 45–70. Cited in page 2.
- 3 HIGHLAND, L.; BOBROWSKY, P. T. et al. *The landslide handbook: a guide to understanding landslides*. [S.l.]: US Geological Survey Reston, 2008. Cited 3 times in pages 2, 3, and 4.
- 4 CRUDEN, D.; VARNES, D. Landslides investigation and mitigation. landslide types and processes. *Special report*, v. 247, 1996. Cited 2 times in pages 2 and 4.
- 5 SCHUSTER, R. L.; HIGHLAND, L. *Socioeconomic and environmental impacts of landslides in the western hemisphere*. [S.l.]: US Department of the Interior, US Geological Survey Denver (CO), 2001. Cited in page 4.
- 6 VARNES, D. J. Slope movement types and processes. *Special report*, v. 176, p. 11–33, 1978. Cited in page 4.
- 7 CLARK, A.; MOORE, R.; PALMER, J. Slope monitoring and early warning systems: application to coastal landslide on the south and east coast of england, uk. In: CITESEER. *Proceedings of the seventh international symposium on landslides*. [S.l.], 1996. p. 1531–1538. Cited in page 5.
- 8 ANGELI, M.; PASUTO, A.; SILVANO, S. Landslide hazard in high mountain areas: some case histories (italy). *JOURNAL-GEOLOGICAL SOCIETY OF CHINA-TAIWAN-, GEOLOGICAL SOCIETY OF CHINA AND ACADEMIA SINICA*, v. 39, p. 401–422, 1996. Cited in page 5.
- 9 ANGELI, M.-G.; PASUTO, A.; SILVANO, S. A critical review of landslide monitoring experiences. *Engineering Geology*, Elsevier, v. 55, n. 3, p. 133–147, 2000. Cited in page 5.
- 10 COROMINAS, J. et al. Measurement of landslide displacements using a wire extensometer. *Engineering Geology*, Elsevier, v. 55, n. 3, p. 149–166, 2000. Cited in page 5.
- 11 ZAN, L. et al. Landslides early warning monitoring system. In: IEEE. *IEEE International Geoscience and Remote Sensing Symposium*. [S.l.], 2002. v. 1, p. 188–190. Cited in page 6.
- 12 SAVVAIDIS, P. Existing landslide monitoring systems and techniques. *From stars to earth and culture*, School of Rural and Surveying Engineering, Aristotle University of ... , p. 242–258, 2003. Cited in page 6.
- 13 ZHOU, P. et al. A demonstrative gps-aided automatic landslide monitoring system in sichuan province. *Positioning*, Scientific Research Publishing, v. 1, n. 09, 2005. Cited in page 6.

- 14 PETLEY, D. et al. The use of surface monitoring data for the interpretation of landslide movement patterns. *Geomorphology*, Elsevier, v. 66, n. 1-4, p. 133–147, 2005. Cited in page 6.
- 15 GARICH, E. A. *Wireless, automated monitoring for potential landslide hazards*. Tese (Doutorado) — Texas A&M University, 2007. Cited in page 6.
- 16 ARNHARDT, C. et al. Sensor based landslide early warning system-slews. development of a geoservice infrastructure as basis for early warning systems for landslides by integration of real-time sensors. *Geotechnologien science report*, v. 10, p. 75–88, 2007. Cited in page 6.
- 17 YIN, Y. et al. Real-time monitoring and early warning of landslides at relocated wushan town, the three gorges reservoir, china. *Landslides*, Springer, v. 7, n. 3, p. 339–349, 2010. Cited in page 6.
- 18 GEORGIEVA, K. et al. An autonomous landslide monitoring system based on wireless sensor networks. In: CITESEER. *Proceedings of the 2012 ASCE International Conference on Computing in Civil Engineering. Clearwater Beach, FL, USA*. [S.l.], 2012. p. 145–8. Cited in page 6.
- 19 FUKUZONO, T. Experimental study of slope failure caused by heavy rainfall. *IAHS-AISH publication*, n. 165, p. 133–134, 1987. Cited in page 6.
- 20 TRAVELLETTI, J. et al. Correlation of multi-temporal ground-based optical images for landslide monitoring: Application, potential and limitations. *ISPRS Journal of Photogrammetry and Remote Sensing*, Elsevier, v. 70, p. 39–55, 2012. Cited in page 6.
- 21 PEPPA, M. et al. Accuracy assessment of a uav-based landslide monitoring system. *ISPRS-International Archives of the Photogrammetry, Remote Sensing and Spatial Information Sciences*, ISPRS, v. 41, p. 895–902, 2016. Cited in page 6.
- 22 SRINIVAS, Y.; RAO, K. R. Landslide warning system using zigbeeand gps. *IOSR Journal of Engineering (IOSRJEN)*, v. 4, n. 07, p. 01–06, 2014. Cited in page 7.
- 23 KIRSCHBAUM, D.; STANLEY, T. Satellite-based assessment of rainfall-triggered landslide hazard for situational awareness. *Earth's Future*, Wiley Online Library, v. 6, n. 3, p. 505–523, 2018. Cited in page 7.
- 24 LAGOMARSINO, D. et al. Updating and tuning a regional-scale landslide early warning system. *Landslides*, Springer, v. 10, n. 1, p. 91–97, 2013. Cited in page 7.
- 25 KRKAČ, M. et al. Method for prediction of landslide movements based on random forests. *Landslides*, Springer, v. 14, n. 3, p. 947–960, 2017. Cited in page 7.
- 26 OTERO, M. D. et al. Use of low-cost accelerometers for landslides monitoring: results from a flume experiment. *Soils and Rocks*, SciELO Brasil, v. 45, 2022. Cited in page 7.
- 27 LALEHPOUR, A.; BERRY, C.; BARARI, A. Adaptive data reduction with neighbourhood search approach in coordinate measurement of planar surfaces. *Journal of Manufacturing Systems*, Elsevier, v. 45, p. 28–47, 2017. Cited in page 7.

- 28 BERRY, C.; BARARI, A. Cyber-physical system utilizing work-piece memory in digital manufacturing. *IFAC-PapersOnLine*, Elsevier, v. 52, n. 10, p. 201–206, 2019. Cited in page 7.
- 29 SELVARAJAN, A. Mems and photonics technologies for structural health monitoring. In: SPIE. *Smart Materials, Structures, and Systems*. [S.l.], 2003. v. 5062, p. 10–17. Cited in page 8.
- 30 ROTTA, L. H. S. et al. The 2019 brumadinho tailings dam collapse: Possible cause and impacts of the worst human and environmental disaster in brazil. *International Journal of Applied Earth Observation and Geoinformation*, Elsevier, v. 90, p. 102119, 2020. Cited in page 8.
- 31 BORGES, R. C. et al. Radiological characterization of the area impacted by the mariana dam disaster, in mariana city-mg-brazil. *Environmental Earth Sciences*, Springer, v. 80, n. 12, p. 1–15, 2021. Cited in page 8.
- 32 SOUSA, J.; BASTOS, L. Multi-temporal sar interferometry reveals acceleration of bridge sinking before collapse. *Natural Hazards and Earth System Sciences*, Copernicus GmbH, v. 13, n. 3, p. 659–667, 2013. Cited in page 8.
- 33 GLASER, S. D. et al. Sensor technology innovation for the advancement of structural health monitoring: a strategic program of us-china research for the next decade. *Smart Structures and Systems*, Techno-Press, v. 3, n. 2, p. 221–244, 2007. Cited in page 8.
- 34 JEON, J. et al. Development of dam safety management system. *Advances in Engineering Software*, Elsevier, v. 40, n. 8, p. 554–563, 2009. Cited in page 8.
- 35 SHARMA, R.; KUMAR, A. Case histories of earthen dam failures. Missouri University of Science and Technology, 2013. Cited in page 8.
- 36 LYNCH, J. P. et al. Design of piezoresistive mems-based accelerometer for integration with wireless sensing unit for structural monitoring. *Journal of Aerospace Engineering*, Citeseer, v. 16, n. 3, p. 108–114, 2003. Cited in page 8.
- 37 SAAFI, M.; ROMINE, P. Embedded mems for health monitoring and management of civil infrastructure. In: SPIE. *Smart Structures and Materials 2004: Sensors and Smart Structures Technologies for Civil, Mechanical, and Aerospace Systems*. [S.l.], 2004. v. 5391, p. 331–343. Cited in page 8.
- 38 ABDOUN, T. et al. Asset management and safety assessment of levees and earthen dams through comprehensive real-time field monitoring. *Geotechnical and Geological Engineering*, Springer, v. 31, n. 3, p. 833–843, 2013. Cited in page 8.
- 39 DOGHRI, W.; SADDOUD, A.; FOURATI, L. C. Cyber-physical systems for structural health monitoring: sensing technologies and intelligent computing. *The Journal of Supercomputing*, Springer, v. 78, n. 1, p. 766–809, 2022. Cited in page 9.
- 40 NUZZO, F. D. et al. Structural health monitoring system with narrowband iot and mems sensors. *IEEE Sensors Journal*, IEEE, v. 21, n. 14, p. 16371–16380, 2021. Cited in page 9.

- 41 VILLACORTA, J. J. et al. Design and validation of a scalable, reconfigurable and low-cost structural health monitoring system. *Sensors*, MDPI, v. 21, n. 2, p. 648, 2021. Cited in page 9.
- 42 PARISI, E. et al. Time and frequency domain assessment of low-power mems accelerometers for structural health monitoring. In: IEEE. *2022 IEEE International Workshop on Metrology for Industry 4.0 & IoT (MetroInd4. 0&IoT)*. [S.l.], 2022. p. 234–239. Cited in page 9.
- 43 KOMARIZADEHASL, S. et al. A novel wireless low-cost inclinometer made from combining the measurements of multiple mems gyroscopes and accelerometers. *Sensors*, Multidisciplinary Digital Publishing Institute, v. 22, n. 15, p. 5605, 2022. Cited in page 9.
- 44 PLEUGER, L.; HAUPT, M.; PAFFENHOLZ, J.-A. Data fusion of mems accelerometer and hydrostatic leveling for structural health monitoring—the test rig investigations. Cited in page 9.
- 45 ARNHARDT, C.; FERNANDEZ-STEEGER, T.; AZZAM, R. Sensor fusion in an ad-hoc multi-hop sensor network for real-time monitoring of landslides endangering human infrastructures. *Science Report*, v. 9, p. 38, 2009. Cited 2 times in pages 9 and 10.
- 46 BENNETT, V. et al. Design and characterization of a compact array of mems accelerometers for geotechnical instrumentation. *Smart structures and systems*, v. 5, n. 6, p. 663–679, 2009. Cited in page 9.
- 47 TRAN, D. T. et al. Development of a rainfall-triggered landslide system using wireless accelerometer network. *International Journal of Advancements in Computing Technology*, Advanced Institutes of Convergence Information Technology, v. 7, n. 5, p. 14, 2015. Cited 2 times in pages 10 and 14.
- 48 LI, C.; AZZAM, R.; FERNÁNDEZ-STEEGER, T. M. Kalman filters in geotechnical monitoring of ground subsidence using data from mems sensors. *Sensors*, MDPI, v. 16, n. 7, p. 1109, 2016. Cited in page 10.
- 49 ALIPPI, C.; GALPERTI, C.; ZANCHETTA, M. Micro acoustic monitoring with mems accelerometers: Towards a wsn implementation. In: IEEE. *SENSORS, 2007 IEEE*. [S.l.], 2007. p. 966–969. Cited in page 10.
- 50 KOTTA, H. Z. et al. Wireless sensor network for landslide monitoring in nusa tenggara timur. *TELKOMNIKA (Telecommunication Computing Electronics and Control)*, v. 9, n. 1, p. 9–18, 2011. Cited in page 10.
- 51 HUANG, X. et al. Frequency characteristics and numerical computation of seismic records generated by a giant debris flow in zhouqu, western china. *Pure and Applied Geophysics*, Springer, v. 177, n. 1, p. 347–358, 2020. Cited in page 10.
- 52 TEVES, A. d. C. et al. Structural design of high-performance capacitive accelerometers using parametric optimization with uncertainties. *Engineering Optimization*, Taylor & Francis, v. 49, n. 3, p. 365–380, 2017. Cited 2 times in pages 14 and 20.
- 53 WANG, L.-P. et al. Design, fabrication, and measurement of high-sensitivity piezo-electric microelectromechanical systems accelerometers. *Journal of microelectromechanical systems*, IEEE, v. 12, n. 4, p. 433–439, 2003. Cited in page 15.

- 54 YAZDI, N.; AYAZI, F.; NAJAFI, K. Micromachined inertial sensors. *Proc IEEE*, IEEE, v. 86, n. 8, p. 1640–1659, 1998. Cited 3 times in pages 15, 18, and 40.
- 55 KRAFT, M. Micromachined inertial sensors: The state-of-the-art and a look into the future. *Meas Control*, SAGE Publications Sage UK: London, England, v. 33, n. 6, p. 164–168, 2000. Cited in page 15.
- 56 MOHAMMED, Z.; ELFADEL, I. A. M.; RASRAS, M. Monolithic multi degree of freedom (mdof) capacitive mems accelerometers. *Micromachines*, Multidisciplinary Digital Publishing Institute, v. 9, n. 11, p. 602, 2018. Cited in page 15.
- 57 KANNAN, A. *Design and modeling of a MEMS-based accelerometer with pull in analysis*. Tese (Doutorado) — University of British Columbia, 2008. Cited in page 15.
- 58 LIU, H. et al. Design, fabrication, and performance characterization of ltcc-based capacitive accelerometers. *Micromachines*, Multidisciplinary Digital Publishing Institute, v. 9, n. 3, p. 120, 2018. Cited in page 16.
- 59 ROCHA, L. A. et al. Auto-calibration of capacitive mems accelerometers based on pull-in voltage. *Microsystem technologies*, Springer, v. 17, n. 3, p. 429–436, 2011. Cited in page 16.
- 60 FARAHANI, H.; MILLS, J. K.; CLEGHORN, W. L. Design, fabrication and analysis of micromachined high sensitivity and 0% cross-axis sensitivity capacitive accelerometers. *Microsystem technologies*, Springer, v. 15, n. 12, p. 1815–1826, 2009. Cited 4 times in pages 17, 19, 20, and 105.
- 61 IBARRA-VILLEGAS, F. et al. Design of capacitive mems transverse-comb accelerometers with test hardware. *Superficies y vacío*, Sociedad Mexicana de Ciencia y Tecnología de Superficies y Materiales AC, v. 26, n. 1, p. 4–12, 2013. Cited in page 17.
- 62 CHI, W. W. Analysis of the suspension beam in accelerometer for stiffness constant and resonant frequency by using analytical and numerical investigation. *Universiti Sains Malaysia*, 2007. Cited in page 19.
- 63 TANG, W. C.-K. *Electrostatic comb drive for resonant sensor and actuator applications*. [S.l.]: University of California, Berkeley, 1990. Cited in page 20.
- 64 LU, Q. et al. Design, optimization, and realization of a high-performance moems accelerometer from a double-device-layer soi wafer. *Journal of Microelectromechanical Systems*, IEEE, v. 26, n. 4, p. 859–869, 2017. Cited in page 20.
- 65 BAIS, B.; MAJLIS, B. Y. Mechanical sensitivity enhancement of an area-changed capacitive accelerometer by optimization of the device geometry. *Analog Integrated Circuits and Signal Processing*, Springer, v. 44, n. 2, p. 175–183, 2005. Cited in page 20.
- 66 MOHAMMED, Z. et al. An optimization technique for performance improvement of gap-changeable mems accelerometers. *Mechatronics*, Elsevier, v. 54, p. 203–216, 2018. Cited in page 20.
- 67 PAK, M.; FERNANDEZ, F. V.; DUNDAR, G. Optimization of a mems accelerometer using a multiobjective evolutionary algorithm. In: IEEE. *2017 14th International Conference on Synthesis, Modeling, Analysis and Simulation Methods and Applications to Circuit Design (SMACD)*. [S.l.], 2017. p. 1–4. Cited in page 20.

- 68 GOMATHI, K.; BALAJI, A.; MRUNALINI, T. Design and optimization of differential capacitive micro accelerometer for vibration measurement. *Journal of the Mechanical Behavior of Materials*, De Gruyter, v. 30, n. 1, p. 19–27, 2021. Cited in page 20.
- 69 HU, Q. et al. Low cross-axis sensitivity micro-gravity microelectromechanical system sandwich capacitance accelerometer. *Micro & Nano Letters*, IET, v. 6, n. 7, p. 510–514, 2011. Cited in page 20.
- 70 ZOU, X.; THIRUVENKATANATHAN, P.; SESHIA, A. A. A seismic-grade resonant mems accelerometer. *Journal of Microelectromechanical Systems*, IEEE, v. 23, n. 4, p. 768–770, 2014. Cited in page 20.
- 71 FUJIYOSHI, M. et al. Stress isolation suspension for silicon-on-insulator 3-axis accelerometer designed by topology optimization method. *IEEE Sensors Journal*, IEEE, v. 22, n. 5, p. 3965–3973, 2022. Cited in page 21.
- 72 PHILIPPINE, M. A. et al. Topology optimization of stressed capacitive rf mems switches. *Journal of microelectromechanical systems*, IEEE, v. 22, n. 1, p. 206–215, 2012. Cited in page 21.
- 73 BENDSOE, M. P.; SIGMUND, O. *Topology optimization: theory, methods, and applications*. [S.l.]: Springer Science & Business Media, 2003. Cited 5 times in pages 21, 38, 53, 66, and 74.
- 74 TEVES, A. d. C.; SILVA, E. C. N. Design of capacitive bulk-micromachined accelerometers using the topology optimization method. *Anais*, 2011. Cited in page 21.
- 75 WANG, C. et al. Design of freeform geometries in a mems accelerometer with a mechanical motion preamplifier based on a genetic algorithm. *Microsystems & Nanoengineering*, Nature Publishing Group, v. 6, n. 1, p. 1–15, 2020. Cited in page 22.
- 76 KOCHENDERFER, M. J.; WHEELER, T. A. *Algorithms for optimization*. [S.l.]: Mit Press, 2019. Cited in page 25.
- 77 BOYD, S.; BOYD, S. P.; VANDENBERGHE, L. *Convex optimization*. [S.l.]: Cambridge university press, 2004. Cited in page 25.
- 78 GOHARI, H.; BARARI, A.; KISHAWY, H. Using multistep methods in slicing 2 1/2 dimensional parametric surfaces for additive manufacturing applications. *IFAC-PapersOnLine*, Elsevier, v. 49, n. 31, p. 67–72, 2016. Cited in page 26.
- 79 BARARI, A. Automotive body inspection uncertainty associated with computational processes. *International journal of vehicle design*, Inderscience Publishers, v. 57, n. 2-3, p. 230–241, 2011. Cited in page 26.
- 80 ABBASI, A. A. et al. Application of hyperelastic models in mechanical properties prediction of mouse oocyte and embryo cells at large deformations. In: AMERICAN SOCIETY OF MECHANICAL ENGINEERS. *ASME International Mechanical Engineering Congress and Exposition*. [S.l.], 2016. v. 50534, p. V003T04A021. Cited in page 26.

- 81 DIBA, F.; BARARI, A.; ESMAILZADEH, E. Active aerodynamic system to improve the safety and handling of race cars in lane change and wet road maneuvers. In: AMERICAN SOCIETY OF MECHANICAL ENGINEERS. *International Design Engineering Technical Conferences and Computers and Information in Engineering Conference*. [S.l.], 2012. v. 45059, p. 417–423. Cited in page 26.
- 82 TEBBY, S.; BARARI, A.; ESMAILZADEH, E. Optimization of vehicle structure considering torsion stiffness using simple structural beam frame-approach. *Computer-Aided Design and Applications*, Taylor & Francis, v. 10, n. 3, p. 413–426, 2013. Cited in page 26.
- 83 BENDER, D.; BARARI, A. Using 3d density-gradient vectors in evolutionary topology optimization to find the build direction for additive manufacturing. *Journal of Manufacturing and Materials Processing*, MDPI, v. 7, n. 1, p. 46, 2023. Cited in page 27.
- 84 LUKE, S. *Essentials of metaheuristics*. [S.l.]: Lulu Raleigh, 2013. v. 2. Cited in page 27.
- 85 MARTINS, J. R.; NING, A. *Engineering design optimization*. [S.l.]: Cambridge University Press, 2021. Cited in page 30.
- 86 BARARI, A.; ELMARAGHY, H.; ORBAN, P. Nurbs representation of actual machined surfaces. *International Journal of Computer Integrated Manufacturing*, v. 22, n. 5, p. 395–410, 2009. Cited in page 30.
- 87 GOHARI, H.; BARARI, A.; KISHAWY, H. An efficient methodology for slicing nurbs surfaces using multi-step methods. *The International Journal of Advanced Manufacturing Technology*, Springer, v. 95, p. 3111–3125, 2018. Cited in page 30.
- 88 KIRKPATRICK, S.; JR, C. D. G.; VECCHI, M. P. Optimization by simulated annealing. *science*, American association for the advancement of science, v. 220, n. 4598, p. 671–680, 1983. Cited 2 times in pages 30 and 31.
- 89 NAJAFABADI, H. R. et al. Multi-objective topology optimization using simulated annealing method. In: SPRINGER. *ICGG 2020-Proceedings of the 19th International Conference on Geometry and Graphics*. [S.l.], 2021. p. 343–353. Cited in page 32.
- 90 GOTO, T. G. et al. Versatility of simulated annealing with crystallization heuristic: Its application to a great assortment of problems. In: *Engineering Problems-Uncertainties, Constraints and Optimization Techniques*. [S.l.]: IntechOpen, 2021. Cited 3 times in pages 34, 49, and 83.
- 91 VICENTE, J. D.; LANCHARES, J.; HERMIDA, R. Placement by thermodynamic simulated annealing. *Physics Letters A*, Elsevier, v. 317, n. 5-6, p. 415–423, 2003. Cited in page 34.
- 92 SIGMUND, O.; MAUTE, K. Topology optimization approaches. *Structural and Multidisciplinary Optimization*, Springer, v. 48, n. 6, p. 1031–1055, 2013. Cited in page 35.
- 93 SIGMUND, O. On the usefulness of non-gradient approaches in topology optimization. *Structural and Multidisciplinary Optimization*, Springer, v. 43, n. 5, p. 589–596, 2011. Cited in page 37.

- 94 BRUYNEEL, M.; DUYSINX, P. Note on topology optimization of continuum structures including self-weight. *Structural and Multidisciplinary Optimization*, Springer, v. 29, n. 4, p. 245–256, 2005. Cited in page 39.
- 95 LIU, J.; MA, Y. A survey of manufacturing oriented topology optimization methods. *Advances in Engineering Software*, Elsevier, v. 100, p. 161–175, 2016. Cited in page 39.
- 96 MAHBOUBKHAH, M.; BARARI, A. Design and development of a novel 4-dof parallel kinematic coordinate measuring machine (cmm). *International Journal of Computer Integrated Manufacturing*, Taylor & Francis, v. 32, n. 8, p. 750–760, 2019. Cited in page 39.
- 97 MHAPSEKAR, K.; MCCONAHA, M.; ANAND, S. Additive manufacturing constraints in topology optimization for improved manufacturability. *Journal of Manufacturing Science and Engineering*, American Society of Mechanical Engineers Digital Collection, v. 140, n. 5, 2018. Cited in page 39.
- 98 MAJD, Y. F.; TSUZUKI, M. S.; BARARI, A. On the accuracy of the infill pattern's density in additive manufacturing. *IFAC-PapersOnLine*, Elsevier, v. 55, n. 21, p. 43–48, 2022. Cited in page 39.
- 99 LAZAROV, B. S.; WANG, F.; SIGMUND, O. Length scale and manufacturability in density-based topology optimization. *Archive of Applied Mechanics*, Springer, v. 86, n. 1, p. 189–218, 2016. Cited in page 39.
- 100 GOHARI, H.; BERRY, C.; BARARI, A. A digital twin for integrated inspection system in digital manufacturing. *IFAC-PapersOnLine*, Elsevier, v. 52, n. 10, p. 182–187, 2019. Cited in page 39.
- 101 COWEN, A. et al. Polymumps design handbook. *Memscap Inc*, v. 13, 2011. Cited 2 times in pages 42 and 79.
- 102 GOHARI, H.; BARARI, A. A quick deviation zone fitting in coordinate metrology of nurbs surfaces using principle component analysis. *Measurement*, Elsevier, v. 92, p. 352–364, 2016. Cited in page 43.
- 103 BARARI, A.; MORDO, S. Effect of sampling strategy on uncertainty and precision of flatness inspection studied by dynamic minimum deviation zone evaluation. *International Journal of Metrology and Quality Engineering*, EDP Sciences, v. 4, n. 1, p. 3–8, 2013. Cited in page 43.
- 104 BARARI, A. et al. Integrated inspection and machining approach to machining error compensation: advantages and limitations. In: *Proceedings of FAIM*. [S.l.: s.n.], 2004. p. 563–572. Cited in page 43.
- 105 UMARAS, E.; BARARI, A.; TSUZUKI, M. d. S. G. Intelligent design tolerance allocation for optimum adaptability to manufacturing using a monte carlo approach. *IFAC-PapersOnLine*, Elsevier, v. 52, n. 10, p. 165–170, 2019. Cited in page 44.
- 106 BARARI, A.; ELMARAGHY, H.; KNOPF, G. Evaluation of geometric deviations in sculptured surfaces using probability density estimation. In: SPRINGER. *Models for Computer Aided Tolerancing in Design and Manufacturing: Selected Conference Papers from the 9th CIRP International Seminar on Computer-Aided Tolerancing, held*

- at Arizona State University, Tempe, Arizona, USA, 10-12 April, 2005. [S.l.], 2007. p. 135–146. Cited in page 45.
- 107 HEIJMANS, H. J. Connected morphological operators for binary images. *Computer Vision and Image Understanding*, Elsevier, v. 73, n. 1, p. 99–120, 1999. Cited in page 46.
- 108 GARCIA-LOPEZ, N. et al. A hybrid topology optimization methodology combining simulated annealing and simp. *Computers & structures*, Elsevier, v. 89, n. 15-16, p. 1512–1522, 2011. Cited in page 49.
- 109 NAJAFABADI, H. R. et al. Smart topology optimization using adaptive neighborhood simulated annealing. *Applied Sciences*, MDPI, v. 11, n. 11, p. 5257, 2021. Cited 2 times in pages 49 and 60.
- 110 MARTINS, T.; SATO, A.; TSUZUKI, M. *Adaptive neighborhood heuristics for simulated annealing over continuous variables*. [S.l.]: INTECH Open Access Publisher, 2012. Cited in page 50.
- 111 SIGMUND, O. A 99 line topology optimization code written in matlab. *Structural and multidisciplinary optimization*, Springer, v. 21, n. 2, p. 120–127, 2001. Cited 4 times in pages 54, 58, 61, and 62.
- 112 NAJAFABADI, H. R. et al. Post-processing of non gradient-based topology optimization with simulated annealing. *IFAC-PapersOnLine*, Elsevier, v. 54, n. 1, p. 755–760, 2021. Cited in page 62.
- 113 LIU, K.; TOVAR, A. An efficient 3d topology optimization code written in matlab. *Structural and Multidisciplinary Optimization*, Springer, v. 50, n. 6, p. 1175–1196, 2014. Cited 3 times in pages xii, 64, and 65.
- 114 NAJAFABADI, H. R. et al. Topology optimization and microfabrication constraints. In: IEEE. *2021 14th IEEE International Conference on Industry Applications (INDUSCON)*. [S.l.], 2021. p. 266–269. Cited in page 74.
- 115 PICELLI, R.; SIVAPURAM, R. Solving topology optimization with 0, 1 design variables and mathematical programming: the tobs method. In: *Proceedings of the 13th world congress of structural and multidisciplinary optimization (WCSMO-13), Beijing, China*. [S.l.: s.n.], 2019. Cited in page 74.
- 116 PICELLI, R.; SIVAPURAM, R.; XIE, Y. M. A 101-line matlab code for topology optimization using binary variables and integer programming. *Structural and Multidisciplinary Optimization*, Springer, v. 63, n. 2, p. 935–954, 2021. Cited in page 74.
- 117 GOTO, T. G. et al. A new non-gradient-based topology optimization algorithm with black–white density and manufacturability constraints. In: ELSEVIER. *Structures*. [S.l.], 2023. v. 47, p. 1900–1911. Cited in page 78.
- 118 REDDY, J. N. *Theory and analysis of elastic plates and shells*. [S.l.]: CRC press, 2006. Cited in page 80.
- 119 NAJAFABADI, H. R. et al. Topology optimization of capacitive mems accelerometers for seismic applications. In: SPRINGER. *ICGG 2022-Proceedings of the 20th International Conference on Geometry and Graphics*. [S.l.], 2022. p. 760–772. Cited in page 84.

-
- 120 ALSEM, D. H. *Mechanisms for fatigue and wear of polysilicon structural thinfilms*. [S.l.], 2006. Cited in page 99.
- 121 DAVIES, B. R. et al. *Micromachined accelerometer design, modeling and validation*. [S.l.], 1998. Cited in page 105.
- 122 HSU, C.-P.; YIP, M.-C.; FANG, W. Implementation of a gap-closing differential capacitive sensing z-axis accelerometer on an soi wafer. *Journal of micromechanics and microengineering*, IOP Publishing, v. 19, n. 7, p. 075006, 2009. Cited 2 times in pages 105 and 106.
- 123 TSAI, M.-H.; LIU, Y.-C.; FANG, W. A three-axis cmos-mems accelerometer structure with vertically integrated fully differential sensing electrodes. *Journal of microelectromechanical systems*, IEEE, v. 21, n. 6, p. 1329–1337, 2012. Cited in page 105.